Studying neutron dynamical diffraction theory and its applications in neutron optics

By

SOHRAB ABBAS

Bhabha Atomic Research Centre, Mumbai

A thesis submitted to the

Board of Studies in Physical Sciences

In partial fulfillment of requirements

For the Degree of

DOCTOR OF PHILOSOPHY

of

HOMI BHABHA NATIONAL INSTITUTE

January, 2012

Homi Bhabha National Institute

Recommendations of the Viva Voce Board

As members of the Viva Voce Board, we certify that we have read the dissertation prepared by Sohrab Abbas entitled "**Studying neutron dynamical diffraction theory and its applications in neutron optics**" and recommend that it may be accepted as fulfilling the dissertation requirement for the Degree of Doctor of Philosophy.

Chairman – Prof. S. V. G. Menon		**Date:** 25.4.12
Guide/Convener – Prof. Apoorva G. Wagh	A. G. Wagh.	**Date:** 25-4-12
External Examiner – Prof. P. S. Goyal		**Date:** 25-4-12
Member 1 – Prof. S. L. Chaplot	S. L. Chaplot	**Date:** 25-4-2012
Member 2 – Prof. S. C. Gupta		**Date:**
Member 3 – Prof. V. M. Datar		**Date:** 25-4-12

Final approval and acceptance of this dissertation is contingent upon the candidate's submission of the final copies of the dissertation to HBNI.

I hereby certify that I have read this dissertation prepared under my direction and recommend that it may be accepted as fulfilling the dissertation requirement.

Date: 25.4.2012

Place: Trombay, Mumbai

A. G. Wagh.
(Guide)

STATEMENT BY AUTHOR

This dissertation has been submitted in partial fulfillment of requirements for an advanced degree at Homi Bhabha National Institute (HBNI) and is deposited in the Library to be made available to borrowers under rules of the HBNI.

Brief quotations from this dissertation are allowable without special permission, provided that accurate acknowledgement of source is made. Requests for permission for extended quotation from or reproduction of this manuscript in whole or in part may be granted by the Competent Authority of HBNI when in his or her judgment the proposed use of the material is in the interests of scholarship. In all other instances, however, permission must be obtained from the author.

SOHRAB ABBAS

DECLARATION

I, hereby declare that the investigation presented in the thesis has been carried out by me. The work is original and has not been submitted earlier as a whole or in part for a degree / diploma at this or any other Institution / University.

SOHRAB ABBAS

DEDICATED TO MY FATHER

Over the years, I have practiced quantum mechanics with zeal and spirits and subscribed to its Copenhagen interpretation which states unless you observe an object it's not there, it exists only in the coherent superposition of all the possibilities. My father though left his physical body in January 2007 but I continue seeing him in the same state he was, when alive. I feel him around, his blessings, his teachings…but I miss his unwavering support, advice,…… assuring voice..... his comforting hug……..greatest salutations to most special individuals…..most precious gift of GOD to me…. my mother (Late Ms. Perveen Bano) and father (Late Mr. Fazal Abbas) ……..

ACKNOWLEDGEMENTS

I sincerely, thank my senior colleague, teacher and research advisor, Prof. Apoorva G. Wagh, for believing in me, guiding, inspiring and supporting me during my thesis work. I also thank him for introducing me to this beautiful world of quantum physics using neutrons and for his great zeal and unwavering patience with which he explained me the neutron dynamical diffraction. His intuition, work ideas, detailed knowledge and unending quest to arrive at the correct mathematical formulas consistent with physics provided me with an invaluable and exciting experience and benefitted me a lot.

I would also like to gratefully acknowledge and thank my all colleagues and coworkers, Prof. W. Treimer, Drs. M. Strobl, R. Loidl, T. Potocar, H. Lemmel and Prof. H. Rauch. Special thanks are due to H. Lemmel for his good company in our June, 11 run of experiment at ILL. It is a pleasure to acknowledge skilled assistance of Smt. M. Sharma of TP&PED, R. Mittal of SSPD, S.S. Patil of CDM, S.S. Jadhav of Spectroscopy Division, D. Sahoo of TP&PED, members of Chemie lab, HZB, O. Ebrahimi, S. Keil, P. Walter, R. Monka, other students of Prof. W. Treimer, V.K. Aswal and D. Sen, at various stages of this work and HZB and ILL (hospitality during experimental runs).

I am very thankful to the members of doctoral committee which comprised of Prof. S.V.G. Menon, Prof. S.C. Gupta, Prof. S.L. Chaplot, Prof. V. Datar and Prof. A.G. Wagh. I am indebted to them for their valuable time and pain that they took to monitor the progress of the work and their valuable suggestions.

I gratefully acknowledge all my teachers, my family members specially my sister, my colleagues at BARC and my friends who have greatly contributed towards my evolution and supported me.

And last but not the least, I would like to express my very special thanks to my wife Mariyam Fatima, for being a very special part of me. I am indebted to her with extreme sense of gratitude for the love, help and support that she has been showering through the period of our togetherness. Special thanks are due for her patience and encouragement during the writing of this thesis.

CONTENTS

Page No.

SYNOPSIS I-V

LIST OF FIGURES

Fig.1 Change in thermal neutron flux with time. Since 1970s, the neutron flux in research Reactors got stagnated due to technical limitations over the achievable power density, forcing to look for new types of neutron sources like spallation, fusion etc. [14]. 2

Fig.2 The distribution of scattering lengths as a function of atomic mass number A [5,119]. 14

Fig.3 Reciprocal space representation of the Bragg diffraction in a single crystal. 18

Fig.4 Asymmetric (a) Bragg and (b) Laue configurations of neutron incidence on a single crystal. 20

Fig.5 Reciprocal space diagram of the Laue diffraction in a single crystal. 25

Fig.6 The intensities of the forward (I_O) and diffracted (I_H) beams exiting a parallel face crystal slab in the symmetric Laue configuration as a function of the reduced incidence angle y for the slab thickness t = 20.25 Δ_S [4]. 30

Fig.7 Operating principle of a symmetric LLL IFM. 31

Fig.8 Intensities of the forward (O) anddiffracted (H) beams emerging from a symmetric LLL interferometer ($t_S=t_M=t_A=t=20.25\Delta_S$) as a function of the reduced incidence angle y for $\chi = 0$ (solid curves) and $\chi = \pi$ (dashed curves) [4]. 34

Fig.9 Neutron propagation through amorphous and single crystal prisms. For the single crystal prism, additional beams emerge from front and side faces and the transmitted beam undergoes a significant lateral displacement. 36

Fig.10 Boundary conditions on wave vectors dictate the allowed wave vectors at incidence and exit faces of an amorphous prism in reciprocal space. 38

Fig.11 Calculated variation of δ_{am} with incidence angle for A=90^o and n=1-10^{-5}, exhibits a minimum when both the incidence and exit angles equal. 39

Fig.12 Bragg diffraction of a neutron beam from a thick single crystal in real space. 40

Fig.13 Bragg diffraction of a neutron beam in reciprocal space. At each incidence angle, continuity of tangential components of wave vectors across the incidence and exit faces of the prism yields unique tie points as well as internal and emergent wave vectors (see text). 41

Fig.14 Variation of the diffracted (I_D) and transmitted (I_O) beam intensities with the angle of incidence for different apex angles A. 43

Fig.15 Calculated δ_{cr} and I_O for a symmetric Bragg prism. 46

Fig.16 Calculated δ_{cr} and I_O for an asymmetric Bragg prism. 46

Fig.17 Calculated δ^b_{cr} and I^b_{cr} for an asymmetric Bragg prism. 48

Fig.18 Experimental layout to measure neutron deflection and transmission by a Bragg prism. The set up employs 7X7 reflections each in the monochromator and analyser channel-cut crystals of a 5.24 Å neutron beam with a silicon prism suspended in each crystal between 3rd and 4th reflections and sample (Bragg prism) was placed between the monochromator and analyser. 50

Fig.19 Bragg reflection intensity fraction as a function of prism rotation for the symmetric Bragg {111} prism reflection with apex angles A of (a) 56.7^o and (b) 90^o, respectively. 51

Fig.20 Bragg reflection intensity fraction as a function of prism rotation for the

Asymmetric Bragg {111} prism reflection with asymmetry angles θ_S and apex angles A being (a) 35° and 94° (b) 41° and 98°, respectively. 52

Fig.21 Typical Voigt function fits (curves) to the direct and deflected beam scans (points) for an asymmetric Bragg prism: θ_S=41° and A=98° at off Bragg condition (θ= -12.85) (top) and near Bragg condition (θ= -4.85) (bottom). 55

Fig.22 Experimental (points) and theoretical (curves) values of δ_{cr} and I_O for a Symmetric Bragg prism with A=56.7°. 56

Fig.23 Experimental (points) and theoretical (curves) values of δ_{cr} and I_O for a symmetric Bragg prism with A=90°. 56

Fig.24 Experimental (points) and theoretical (curves) values of δ_{cr} and I_O for an asymmetric Bragg prism: θ_S=35° and A=94°. 57

Fig.25 Experimental (points) and theoretical (curves) values of δ_{cr} and I_O for an asymmetric Bragg prism: θ_S=41° and A=98°. 57

Fig.26 Asymmetric Bragg prism diffraction (schematic). Outside the total reflectivity domain, unreflected neutrons traverse the prism at an angle Δ to the incidence surface and exit the side face in diffracted (I_H) and forward diffracted (I_O) beams. At large enough angles Δ, neutrons reach the part of the side face cut along the diffracted beam direction and exit wholly into the I_O beam, thus truncating I_H on the larger-|y| side as well to yield a tail-free, sharp angular profile. 59

Fig.27 Bragg diffraction of a neutron beam in reciprocal space. At each incidence angle, continuity of tangential components of wave vectors across the incidence and exit faces of the prism yields unique tie points as well as internal and emergent wave vectors. 61

Fig.28 Theoretical curves for Si {111} Bragg reflection and prism diffraction of 5.26 Å neutrons with A=172^o and θ_S=50.1^o as a function of the incidence angle. 64

Fig.29 Exit angle as a function of incidence angle and Diffracted intensity for the Bragg prism monochromator with A=160^o and θ_S=50.1^o. For A<A_x, neutron exit angles corresponding to incidence angles on the two sides of the Bragg reflection do not overlap yielding two separated peaks. 65

Fig.30 Exit angle as a function of incidence angle and Diffracted intensity for Bragg prism Monochromator (A_x =166.85^o and θ_S=50.1^o). For A=A_x, exit angles of neutrons corresponding to incidence angles on the two sides of the Bragg reflection become exactly equal and peaks begin to overlap for A even slightly greater (e.g., A =167.4) than A_x (inset). 66

Fig.31 Exit angle as a function of incidence angle and Diffracted intensity for the optimised Bragg prism monochromator (A= 172^o and θ_S=50.1^o). At this A, exit angles of neutrons corresponding to incidence on the two sides of the Bragg reflection significantly overlap to yield a single peak with long tails.. 67

Fig.32 Exit angular profiles of prism diffraction (theory) for parameters as in Fig.28. Long tails of the large curves obtainable with the Bragg prism get clipped (small curves) on cutting the prism side face along the diffracted beam direction beyond a depth of 5 mm. 68

Fig.33 Theoretical flat-topped angular profile of the optimally tailored Bragg prism monochromator (A=172^o and θ_S=50.1^o). The angular width at zero intensity of the net peak is ($\theta_H|_{y=1} - \theta_H|_{y=-1}$)=0.86 arcsec. 69

Fig.34 Numerically computed acceptance curve of the optimal Bragg prism analyser

(A=16^{o} and θ_S=−51^{o}) for 5.26 Å neutrons (theory) and its convolution with the monochromator angular profile of Fig.33. 69

Fig.35 SUSANS experimental arrangement of the optimised monochromator-analyser pair of Si {111} Bragg prisms. A translation of the monochromator chooses between its Bragg reflection and prism diffraction to illuminate the analyser. Cd sheet downstream of the analyser can be translated to allow or forbid the analyser Bragg reflection into the detector (not shown). 71

Fig.36 Photographs of Bragg prisms. Top: Monochromator-analyser setup. Bottom: Three monochromators and one analyser (3rd from the left). 73

Fig.37 Bragg reflection from the θ_S=53.5^{o} monochromator observed with prism diffraction (cf. inset) of the optimal analyser. 75

Fig.38 Bragg reflection rocking curve of the monochromator (A=172^{o} and θ_S=50.1^{o}) observed with Bragg reflection and prism diffraction (cf. inset) of the optimal analyser. 76

Fig.39 Bragg Prism diffraction rocking curve of monochromator (A=172^{o} and θ_S=50.1^{o}) observed with Bragg reflection and prism diffraction (cf. inset) of the optimal analyser. 76

Fig.40 1st sub-arcsec neutron collimation: observed (data points) and calculated (curve) rocking curves (cf. inset) for prism diffractions of the monochromator (A=172^{o} and θ_S=50.1^{o}) and the optimal analyser. 77

Fig.41 SUSANS spectra without and with a sample holder, viz. a pair of overhead projection transparencies. 78

Fig.42 First Q ~ 10^{-6} Å^{-1} SUSANS spectra without and with a Hydroxyapatite casein

sample. Least-squares fit to the sample spectrum (smooth curve) implies the instrument capability of characterising ~ 150 μm-size agglomerates in a sample. 80

Fig.43 Sphere size distribution inferred from Fig.42. 80

Fig.44 1st neutron diffraction pattern of a macroscopic grating (inset) of period d ~ 200 μm. The least-squares fit to the pattern (smooth curve) corresponds to a transverse coherence length of 175 μm, the highest value reported to date for Å wavelength neutrons. 83

Fig.45 Neutron diffraction pattern (points) from a macroscopic grating of period d ~ 200 μm and the least-squares fit (smooth curve) to the pattern. 85

Fig.46 Analyser rocking curve for an iron sample (top) and inferred scattering length density distribution (bottom). 86

Fig.47 Analyser rocking curve for amorphous aluminium prisms of apex angles 120^o (top) and 90^o (bottom) to observe ~ arcsec deflections. 87

Fig.48 Theoretical flat-topped angular profile from the optimally tailored Bragg prism monochromator ($A=172^o$ and $\theta_S=50.1^o$) for 1.75 Å neutrons. 90

Fig.49 Theoretical acceptance curve (black) of the optimal Bragg prism analyser ($A=16^o$ and $\theta_S=-51^o$) for 1.75 Å neutrons and its convolution (red) with the monochromator angular profile of Fig.48. 90

Fig.50 Our proposal depicting the phase measurement by recording the interferograms with the thick sample placed alternately in subbeams I and II of the symmetric LLL IFM. 91

Fig.51 In a symmetric LLL IFM, neutrons of wavelengths λ and $\lambda+\delta\lambda$ propagate at corresponding Bragg angles θ_B and $\theta_B+\delta\theta_B$ to the IFM Bragg planes and hence

are incident at angles θ and $\theta+\delta\theta_B$ on the sample. Neutron refraction at the air-sample interfaces introduces a small correction to the phase due to the sample. 93

Fig.52 Phase dispersion in a 26.5 mm thick Si sample placed on path I of an IFM as a function of neutron incidence angle θ at central wavelength λ_0 (=5.14Å). The phase becomes nondispersive only for incidence at the Bragg angle θ_B and hence mandates sample alignment to arcsec precision. 94

Fig.53 Variation in the difference Φ_I-Φ_{II} between phases arising with the sample on paths I and II with θ near θ_B for three wavelengths (top). The approximate phases for λ_0 are also shown (bottom). Φ_I-Φ_{II} remains nondispersive over ~ arcminute, relaxing the required sample alignment precision. 97

Fig.54 Variation of the allowed sample thickness with Bragg angle of the IFM. 99

Fig.55 The experimental setup (schematic) employing a large symmetric LLL IFM with dual sample placed in subbeam II. 103

Fig.56 Dual Si-sample mounted on a plate. 104

Fig.57 A photograph of the experimental setup at S18 ILL, depicting a pair of amorphous Si prisms each of 120^o apex angles placed before the symmetric {220} LLL IFM to remove the λ/2 from monochromatic neutron beam. Dual sample mounted on a plate, is hanging from the top. 106

Fig.58 Optimisation of the sample rotation and tilt. 109

Fig.59 Typical interferograms for path I and II as a function of phase flag. 110

Fig.60 Variation in phase with the interferogram oscillation frequency normalised to that expected theoretically. 110

Fig.61 Oscillation frequency and phase with scan number. 111

Fig.62 Interference contrast and average intensity. 111

Fig.63 Path I, II and I-II phases during the run. 112

Fig.64 Metrological mapping of the Si sample thickness along with the neutron trajectories in paths I and II. 112

Fig.65 Average intensity with the sample placed IN and OUTSIDE paths I and II. 114

Fig.66 Interference contrasts with the sample placed IN and OUTSIDE in paths I and II. 114

Fig.67 Optimisation of the sample rotation and tilt. 115

Fig.68 Interferograms with the sample placed in paths I and II. 115

Fig.69 New metrological mapping of Si dual sample. 116

LIST OF TABLES

Table 1: Isotopic abundance, spin, neutron scattering lengths and cross sections for the Si. 15

Table 2: Observed deflection sensitivities, corresponding transmissions and percentage variations in the deflections for various Bragg prisms from their respective amorphous prisms. 58

Table 3: Comparison between various $\Delta b_c/b_c$ contributions at Ioffe et al. [127] and our proposal for a Si sample. 101

Table 4: Comparison between various $\Delta b_c/b_c$ contributions at Ioffe et al. [127] and in the proposed experiments with dual Si-sample. 105

CHAPTER 1 Introduction 1

1.1 Introduction 1

1.2 Background and brief literature survey of dynamical diffraction and neutron optics 4

1.3 Motivation and scope of the thesis 9

CHAPTER 2 Optics and dynamical diffraction theory of neutrons 13

2.1 Scattering length: Basic relations 13

2.2 Dynamical diffraction from a single crystal 16

2.2.1 Boundary conditions and diffraction geometries 19

2.2.2 Bragg Case 20

2.2.2.1 Neutron collimation 23

2.2.3 Laue Case 24

2.2.3.1 Energy flow and Pendellösung oscillation 27

2.2.3.2 Symmetric Laue Case 29

2.3 Symmetric LLL neutron interferometer operation 30

2.4 Detectors 35

CHAPTER 3 Neutron forward diffraction by Bragg prisms 36

3.0 Amorphous prism 37

3.1 Neutron forward diffraction 40

3.2 Forward diffracted intensity fraction 42

3.3 Neutron deflection 44

3.3.1 Bragg prism 44

3.3.2 Back Face contribution to neutron forward diffraction 47

3.4 Experimental 49

3.5 Results and Discussion 53

CHAPTER 4 First sub arcsec collimation of monochromatic neutron beam 59

4.0 Introduction 59

4.1 Bragg prism diffraction 60

4.2 Bragg prism design 63

4.3 Experimental 72

4.3.1 Bragg prism preparation 72

4.3.2 Expeiment 74

4.3.3 1st ever sub arcsec collimation 74

4.4 Applications of novel SUSANS set up 78

4.4.1 Super Ultra small angle neutron scattering (SUSANS) of a protein sample 78

4.4.2 Coherence properties of the beam 81

4.4.3 Versatility of the instrument 85

4.5 Tightening the neutron collimation still further 89

CHAPTER 5 High precision determination of the neutron coherent scattering length 91

5.0 Introduction 91

5.1 Our proposal: Theory 92

5.1.1 Achieving high precision b_c through optimisation of various parameters 99

5.1.2 Dual nondispersive phase shifter 102

5.2 EXPERIMENTAL 106

5.2.1 Recording of the interferograms 107

5.2.2 Data analysis 108

5.2.3 Repeat Experiment 113

CHAPTER 6 Conclusion and Future directions 119

REFERENCES 124

SYNOPSIS

The present thesis aims to elucidate intricacies of the dynamical diffraction theory and its applications in design, fabrication and operation of novel neutron optical devices. The thesis consists of 6 chapters.

Chapter 1 focuses on introducing neutron optics in single crystals which requires detailed understanding of the dynamical diffraction theory. After enumerating various advantages and application areas of neutrons, I briefly review the work done by earlier researchers on neutron optics, neutron dynamical diffraction theory and neutron interferometry. Inability of kinematical theory to explain diffraction from a single crystal and therefore, the need for dynamical diffraction theory is briefly discussed. The last Section of this chapter details the motivation and scope of the thesis. In this Section, some imposing problems associated with neutron optics and limitations/restrictions arising due to these in neutron related research areas, e.g., accessing smaller wave vector transfers in scattering experiments, difficulties in controlling neutron deflections and precision measurement of neutron coherent scattering length, are described. The solutions to these problems form the core of this Ph.D. thesis.

The Chapter 2 presents the basic theoretical framework underlying our work on neutron dynamical diffraction and its application in neutron optics. Dynamical diffraction theory addresses incidence of a neutron plane wave on a single crystal represented by a 3-D periodic nuclear potential, within the elastic scattering limit. All possible solutions of the corresponding time-independent Schrödinger equation constitute the dispersion surface in the reciprocal space. Boundary conditions at the vacuum-single crystal interface then pick unique neutron wave vector and wave amplitude solutions. The Bragg case has been dwelt upon (Section 2.2.2) keeping in view its importance in neutron monochromatisation and collimation. The Laue case has been

discussed in detail in Section 2.2.3 with special emphasis on the symmetric Laue case due to its wide use in the perfect crystal LLL interferometer (Section 2.2.4). For the sake of completeness, nuclear reactions exploited for neutron detection in all our experimental work are presented in the last Section of this Chapter.

In Chapter 3, I present the first ever calculations and experimental observations of the deflection and intensity fraction of neutrons forward diffracted by a single crystal prism as a function of the angle of incidence θ. For neutron incidence on a single crystal prism near a general asymmetric Bragg reflection, I delineate Bragg reflection at the incidence face and diffraction and forward diffraction at the side face of the prism in Section 3.1. Sections 3.2 and 3.3 present analytic expressions for the intensity fraction $I_O(\theta)$ and deflection $\delta_{cr}(\theta)$ of forward diffracted neutrons. In the vicinity of a Bragg reflection, $\delta_{cr}(\theta)$ deviates sharply from δ_{am} for an identical amorphous prism, reaching opposite extrema at either end of the total reflectivity domain and exhibits a 3 orders of magnitude greater sensitivity to the incidence angle. We have coined the term 'Bragg prism' to name this device. The neutron deflection and transmission from a Bragg prism are governed by the apex angle A, the Bragg reflection {h,k,l} and the angle between the Bragg diffracting planes and incidence surface of the prism, as illustrated with various Bragg prism configurations. For a suitably selected Bragg prism configuration, the deflection can even change sign on the low θ side. Sections 3.4 and 3.5 describe experimental observations of $I_O(\theta)$ and $\delta_{cr}(\theta)$ across the Bragg reflection for several silicon Bragg prism. The observed Bragg prism deflections deviate from amorphous prism deflections by up to 27% with variations of deflection up to 0.43 arcsec per arcsec variation in incidence angle [1-7].

Chapter 4 dwells upon preparation of a nearly plane wave neutron beam by employing an optimally designed Bragg prism and scoring several experimental firsts with it. In Section 4.1,

analytic expressions for intensity fraction I_H and exit angle θ_H of neutrons diffracted from a Bragg prism, are derived. With a judicious choice of the Bragg reflection, its asymmetry and the apex angle, a Bragg prism can collimate a neutron beam to sub-arcsec widths (Section 4.2). In conjunction with an analyser in the opposite asymmetry likewise tailored to accept a pair of even narrower peaks, it would yield a rocking curve comprising a pair of sub-arcsec peaks separated by up to a few arcsec. Experimental achievement of the first ever neutron beam of sub-arcsec widths is presented in Section 4.3. This novel setup has facilitated SUSANS (Super Ultra-Small-Angle Neutron Scattering) experiments probing wave vector transfers $Q \sim 10^{-6}$ Å^{-1} (Section 4.4) and hence characterisation of up to 150 μm-size agglomerates in samples. The transverse coherence length of 175 μm of the monochromated beam is the highest achieved to date, allowing us to record the first neutron diffraction pattern from a macroscopic grating of 200 μm period [8-16].

Chapter 5 describes high-precision interferometric determination of the coherent scattering length b_C by optimising various parameters of the experiment. A finely surfaced thick dual sample in the nondispersive configuration and a large interferometer (IFM) with spacious splitter-mirror and mirror-analyser gaps operating at a large Bragg angle reduce imprecision in previous b_C measurements down to a few ppm. It is then imperative to correct the b_C inferred from the observed phase for neutron refraction effects at the sample-ambient interfaces. The refractive index for neutrons can thus be determined to a phenomenal precision of a few parts in 10^{12}. Section 5.2 describes the interferometric experiment which thus determined b_C of silicon to within 27 parts in 10^6 [17-22].

Chapter 6 concludes this thesis and provides a summary of the main results and future directions for the use of these novel techniques and devices in research. It enumerates several firsts scored

by us in the field of neutron optics such as:

- Enunciation and observation of neutron forward diffraction by single crystal prisms which enables smooth control over the neutron deflection due to the arcsec/arsec sensitivity of the deflection to the incidence angle.
- Design, fabrication and operation of a novel Bragg prism monochromator-analyser pair which achieved the first rocking curve of sub-arcsec angular width.
- SUSANS (Super Ultra Small Angle Neutron Scattering) spectrum probing wave vector transfers $Q \sim 10^{-6}$ $Å^{-1}$.
- Neutron diffraction pattern from a macroscopic grating (period ~ 200 μm).
- Measurement of the largest non-dispersive phase (911 interference orders) to date, determining b_C to within 27 parts per million.

REFERENCES

[1] S. Abbas, A. G. Wagh, M. Strobl and W. Treimer, Nuclear Instruments and Methods in Physics Research A, **634** (2011) S144.

[2] A. G. Wagh, S. Abbas and W. Treimer, Journal of Physics (CS), **251** (2010) 012074.

[3] S. Abbas, A. G. Wagh, and W. Treimer, Pramana- J. Phys., **71** (2008) 1109.

[4] S. Abbas, A. G. Wagh, M. Strobl and W. Treimer, Sol. St. Phys. (India), **51** (2006) 351.

[5] M. Strobl, W. Treimer, Ch. Ritzoulis, A. G. Wagh, S. Abbas and I. Manke, J. Apl. Cryst., **40** (supplement) (2007) s463.

[6] A. G. Wagh, S. Abbas , M. Strobl and W. Treimer, BENSC experimental reports 2005 (HMI, Germany, 2006) 115.

[7] S. Abbas and A. G. Wagh, Sol. St. Phys. (India), **50** (2005) 317.

[8] A. G. Wagh, S. Abbas and W. Treimer, Nuclear Instruments and Methods in Physics

Research A, **634** (2011) S41.

[9] S. Abbas, A. G. Wagh, M. Strobl and W. Treimer, Journal of Physics (CS), **251** (2010) 012073.

[10] S. Abbas, A. G. Wagh, and W. Treimer, Sol. St. Phys. (India), **53** (2008) 555.

[11] A. G. Wagh, S. Abbas, and W. Treimer, Sol. St. Phys. (India) **53** (2008) 553.

[12] A. G. Wagh, S. Abbas, and W. Treimer, Pramana- J. Phys. **71** (2008) 1171.

[13] A. G. Wagh, S. Abbas and W. Treimer, BENSC Experimental reports 2007(HMI, Germany, 2008) 223.

[14] A. G. Wagh and S. Abbas, Sol. St. Phys. (India), **51** (2006) 353.

[15] A. G. Wagh, S. Abbas, M. Strobl and W. Treimer, BENSC experimental reports 2006 (HMI, Germany, 2007) 22.

[16] S. Abbas, A. G. Wagh, M. Strobl and W. Treimer, Sol. St. Phys. (India), **52** (2007) 441.

[17] S. Abbas, A. G. Wagh, R. Loidl, H. Lemmel and H. Rauch, AIP Conf. Proc., **1349** (2011) 501.

[18] A. G. Wagh, S. Abbas R. Loidl, H. Lemmel and H. Rauch, ILL Experimental reports **3-15-58**, 2009 (Grenoble, France, 2010).

[19] S. Abbas and A. G. Wagh, Pramana J-Phys., **63** (2004) 375.

[20] A. G. Wagh and S. Abbas, J. Res. Natl. Stad. Technol., **110** (2005) 237.

[21] A. G. Wagh, S. Abbas T. Potocar, H. Lemmel and H. Rauch, ILL Experimental reports **3-15-61**, 2011 (Grenoble, France, 2012) to be published.

[22] S. Abbas, A. G. Wagh, T. Potocar, H. Lemmel and H. Rauch, AIP Conf. Proc. (2011) submitted.

CHAPTER 1

Introduction

1.1 Introduction

Particle-wave duality forms the basis for optics and the dynamical diffraction of neutrons [1-5]. De Broglie's discovery [6] of the fundamental fact that a particle of mass m and velocity v behaves like a wave of wavelength λ given by

$$\lambda = \frac{h}{m v}, \tag{1}$$

paved the way for the unification of matter and radiation. Here symbol h signifies the Planck constant. Davisson-Germer [7] and Thomson [8] provided a firm experimental footing to the matter wave hypothesis by observing Bragg diffraction [9] of electrons from a Ni-single crystal. Chadwick's discovery of the neutron in 1932 [10] motivated Mitchell and Powers [11] to experimentally verify its wave nature by employing the Bragg diffraction of neutrons (from an MgO single crystal) with the neutron beam extracted from a Ra–Be source embedded in a paraffin moderator. However, the biggest and the most drastic boost to development of neutron physics came with Fermi's operation of a nuclear reactor in 1942. Neutrons produced by U^{235} fission in a research reactor have an average energy of 2MeV. They are slowed to thermal energies in a moderator (such as graphite, beryllium, heavy or light water) surrounding the fuel. The peak core flux of research reactors is typically in the range of 10^{14} cm^{-2} s^{-1} to 10^{15} cm^{-2} s^{-1}. To maximize the neutron flux density, it is necessary to increase the fission rate per unit volume, but the power density is limited by heat transfer and material properties [12]. In spallation sources, high intensity (mA) proton beams (typically) of energies in the GeV range strike a high Z target, producing approximately 20 neutrons per proton with energies in the fast and epithermal region. Existing

spallation sources yield peak neutron flux of 10^{16} $cm^{-2}s^{-1}$ and 10^{17} $cm^{-2}s^{-1}$ [13-15]. New neutron sources under study, based on inertial confinement fusion (ICF) will increase the neutron flux by many orders of magnitude (Fig.1) [14]. Neutron sources are inherently weak compared to X-ray sources. However, due to the importance of neutrons, numerous research reactors have been built around the world. To mention a few of them, state-of-the-art research reactors like 10 MW BERII in Helmholtz Zentrum Berlin and 20 MW FRM II in Munich (Germany) [16], 58 MW ILL reactor in Grenoble (France) [17], 100 MW Dhruva reactor in Mumbai (India) [18], 20 MW NIST [19] and LANL [20] in USA have been built and are operational. Next-generation spallation neutron source facilities e.g., SNS at Oak Ridge National Laboratory-U.S.A [21] and J-PARC at Tokai-Japan [22], have also become functional.

Extraordinary importance conferred to neutrons is due to its use both as a probe and as an object of

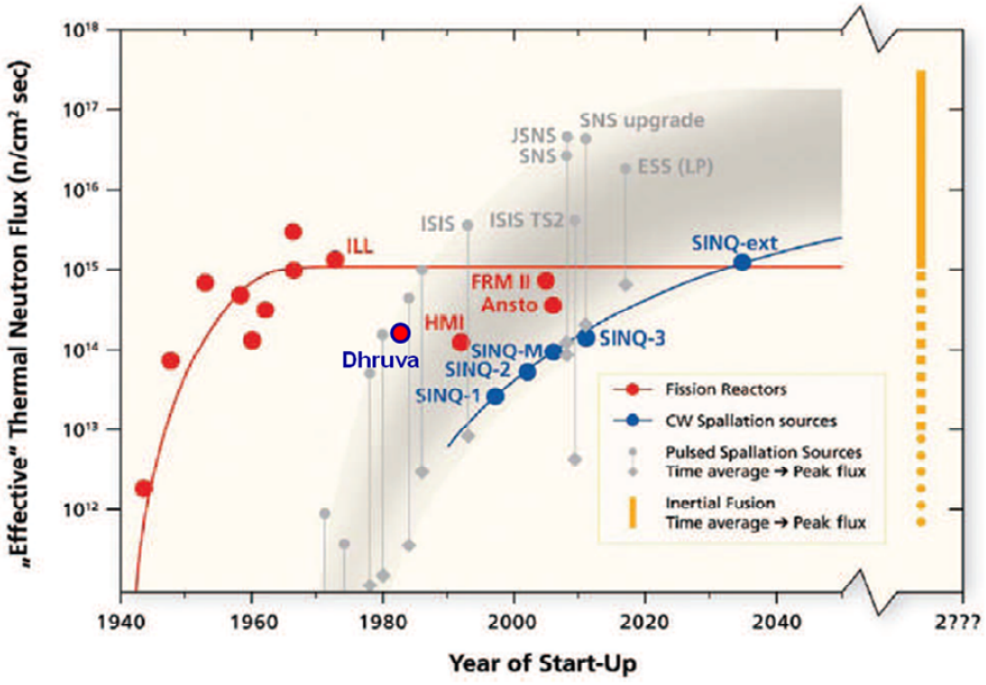

Fig.1 Change in thermal neutron flux with time. Since 1970s, the neutron flux in research reactors got stagnated due to technical limitations over the achievable power density, forcing to look for new types of neutron sources like spallation, fusion etc. [14].

study themselves due to their unique properties like large mass (~ 2000 times the e^- mass), short range strong interaction, essentially no electric charge, long life time, anomalous magnetic moment (μ_n=–1.913μ_N, μ_N being the nuclear magneton) etc. Responding to all known fundamental interactions viz. strong, electromagnetic, weak and gravitational, they are a powerful tool for addressing questions from the domains of particle physics, nuclear physics and astronomy [3, 23]. Neutrons especially in the thermal energy range ~ 25meV (in thermal equilibrium with a moderator at ~ 300 K), stand out as a unique probe for condensed matter. The significant advantages of thermal neutrons can briefly be summarised as [24-27]:

1. The thermal neutron energy (meV) is ~ energies of atomic motions. A wide range of energy scales may be probed, from the neV energies associated with polymer reptation, through molecular vibrations and lattice modes in meV to eV transitions within the electronic structure of materials.
2. The wavelengths of thermal neutrons (~ Å) are of the same order as atomic spacing in condensed matter. Through various neutron scattering techniques from diffraction to ultra small angle scattering, structural information over many orders of magnitude (~ Å to 10^4Å) in scale can be obtained.
3. Neutrons primarily undergo the strong interaction with nuclei, rather than the diffuse e^- clouds of atoms, in contrast to X-rays. Therefore n's can discern light atoms (e.g. hydrogen) in the presence of heavier ones, and distinguish neighbouring elements.
4. The neutron's magnetic moment is ideally suited to study microscopic magnetic structures and magnetic fluctuations.
5. Because of its charge neutrality and spin ½, the two component neutron spinor evolves in a magnetic field **B** through the interaction Hamiltonian $-\mu_n \boldsymbol{\sigma}.\mathbf{B}$, enabling observation of the

SU(2) phase, and separation of geometric and dynamical phases. Here **σ** signifies Pauli spin operator.

6. Neutrons are non-destructive, even to complex, delicate biological materials. They are highly penetrating, allowing non-destructive investigation of the interior of materials.

In spite of these advantages, neutrons have some disadvantages, e.g.,

1. Neutron sources are weak in intensity and the neutron flux at the sample is generally low in comparison to other sources like X-rays. Large samples and long experimental durations are hence required.
2. Other serious drawback is Kinematic restrictions viz., all energy and momentum transfers with neutrons can't be accessed with a single instrument.

Therefore, neutron instruments are designed to compromise between intensity and resolution and different types of instruments are required to achieve the best compromise for different types of measurements. So far, the greatest gains in instrument performance have come from improvements in neutron optics such as supermirrors and improved detectors (especially PSDs) and not from better sources, as the neutron flux hasn't risen appreciably over for the last 4 decades (Fig.1).

1.2 Background and brief literature survey of dynamical diffraction and neutron optics

The phrase "neutron optics" encompasses a wide range of optical elements which exploit the phenomena of reflection, refraction, interference and diffraction or combinations of these to focus, deflect, monochromate or manipulate neutron beams. Fermi [28] proposed in analogy with theory of refraction of light (or X-rays) that the interaction of neutrons with materials consists of coherent scattering, or re-radiation of the incident wave by individual scattering centres. His consequent introduction of Fermi pseudo potential forms the backbone of neutron optics for thermal neutrons.

Neutron optics has since made great strides in diverse directions. Many of the fundamental relations of neutron optics concerning magnetic effects in neutron scattering, theory of coherent and incoherent scattering, magnetic crystal diffraction, and refraction were developed in a series of papers by Halpern and co-workers [29-31] and Hamermesh [32]. Refraction, in analogy with visible photon optics, is described by introducing a refractive index n defined as the ratio of the neutron wave vector inside a material medium to that in vacuum. For most materials, n [see Chapter 2] differs from unity by about 10^{-6}-10^{-5}. The neutron refraction effects have been studied [33-38] extensively and applied to build lenses and prisms to respectively focus and deflect neutron beams. Refraction for thermal neutrons, though miniscule, has been effectively used to observe a focusing effect using symmetric concave lenses made of amorphous MgF_2 [39], stacked layers of small amorphous prisms and stacked Fresnel-shape discs [40-42]. Spin dependent refraction using a quadrupole magnet was observed by Oku et al., [43].

Materials with n less than unity effect total external reflection of neutrons incident at grazing angles less than the critical angle θ_c given by

$$\cos\theta_c = n. \qquad (2)$$

Neutron transportation through a neutron guide tube, the inner wall of which is made of a material with $n<1$, is based on total external reflections. The principle and the design were proposed by Maier-Leibnitz [44]. Ultracold neutrons (UCN) which have speeds < 10 m/s, i.e., wavelength $\lambda >$ 400 Å and E < 500 neV, get totally reflected and bounce elastically from the material walls at all angles of incidence including normal incidence as neutrons with such energies (~100 neV) can't overcome the optical potential barriers of most materials [36,45]. Some extremely important questions pertaining to fundamental physics [44-47], have been addressed using UCN. The effect of the magnetic interaction on n is merely to add a term of opposite signs for the two spin states

[33-34,48]. The bi-refracting nature of ferromagnetic materials which provides two different critical angles for two spin states of neutrons (± ½) forms the basis for the production of polarized neutrons through selection of one component only, and super mirrors guides [49-50]. Magnetic confinement of ultracold neutrons also relies on the same principle and only one spin state can be confined [36,45].

Diffraction: I. Kinematic Diffraction

The kinematical theory of diffraction considers the scattering of the incident wave from atoms in a crystal, but ignores further interactions of scattered wavelets within the crystal. Born approximation [51-52] is applied to calculate the scattering amplitude. Assuming the wave amplitude incident on each nucleus inside the crystal to be same, the total diffracted amplitude is obtained simply by adding the individual amplitudes diffracted by each atom, taking into account the phase differences between them. Distribution of diffracted amplitudes in the reciprocal space is then the Fourier transform of the distribution of nuclear scattering length density in the real space. The integrated reflected intensities calculated thus, are proportional to the square of the structure factor and to the volume of crystal. The diffracted intensity becomes infinity if the crystal thickness is increased to infinity, which is unphysical. The theory can only be applied to measure diffracted intensities and their peak positions for a weak optical potential and extremely small crystals or polycrystalline materials. Further, it is difficult to obtain the phase information of the diffracted wave [24-27]. Therefore, for perfect or nearly perfect crystals, a more complete theory which takes into account further interactions of the scattered radiation with matter ought to be developed.

II. Dynamical diffraction

Dynamical diffraction theory for neutrons as well as X-rays owes its birth to the availability [53] of pure, defect free and large single crystals in late 40's. Several discrepancies between experimental observations and predictions of kinematical theory showed that the theory was ill-equipped to deal with scattering from perfect crystals. The applications of neutron dynamical diffraction include mainly neutron optics, measurement of scattering lengths, neutron interferometry, imaging of defects, multiple Bragg diffraction and grazing incidence diffraction.

Dynamical diffraction theory for X-rays was developed much before neutrons and the immediate stimulus for this development was observation of Bormann effect [38] for X-rays. X-ray Dynamical diffraction theory of a plane wave by a perfect crystal was formulated by Darwin [54] and Ewald [55], using two different but original approaches. Two beam plane wave dynamical diffraction which considers only an incident beam and one Bragg diffracted beam has been the main focus of theoretical development since then. The theory was extended to multiple Bragg diffracted beams later. Prins [56] extended the Darwin's theory to take absorption into account, and von Laue [57] reformulated Ewald's approach which forms the backbone of the modern-day dynamical theory. Reviews and extensions of the theory have been given by Zachariasen [58], James [59], Kato [60] and Authier [61]. A comprehensive review of the Ewald-von Laue theory has been provided by Batterman and Cole [37]. More recent reviews are provided by Kato [62], Pinsker [63] and Authier [64-65].

There exists a one to one correspondence between dynamical diffraction theory of X-rays and neutrons [65] with an important difference being that for neutrons unlike X-rays, absorption is weak in most materials. Since the first observation of the Pendellösung fringe structure in a neutron diffraction experiment, using single crystals of Si, by Shull about 43 years ago [66], interest in the

application of the dynamical theory to the neutron case has grown substantially. A concise review with focus on the work presented in this thesis is given in Chapter 2. Some excellent papers and reviews already exist on the theory for example, by Sears [67-68], Rauch and Petrascheck [1,69], Wagh and Rakhecha [4,70] and Klein and Werner [5]. Extension of the dynamical diffraction theory for magnetic case is provided by Stasis and Oberteuffer [69,71]. Many of the theoretical predictions of neutron dynamical diffraction have since been verified and exploited for applications. Knowles in 1956 showed that the intensity of neutron capture γ-radiation varies markedly close to a Bragg condition for $CdSO_4$ single crystals [72]. This was the first effect of dynamical diffractions of neutrons demonstrated experimentally. Thereafter, anomalous transmission of neutrons associated with α-branch of the dispersion surface was experimentally verified by Sippel et a1. [73] and Shilshtein et a1. [74] using InSb crystals. The angle amplification effect was exploited by Kikuta et a1. [75] and Zeilinger et al. [76] to measure small directional changes of a neutron beam resulting from prism refraction. In a TOF (time-of-flight) experiment, Shull [77] could also observe 'anomalous' speed reduction by a factor $\cos\theta_B$ within a single crystal. The effects of a finite curvature of the incident wavefront can be accounted for by using the spherical wave approach [78]. Shull and Oberteuffer [66,78] used the Laue collimator setup to measure the fringe shift with the displacement of the exit slit along the crystal face. The experiment [79] showed that the phenomenon ought to be described in terms of a spherical incident wave. The interest and activities in neutron dynamical diffraction theory and its applications, reached the crescendo with the successful operation of the 1st perfect-crystal neutron interferometer (IFM) by Rauch-Treimer-Bonse [80] in 1974 by exploiting the amplitude division of the neutron wave function in the symmetric Laue configuration. However, a perfect-crystal X-ray IFM [81] was conceived and realized 9 years earlier. The first neutron IFM was built by Maier-Leibnitz and

Springer though in 1962, that used the wavefront division. Biprism (refraction based) IFMs suffer from small beam separations (~ 60 μm) making measurements with samples placed in one of the interfering paths extremely difficult [82]. To overcome this, various IFMs based on amplitude division have been developed for different requirements [Chapter 3, 1,4,83-84]. Among these, the LLL IFM (both skew symmetric and symmetric case) is the most widely used. Neutron interferometry has been a testing bed for the concepts of quantum mechanics. Many of the hypotheses previously treated only in thought experiments have since been verified neutron interferometrically. Some of these landmark experiments include observation of 4π spinor periodicity [85-87] and gravitational phase shift measurement [88], separation of geometric and dynamical phases [89], observation of Aharonov-Anandan-Casher (AAC) [90-91] and scalar Aharonov-Bohm (AB) effects [92-93], confinement induced phase [94], coherence length measurements [95-96] and experiment for testing quantum contextuality with single neutrons [97]. These alongwith some other experiments and many more interesting proposals are well documented [1,4,98-107].

1.3 Motivation and scope of the thesis

With neutron optics lying at the very heart of every neutron instrument, it becomes challenging indeed to match new experimental requirements with better instruments and novel optical components. Single crystal neutron optics plays a pivotal role in development of some of the key components of neutron instruments. In this section, we describe some of the neutron optics issues needed to be resolved, present motivation for their solution and circumvent them through new optical devices coupled with novel ideas. This opens up new vistas for the many experiments which otherwise are not possible (Chapters 3-5).

I. One of the major disadvantages of neutrons, also shared by X-rays, is their very small magnitude of refractive power $|n - l| \sim 10^{-6}$–10^{-5} [4-5]. Therefore, thermal neutrons traversing an amorphous prism undergo a deflection in the arcsec regime and a few-degree variation in the incidence angle brings about only ~ arcsec change in the neutron deflection. Further, contrary to light, since refractive index is usually smaller than unity for neutrons, the deflection will be towards the apex of prism. Schneider and Shull [108] have carried out precision measurements of prism deflection angles from which refractive indices, and hence scattering lengths, were determined. Wagh and Rakhecha [109] showed that for neutron propagation parallel to the prism base, the neutron deflection just equals the product of the refractive power and base-height ratio of the prism. Over the past five decades, variations of the forward diffracted (I_O) and diffracted (I_H) intensities from single crystal prisms with the incidence angle have been observed for X-rays [38,110] and neutrons [79]. Due to the nonavailability of arcsec wide neutron beams at that time however, the neutron $I_H(\theta)$ variation could only be mapped by scanning a narrow slit across the diffracted beam. However, deflection sensitivities of the amorphous prisms remained abysmally low. In Chapter 3, we overcome this problem by presenting a novel Bragg prism, viz., a single crystal prism operating in the vicinity of a Bragg reflection, offering deflection sensitivity of more than three orders of magnitude greater than an amorphous prism achieved with a 2 arcsec wide neutron beam [111-112].

II. Experimenters' insatiating thirst for more and more parallel monochromatic neutron beam, has led to development of numerous types of monochromator–collimator setup using single crystal [4,24-27]. Ultra-small angle neutron (or X-ray) scattering (USANS/USAXS) studies [113] which probe wavevector transfers $Q \sim 10^{-5}$ $Å^{-1}$, require an incident beam collimation down to a few arcsec, to characterize samples [26-27,114] containing agglomerates of μm dimensions. A Bragg

diffracted neutron beam from a single crystal monochromator is typically a few arcsec wide but with long tails. The Darwin profile is sharper, with an intensity nearly half that for the Ewald profile in the tail region. Yet even the Darwin tail intensity drops gradually, in inverse proportion to the square of the incidence angle measured from the centre of Bragg reflection. Bonse and Hart in 1965 [115] proposed a number p of successive identical Bragg reflections from two slabs of a channel-cut monolithic single crystal to achieve collimation without the tail contamination. The tails of the multiply reflected intensity fraction R^p (R<1) get trimmed drastically leaving the peak (R=1) essentially unaltered, R denoting the reflectivity for each Bragg reflection. Such a beam thus has a nearly rectangular angular profile, a few arc sec wide. However, efforts to achieve such a top hat angular profile for X-ray [116] and neutron [117–118] beams yielded tail intensities a few orders of magnitude higher than expected. However, such a tail-free Darwin angular profile could be attained by Wagh et al. [111] only in 2001. The angular width achievable is limited to that of Darwin angular profile width. Using an asymmetrically cut crystal, one reduces the Darwin width. Treimer et al. [112] however placed a Si-wedge after a few reflections to deflect neutrons before the remaining reflections, attaining an analyser rocking curve width ~2 arcsec. In order to achieve sub-arcsec collimation of neutrons, we devised a judiciously optimised Bragg prism. We address this issue in Chapter 4 by enunciating the novel analytical as well numerical calculations based on the dynamical diffraction theory, which leads to the optimised collimator configuration yielding sub-arcsec collimation.

III. In the low energy limit, scattering length is the only important parameter required to describe the strength and the character of the neutron – nuclear interaction. Scattering length values vary irregularly from one nucleus to another due to their strong dependence on the details of the nuclear structure. This makes precise determination of scattering length of low-energy neutrons for basic

nuclear physics very important as it would shed light on the basic nucleon- nucleon interaction, charge independence and charge symmetry of the nuclear forces and thus on validity of different nuclear models [1,2,68,119]. Neutron scattering studies of condensed matter clearly require accurate values for the coherent (b_C) and incoherent (b_I) scattering lengths of the elements present in the sample. There are many methods for b_C determination such as, Christiansen filter [120], mirror reflection [121-122], gravity refractometer [123], prism refraction [49,124] and transmission [125] etc. However, the most accurate value with a relative error of about 0.03% was obtained by Shull et al. [66,78-79] using the dynamical diffraction of neutrons from a Si single crystal in Laue geometry and observing the Pendellösung oscillation for various thicknesses of Si crystal.

Perfect crystal interferometry affords most precise determination of the coherent scattering length [1,2,4,69,119] of samples. Following Scherm's suggestion of placing the sample with its surface parallel to the Bragg planes of the interferometer to attain a wavelength-independent phase, Rauch et al. [126] determined b_C to within a few parts in 10^4. Ioffe et al. [127] reduced the b_C imprecision to a few parts in 10^5 by measuring the phase shift between two interferograms recorded with the sample placed alternately on the two beam paths of the interferometer in this non-dispersive configuration. Wagh and Abbas have proposed a comprehensive optimisation of this method to attain a further order of magnitude improvement in b_C precision and pointed out that a correction for neutron refraction at the air-sample interfaces would then become mandatory. Using a monolithic dual sample, proposed by Lemmel and Wagh [128], in the non-dispersive configuration, b_C has been determined with a precision of 27 parts per million [Chapter 5].

CHAPTER 2

Optics and dynamical diffraction theory of neutrons

This Chapter presents the basic theoretical framework underlying our work on neutron dynamical diffraction and its application in neutron optics. First, I briefly summarise the relevant results from the theory of neutron optics needed to understand the scattering length and its importance.

2.1 Scattering length: Basic relations

Thermal neutrons are scattered by a nucleus through the strong interaction. The strong interaction being short-ranged, the relevant impact parameter R (~ fm) is much smaller than the neutron wavelength λ (~ Å) and the neutron angular momentum $mvR = hR/\lambda < 10^{-4}\hbar$. Hence only $l = 0$ (s-wave) scattering need be considered which by the first Born approximation [51-52], is isotropic.

Consider a neutron plane wave $\psi_{inc} = e^{i\mathbf{k}\cdot\mathbf{r}}$ incident on a single nucleus bound within a solid sample. Here **k** denotes the incident wave vector. The condition of $kR<<1$ for thermal neutrons allow the introduction of a point-like interaction viz., the Fermi pseudopotential [28]

$$V(\mathbf{r}) = \frac{2\pi\hbar^2}{m} b_C \delta(\mathbf{r}). \qquad (3)$$

The symbol b_C denotes the coherent scattering length. At large distances, the neutron wave function after the scattering is written as the sum of incident plus scattered wave functions [5,24-27,52] i.e.,

$$\psi = e^{i\mathbf{k}.\mathbf{r}} - b_C \frac{e^{ikr}}{r}. \qquad (4)$$

Matching of the neutron wave function and its derivative at the radius R of the nucleus, forces coherent scattering lengths b_C to be positive most frequently [5], indicating a repulsive optical

potential for most nuclei in spite of the attractive nature of basic neutron-nuclear interaction. The dependence of b_C on the atomic mass (Fig.2) is quite irregular [119] with only a few nuclei displaying negative scattering lengths [5,131].

If all scattering nuclei are identical, neutrons scattered from different nuclei have a definite phase relationship and coherent scattering results. On the contrary, there is no definite phase relationship between waves from scattered different isotopes (isotopic incoherent scattering) or from nuclei with random spin orientations in the sample (spin incoherent scattering) [1-2,4,24-27,119,129-130].

If the sample contains different isotopes with fractional isotopic abundances f_i, distributed randomly, the coherent b_C, the isotopic incoherent b_I, and the total b, scattering lengths are computed by accounting for the isotopic abundances, viz.,

$$b_C = \sum_i f_i \, b_i \,, \tag{5}$$

$$b_I = \sqrt{\sum_{i \neq j} f_i \, f_j \left(b_i - b_j \right)^2} \tag{6}$$

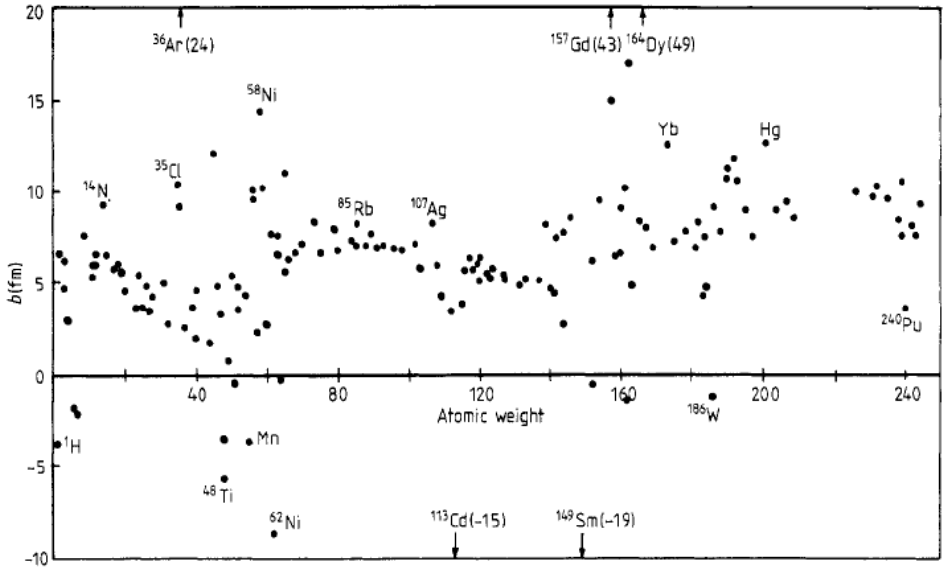

Fig2. The distribution of coherent scattering lengths as a function of atomic mass number [5,119].

and $b = \sqrt{\sum_i f_i b_i^2}$. (7)

Absorption is accounted for by a complex interaction potential and therefore by a complex scattering length

$$b_C^{'} = \sqrt{b_C^2 - \left(\sigma_{attn}/2\lambda\right)^2} - i\sigma_{attn}/2\lambda\,, \quad (8)$$

where the attenuation cross section σ_{attn} includes both absorption σ_a and incoherent scattering σ_I. The coherent, incoherent and total scattering cross sections $\sigma_C = 4\pi\left|b_C^{'}\right|^2 = 4\pi b_C^2$, $\sigma_I = 4\pi\left|b_I\right|^2$ and $\sigma_S (= \sigma_C + \sigma_I) = 4\pi\left|b\right|^2$ respectively of a bound nucleus, are determined by the moduli of the respective complex scattering lengths. In general, b_C varies for different isotopes of an element, allowing isotopic substitution methods to yield structural and dynamical information in great detail. It also facilitates the use of contrast variation to selectively mask specific components of a complex system to observe scattering only from the rest of the system in small angle neutron scattering (SANS) studies.

Table 1: Isotopic abundance, spin, neutron scattering lengths and cross sections for the Si.

Silicon	Abundance (%)	Spin	b_C (fm)	b_I (fm)	σ_C (barn)	σ_I (barn)	σ_a (barn)
$_{14}$Si	-	-	4.15071(22)	0.178	2.1633(10)	0.004(8)	0.171(3)
$_{14}Si^{28}$	92.2	0	4.106(6)	0	2.120(6)	0	0.177(3)
$_{14}Si^{29}$	4.7	1/2	4.7(1)	0.089*	2.78(12)	0.001(2)	0.101(14)
$_{14}Si^{30}$	3.1	0	4.58(8)	0	2.64(9)	0	0.107(2)

*For the isotope Si^{29} with a spin ½, b_I arises from different scattering lengths for the up and down spin states.

Due to the rapid strides made lately by the semiconductor electronics industry, most relevant properties of single crystal silicon have been determined to great precision over a wide temperature range. Single crystal silicon is therefore an ideal candidate for high precision b_C determination (cf. Chapter 5). For Si, $\sigma_{attn}/(2\lambda\, b_C) \sim 10^{-5}$ for 2Å neutrons, implying negligible neutron absorption and incoherent scattering. Some important neutron scattering properties of silicon cited in literature [119] are summarised in the Table 1.

2.2 Dynamical diffraction from a single crystal

The dynamical theory [1,4,54-70] regards the incident and diffracted waves inside the crystal to be coherently coupled forming a composite wave function

$$\psi(\mathbf{r}) = \psi_O e^{i\mathbf{K_O}\cdot\mathbf{r}} + \sum_H{}' \psi_H e^{i\mathbf{K_H}\cdot\mathbf{r}}, \tag{9}$$

which behaves as a single entity. The sum extends over all reciprocal lattice vectors. The internal wave vectors $\mathbf{K_O}$ and $\mathbf{K_H}$ are related through the Bragg condition

$$\mathbf{K_H} = \mathbf{K_O} + \mathbf{H}. \tag{10}$$

The interactions between the waves and the crystal are represented by the potential

$$V(\mathbf{r}) = \sum_H V_H e^{i\mathbf{H}\cdot\mathbf{r}} = V_O + \sum_{H\neq 0} V_H e^{i\mathbf{H}\cdot\mathbf{r}} \tag{11}$$

with

$$V_H = \frac{2\pi\hbar^2 N b_c}{m}\frac{F_H}{F_O} = \frac{\hbar^2 k_0^2}{2m}\chi_H\,. \tag{12}$$

Here m stands for the neutron mass, F_O and F_H, the structure factors for **O** and **H** reflections respectively, N, the atomic number density, χ_H, the susceptibility for the **H** reflection and b_C, the coherent scattering length.

Matters get simplified while dealing with the two-beam case, wherein only one reciprocal lattice point is close enough to the Ewald sphere to excite the corresponding diffracted wave. Thus for a plane wave, exp(i$\mathbf{k_O}$.$\mathbf{r}$), incident on the crystal near the Bragg condition for a single reflection **H**, only two terms in the series (Eq.(9)) for the internal wave function need be considered, the amplitudes of all other terms being negligibly small. On solving the time-independent Schrodinger equation involving the potential (Eq.(11)) with such a wave function, one obtains the dispersion relation

$$(K^2 - K_O^2)(K^2 - K_H^2) = \left(2m/\hbar^2\right)^2 V_H V_{-H}, \tag{13}$$

which to an excellent approximation for thermal neutrons translates to

$$\xi_O \xi_H = \frac{k_O^2 \chi_H \chi_{-H}}{4}. \tag{14}$$

where

$$K = k_O \sqrt{1 - \frac{2mV_O}{\hbar^2 k_O^2}}\ , \quad \xi_O = K_O - K \text{ and } \xi_H = K_H - K, \tag{15}$$

K being the magnitude of the average internal wave vector, differing from k_O due to the refractive index. Eq.(13) defines the dispersion surface in the reciprocal space. Each solution of Eq.(13) is represented by a point on the dispersion surface, with the corresponding wave amplitude ratio

$$\frac{\psi_H}{\psi_O} = \frac{(K^2 - K_O^2)}{(2m/\hbar^2)V_{-H}} = \frac{(2m/\hbar^2)V_H}{(K^2 - K_H^2)} \approx -\frac{2\xi_O}{k_O \chi_{-H}} = -\frac{k_O \chi_H}{2\xi_H} \tag{16}$$

The appearance of V_{-H} in the solution is to be expected since a multiple interplay between the two wave components involves the **-H** reflection as well. In practice, the solutions K_O and K_H of Eq.(13) differ from K at most by $10^{-5}k_O$. The loci of points where the allowed $\mathbf{K_O}$ and $\mathbf{K_H}$ vectors originate, then constitute a hyperbolic dispersion surface in the reciprocal space and each point on this surface is called a tie point. In Fig.3, the solutions in the vicinity of Bragg angle θ_B are shown

for a positive value of b_C i.e. for V_O and $V_H > 0$. Over this small region, the spheres LR and LL′ of radius k_O drawn about the origin O and reciprocal lattice point H respectively, appear as planes intersecting the bisector LQ of OH at the point L in the plane of incidence. The spheres QR′ and QQ′ of radius K, centred at O and H respectively, are the asymptotes to the hyperbolic dispersion surface comprising branches labelled α and β, α denoting the branch closer to the point L. The dispersion surface has a remarkable property viz. that for any allowed ψ, the energy flow averaged over the planar spacing d and represented by the current density vector

$$\left\langle \mathbf{J}_{\psi} \right\rangle = \frac{\hbar}{\mathrm{m}} \left(|\psi_0|^2 \mathbf{K_O} + |\psi_H|^2 \mathbf{K_H} \right) \tag{17}$$

is directed along the normal [132] to the dispersion surface at the corresponding tie point.

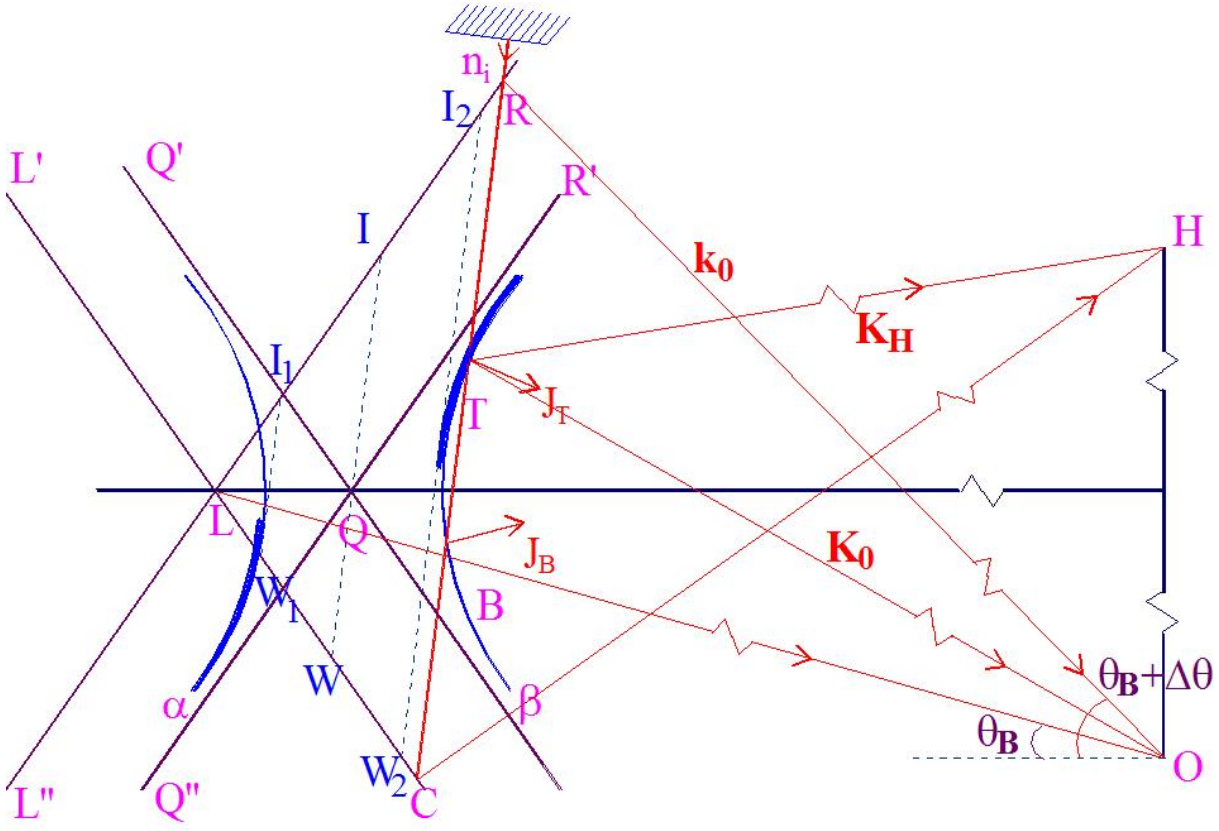

Fig.3 Reciprocal space representation of the Bragg diffraction in a single crystal.

The dispersion surface thus represents an infinity of allowed internal wave functions and each tie point characterises completely the properties of the associated wave and its propagation.

2.2.1 Boundary conditions and diffraction geometries

Of the various possible solutions obeying the dispersion relation, only those satisfying the following boundary conditions at the crystal-vacuum interface can be excited:

I) The tangential components of wave vectors for the incident as well as the diffracted wave should be continuous across the interface The vacuum wave vector of either wave can hence differ from the corresponding internal wave vector at most by a component along the surface normal.

II) At the interface, the incident and diffracted wave components of the external wave function should match the respective net components of the internal wave function, each internal component comprising a summation extending over all excited tie points.

The condition I) is represented geometrically in Fig.3 for incidence at $\theta_B+\Delta\theta$ represented by the point R on the sphere of incidence. Only for the tie points T and B in the figure where the straight line passing through R and parallel to the surface normal $\mathbf{n_i}$, intersects the dispersion surface, does $\mathbf{k_O}$ = **RO** differs from the associated internal wave vectors $\mathbf{K_O}$, viz. **TO** and **BO**, just by components, **RT** and **RB** respectively, along $\mathbf{n_i}$. Thus in general, two tie points can be excited at each angle of incidence.

Depending on the angle θ_S between the diffracting planes and the crystal surface, the diffraction is classified into two cases, viz. Bragg configuration for $-\theta_B<\theta_S<\theta_B$ (Fig4a) and Laue configuration for $\theta_B-\pi<\theta_S<-\theta_B$ (Fig4b). The ratio of direction cosines of the external incident and diffracted wave vectors, $\mathbf{k_O}$ and $\mathbf{k_H}$, with respect to the inward surface normal $\mathbf{n_i}$,

$$b = \frac{\mathbf{k_O}.\mathbf{n_i}}{\mathbf{k_H}.\mathbf{n_i}} = -\frac{\sin(\theta_B - \theta_S)}{\sin(\theta_B + \theta_S)}. \qquad (18)$$

is negative in the Bragg case and positive in the Laue case. The diffracted wave exits the incidence surface in the Bragg case, but propagates inside the crystal in the Laue case. In the reciprocal space (Fig.3), $\mathbf{n_i}$ lies between the directions QQ′ and QR′ in the Bragg, and between QQ′ and QQ′′ in the Laue case. For a given incidence angle in the Bragg case, two tie points, in general, are excited either on the α- or on the β-branch. In the Laue case on the other hand, one tie point each on the α and β branches is excited.

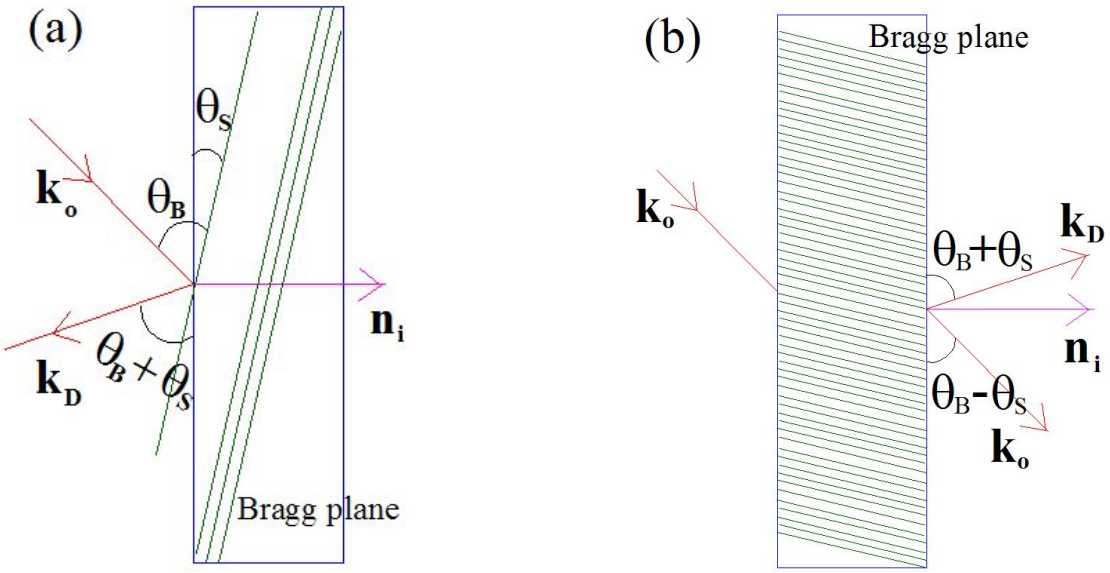

Fig.4 Asymmetric (a) Bragg and (b) Laue configurations of neutron incidence on a single crystal.

2.2.2 Bragg Case

In the Bragg configuration, incidence and exit surfaces are identical. Thus, for incidence represented by point R in Fig.3, the exit wave vector $\mathbf{k_H}$ is obtained, in accordance with the boundary condition I), by producing TB, to intersect the sphere of diffraction CLL′ of radius k_O about **H** at the point C, say. Then $\mathbf{k_H}$ = **CH.** The wave vector of the external diffracted wave thus

differs from $\mathbf{k_O}$ by a small component, such as CR, in addition to **H**. The boundary condition II) in this case reads (Fig.4a)

$$1 = \psi_{OT} + \psi_{OB} \qquad \text{and} \qquad \psi_H^V = \psi_{HT} + \psi_{HB}\,, \tag{19}$$

where $\psi_H^V e^{i\mathbf{k_H}\cdot\mathbf{r}}$ is the diffracted wave outside the crystal. Over a range of incidence angles indicated by I_1I_2 in Fig.3, the line drawn through the point of incidence parallel to $\mathbf{n_i}$ does not intersect the dispersion surface. Thus $\mathbf{K_O}$ and $\mathbf{K_H}$ are complex over the range I_1I_2 even for a non-absorbing crystal and the amplitude ratio is given by

$$\psi_H^V = \frac{\psi_H}{\psi_O} = -e^{i\phi}\sqrt{|b|\frac{\chi_H}{\chi_{-H}}}\,. \tag{20}$$

The phase ϕ varies smoothly from 0 at I_1 through $\pi/2$ at I, to π at I_2. For centrosymmetric crystals, $\chi_H = \chi_{-H}$, and the reflectivity equals unity, i.e.,

$$|b|^{-1}\left|\psi_H^V\right|^2 = 1 = I_D \tag{21}$$

over the segment I_1I_2. The factor $|b|^{-1}$ has been included in the definition of reflectivity to correct for the change, by the factor $|b|^{-1}$ in the diffracted beam cross section from that of the incident beam. Thus over the region I_1I_2 corresponding to an incidence angle width

$$w_i = \frac{2\sqrt{\chi_H\chi_{-H}}}{\sin 2\theta_B\sqrt{|b|}}\,, \tag{22}$$

the incident wave undergoes total reflection generating a diffracted wave with an emergent angular spread

$$w_e = \frac{2}{\sin 2\theta_B}\sqrt{\chi_H\chi_{-H}\,|b|} \tag{23}$$

represented by the segment W_1W_2. The symbol w_i signifies the full Darwin width. When thermal vibrations of lattice atoms are considered, the widths w_i and w_e get multiplied by the Debye-Waller

factor exp(-W). The centre, θ_C, of the total reflectivity range differs from θ_B by

$$\theta_C - \theta_B = \frac{LI}{k_0} = (1 - 1/b)\frac{\chi_0}{2\sin 2\theta_B}, \tag{24}$$

a deviation brought about by the average refractive index, $(1-\chi_O/2)$.

As mentioned, $\mathbf{K_O}$ and $\mathbf{K_H}$ have to be complex even for a nonabsorbing crystal, over the total reflectivity regime. Since the incident wave vector $\mathbf{k_O}$ in vacuum is real, the boundary condition I) dictates that the imaginary component $\mathbf{K_O}''$ of $\mathbf{K_O}$ must necessarily lie along the surface normal. Moreover $\mathbf{K_H}''= \mathbf{K_O}''$, since $\mathbf{K_H}$ and $\mathbf{K_O}$ differ by a real vector $\mathbf{H}$. Thus both the incident and the diffracted wave intensities must attenuate in a direction perpendicular to the crystal surface as exp $(-2K_O''Z)$, Z being the depth in the crystal, with

$$K_0'' = \frac{\pi \sin\phi}{\lambda}\frac{\chi_H}{\sqrt{|\sin(\theta_B - \theta_S)\sin(\theta_B + \theta_S)|}}. \tag{25}$$

The attenuation (and not absorption) is a direct consequence of the diversion of the incident wave intensity into the diffracted wave at the expense of penetration into the crystal. This phenomenon is known as primary extinction, to distinguish it from the secondary extinction caused by overlying grains in polycrystalline samples. The primary extinction is the strongest for $\phi=\pi/2$, i.e. at θ_C. The effect is the most pronounced for the two extreme Bragg configurations and weakest for the symmetric Bragg case.

For neutron incidence outside the total reflectivity domain, i.e., $|y| > 1$, the fraction of incident intensity diffracted at the front face of a thick single crystal is given by

$$I_D = (|y| - \sqrt{y^2 - 1})^2 = \left(1 - \sqrt{1 - y^{-2}}\right) / \left(1 + \sqrt{1 - y^{-2}}\right). \tag{26}$$

Here, y denotes scaled deviation of incidence angle θ from centre of Bragg diffraction θ_C i.e.,

$$y = 2(\theta - \theta_C)/w_i. \tag{27}$$

However, for a thin crystal, the reflectivity remains unity over $|y| \leq 1$, whereas for $|y| > 1$, we obtain the Ewald reflectivity

$$I_D = (1 - \sqrt{1 - y^{-2}}) . \quad (28)$$

2.2.2.1 Neutron collimation

Experimenters yearn for monochromatic neutron beams with δ-function angular profiles. Such beams allow measurements of ultra-small beam deflections and determination of micrometre-sized agglomerate distributions within samples through their USANS (ultra-small angle neutron scattering) studies. Early attempts at collimation used a pair of ~ mm wide slits set at a distance ~ m apart to limit the angular divergence of the beam. An advanced collimator introduced by Soller [133] consists of a number of uniformly spaced thin cadmium-coated metal sheets (steel or copper) forming a series of long (~ m) and narrow (~ mm) rectangular channels between the sheets. Each channel allows a narrow parallel beam of neutrons to pass through since highly divergent neutrons get absorbed in the cadmium coating [134-135]. Soller slits afforded large beam cross-sections without sacrificing the angular collimation. The slit collimation for thermal and cold neutrons however is constrained to the minute of arc regime; efforts at better collimation are defeated by neutron diffraction at the slit edges apart from a heavy loss in the beam intensity. Tighter collimation ~ arcsec is achievable through neutron diffraction from a single crystal.

In the symmetric Bragg case (θ_S=0 and b=–1), the diffracted wave exits at exactly the same angle to the planes as the incident wave and both w_i and w_e equal $w = 2\chi_H / \sin 2\theta_B$ for a centrosymmetric crystal. For 2Å neutrons exciting a {220} reflection in silicon, w = 1.2 arcsec. Neutron double-crystal diffractometers employ single Bragg reflections ~ arcsec, both as a monochromator and analyser albeit with long tails. However, the tails were suppressed by

exploiting multiple successive identical Bragg reflections from two slabs of a channel-cut monolithic single crystal, producing a highly collimated neutron beam [111,115].

For a crystal cut asymmetrically at $\theta_S \approx \theta_B$ to the reflecting planes, $|b|^{-1}$ is large. For incidence at a near grazing angle $\theta_B - \theta_S$, the crystal will thus accept a narrow beam of a large angular divergence $w/|b|^{1/2}$ and generate a highly collimated ($w|b|^{1/2}$) diffracted beam wider in cross section. The enhancement by the factor |b| in the spatial width δx of the reflected beam vis-a-vis the incident beam, reduces the angular divergence of the reflected beam by the same factor. This is a direct consequence of conservation of the phase space volume spanned by the beam since the momentum spread $\delta p_x = p_0 \delta\theta$ of a monochromatic beam is proportional to the angular width $\delta\theta$. Such an arrangement therefore works as a collimator. The same setup with the beam directions reversed, relating to the other extreme ($\theta_S \approx -\theta_B$, $|b|^{-1} \rightarrow 0$) in the Bragg case, may be employed where a small sample is to be studied and the angular divergence is of no great consequence.

2.2.3 Laue Case

In a Laue configuration (Fig.4b), the line drawn through the point of incidence parallel to $\mathbf{n_i}$ always intersects the dispersion surface in two real points, such as A and B in Fig.5. The internal wave vectors are thus always real for a nonabsorbing crystal. Further, since the diffracted wave does not exit the incidence surface, the boundary condition II) implies

$$1 = \psi_{O\alpha} + \psi_{O\beta} \qquad\qquad 0 = \psi_{H\alpha} + \psi_{H\beta} \,. \tag{29}$$

At the exit surface, each composite internal wave function (ψ_α or ψ_β) gives rise to a transmitted and a diffracted wave. The situation where the exit surface normal, $\mathbf{n_e}$ is not parallel to $\mathbf{n_i}$ is illustrated in Fig.5. The line drawn through A parallel to $\mathbf{n_e}$ intersects the spheres of incident and diffracted wave vectors in vacuum in the points E and R respectively. Thus, the exiting transmitted

and diffracted waves generated by ψ_α will propagate in the directions **EO** and **RH** respectively. Since in general, the points E and T are distinct, the transmitted wave vector **EO** subtends an angle, ET/k_O, with the incident wave vector **TO**. The tie point B will similarly result in another set of exiting waves.

In the case where the incidence and exit surfaces are parallel, each of the tie points A and B, excites points T and I on the $\mathbf{k_O}$ and $\mathbf{k_H}$ spheres respectively. Each transmitted wave thus propagates exactly in the incident direction **TO** and each diffracted wave, along **IH**. In particular, for the symmetric Laue configuration, where $\mathbf{n_i}$ is parallel to LQ ($\theta_S = -\pi/2$, b=l), a wave incident at an angle ($\theta_B+\omega$) to the crystal planes gives rise to diffracted waves exiting at ($\theta_B-\omega$) thus always maintaining an angle $2\theta_B$ between the incident and diffracted waves. The amplitudes of the exiting waves are derived by applying the boundary condition II) at the exit surface.

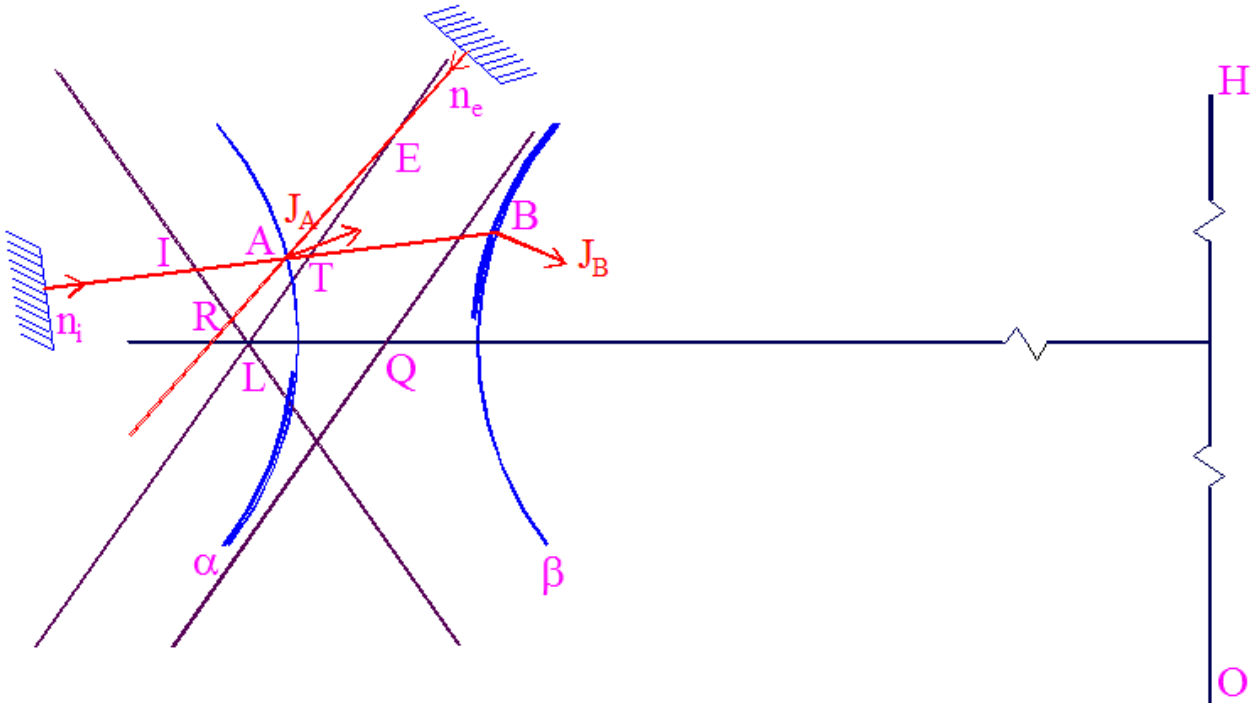

Fig.5 Reciprocal space diagram of the Laue diffraction in a single crystal.

We shall confine our discussion henceforth to nonabsorbing centrosymmetric crystals, for the sake of simplicity and clarity. The assumption of zero absorption is fairly accurate for instance, with crystals of silicon which exhibit absorption lengths of a few metres for Å wavelength neutrons. The quantities χ_O, $\chi_H(=\chi_{-H})$, $\mathbf{K}$, $\mathbf{K_O}$ and $\mathbf{K_H}$ are thus all real.

The internal wave solutions can then be represented by

$$\psi_{O\alpha} = 1 - \psi_{O\beta} = \frac{1}{2}\left(1 - \frac{y}{\sqrt{y^2+1}}\right)$$
$$\text{and } \psi_{H\alpha} = -\psi_{H\beta} = -\frac{1}{2}\left(\frac{\sqrt{|b|}}{\sqrt{y^2+1}}\right), \tag{30}$$

with the associated wave vector magnitudes

$$K_{\substack{O\alpha \\ \beta}} = K \pm \frac{k_0\chi_H\sqrt{|b|}}{2}\left(\sqrt{y^2+1} \pm y\right)$$
$$K_{\substack{H\alpha \\ \beta}} = K \pm \frac{k_0\chi_H}{2\sqrt{|b|}}\left(\sqrt{y^2+1} \mp y\right). \tag{31}$$

For incidence at $\theta = \theta_C$, i.e. $y = 0$, the incident wave splits equally into the α and β waves. $\psi_{O\beta}$ gets stronger at the expense of $\psi_{O\alpha}$, as θ increases beyond θ_C ($y > 0$), whereas $\psi_{O\alpha}$ becomes the dominant component on the other side of θ_C. The diffracted wave amplitudes on the other hand exhibit a peak, $\sqrt{|b|}/2$ in magnitude, at θ_C and fall symmetrically on both sides of θ_C. The diffracted intensities $\psi^2_{H\alpha}$ and $\psi^2_{H\beta}$ drop to half their peak values at $y = \pm 1$, corresponding to an FWHM equal to w_i of Eq.(22). Thus θ_C represents the centre of diffraction in the Laue case as well. Only in the symmetric Laue configuration, does θ_C equal θ_B represented by the point L, the centre of diffraction within the kinematical model.

2.2.3.1 Energy flow and Pendellösung oscillation

Associated with the two tie points such as A and B, excited for a given incidence angle are the current density vectors

$$\langle \mathbf{J}_{\alpha} \rangle = \frac{\hbar}{m}\left(\psi_{O\alpha}^2 \mathbf{K}_{O\alpha} + \psi_{H\alpha}^2 \mathbf{K}_{H\alpha}\right) \text{ and } \langle \mathbf{J}_{\beta} \rangle = \frac{\hbar}{m}\left(\psi_{O\beta}^2 \mathbf{K}_{O\beta} + \psi_{H\beta}^2 \mathbf{K}_{H\beta}\right) \tag{32}$$

directed along the respective normals to the dispersion surface. A small variation in θ causes a large deflection of the energy flow vectors, the angle amplification occurring, albeit nonlinearly, typically by five orders of magnitude. An incident neutron beam with an angular divergence of a few arcsec thus illuminates the entire 'Borrmann fan' of energy flow with a $2\theta_B$ angular span centred on the reflecting planes. For large magnitudes of y, the diffracted wave intensities drop to insignificant levels and the currents propagate practically in the incident direction. In the symmetric Laue case, the two <**J**> vectors for a given incidence angles subtend equal and opposite angles with the lattice planes and only for y=0, do they propagate in the same direction, i.e. along the lattice planes. Kikuta et al. [75] and Zeilinger and Shull [136] utilised the large angle magnification within a crystal near y = 0, to measure a minute deflection of a neutron beam using a monolithic Si double crystal arrangement in symmetric Laue configuration. If the incident plane wave is of infinite (or very large) lateral extent, the α and β waves overlap physically during their propagation through the crystal and create an interference term

$$\begin{aligned}\langle \mathbf{J}_{\alpha\beta} \rangle &= \frac{\hbar}{m}\left(\psi_{O\alpha}\psi_{O\beta}\,\mathbf{K}_{O\alpha} + \mathbf{K}_{O\beta}) + \psi_{H\alpha}\psi_{H\beta}\,\mathbf{K}_{H\alpha} + \mathbf{K}_{H\beta})\right)\cos\left(\mathbf{K}_{O\alpha} - \mathbf{K}_{O\beta}).\mathbf{r}\right) \\ &= \frac{\hbar(1-\chi_O/2)}{2m(1+y^2)}(\mathbf{k}_O - b\mathbf{k}_H)\cos\left(\frac{2\pi z\sqrt{1+y^2}}{\Delta}\right),\end{aligned} \tag{33}$$

In addition to sum

$$\langle \mathbf{J}_{\alpha} \rangle + \langle \mathbf{J}_{\beta} \rangle = \frac{\hbar(1-\chi_O/2)}{2m(1+y^2)}\left(\left(1+2y^2\right)\left(\mathbf{k}_O + b\mathbf{k}_H\right)\right). \tag{34}$$

The depth Z is measured from the incidence surface along $\mathbf{n_i}$ and

$$\Delta = \frac{2\pi}{k_O \chi_H} \sqrt{\left|\sin\left(\theta_B + \theta_S\right)\right| \sin\left(\theta_B - \theta_S\right)}, \tag{35}$$

is called the extinction distance. In the symmetric Laue case, $\Delta_S = 2\pi \cos\theta_B / k_O \chi_H$ and is e.g., 64 μm for the {220} Si reflection with 2Å neutrons.

In the general Laue case, the component of $<\mathbf{J}_{\alpha\beta}>$ along $\mathbf{n_i}$ vanishes as can be seen by taking a dot product of $<\mathbf{J}_{\alpha\beta}>$ in Eq. (33) with $\mathbf{n_i}$. Thus $<\mathbf{J}_{\alpha\beta}>$ is normal to $\mathbf{n_i}$, lies in the plane of incidence and varies sinusoidally in magnitude with Z. At depths which are integral multiples of $\Delta / \sqrt{1+y^2}$, the net current vector

$$\left\langle \mathbf{J} \right\rangle_m = \frac{\hbar \mathbf{k_O} (1 - \chi_O / 2)}{m} \tag{36}$$

is identical to that for the incident wave modified by the average refractive index. At depths $z = (m + 1/2)\Delta / \sqrt{1+y^2}$ on the other hand,

$$\left\langle \mathbf{J} \right\rangle_{m+1/2} = \frac{\hbar (1 - \chi_O / 2)}{m(1+y^2)} \left(y^2 \mathbf{k_O} + b \mathbf{k_H} \right), \tag{37}$$

which is predominantly in the diffracted wave direction for fractional values of y. At the centre of diffraction (y = 0), $\left\langle \mathbf{J} \right\rangle_{m+1/2} = b\hbar \mathbf{k_H} (1 - \chi_O / 2) / m$, propagates totally along the diffracted direction, the factor b in the numerator compensating the changed cross section of the diffracted beam. This periodic variation with depth of the energy flow direction (Eqs.(33-34)) is termed ‘Pendellösung’, due to its analogy with the energy transfer between two weakly coupled pendulums.

2.2.3.2 Symmetric Laue case

For an infinite incident plane wave, the α and β wave functions combine at the exit surface in accordance with the boundary conditions to generate a forward transmitted and a diffracted wave in vacuum. In order to simplify the relevant expressions without losing generality, we restrict ourselves to the symmetric Laue case in a parallel-faced crystal slab and a full reflection ($\chi_O = \chi_H$). The amplitudes of the emergent waves can then be written as

$$T(y,t) = \psi_O^V(y,t) = e^{\frac{i\pi t(1-y)}{\Delta_S}}\left(\cos\left(\frac{\pi t}{\Delta_S}\sqrt{y^2+1}\right) + i\frac{y}{\sqrt{y^2+1}}\sin\left(\frac{\pi t}{\Delta_S}\sqrt{y^2+1}\right)\right) \tag{38a}$$

$$\text{and } R(y,t) = \psi_H^V(y,t) = ie^{\frac{i\pi(t(1+y)+2Z_f y)}{\Delta_S}}\left(\frac{\sin\left(\frac{\pi t}{\Delta_S}\sqrt{y^2+1}\right)}{\sqrt{y^2+1}}\right), \tag{38b}$$

t denoting the slab thickness and Z_f being the distance of the incidence surface from the origin measured along $\mathbf{n_i}$. As explained in Fig.5, the ψ_O, wave emanates exactly along the incidence direction, represented by y, whereas the ψ_H wave exits at an angle corresponding to -y with the exact Bragg condition. The associated intensities

$$I_O(y,t) = 1 - I_H(y,t), \tag{39a}$$

$$\text{with } I_H(y,t) = \frac{\sin^2\left(\frac{\pi t}{\Delta_S}\sqrt{y^2+1}\right)}{\left|y^2+1\right|}; \tag{39b}$$

are both symmetric about the centre of diffraction viz. y=0. The diffracted intensity exhibits maxima equal to $\left(y_m^2+1+\Delta_S^2/(\pi^2t^2)\right)^{-1}$ at angles $y=y_m$ satisfying the condition, $\tan\left(\pi t\sqrt{y_m^2+1}/\Delta_S\right) = \pi t\sqrt{y_m^2+1}/\Delta_S$. The H and O intensities have been plotted in Fig.6 for $t=20.25\Delta_S$. Both the intensities oscillate strongly, the oscillations becoming more rapid in the

wings (large-y regions). The frequency of oscillations also rises with t/Δ_S, in accordance with Eqs.(39a-39b). Similar intensity oscillations occur in a Bragg configuration outside the total reflectivity range [4]. For thick non-absorbing crystals, $\pi t/\Delta_S$ is large so the $\sin^2$ oscillations tend to average to a value equal to .5. Thus Eq. (39b) reduces to a simple Lorentzian shape, $I_H(y) = 0.5/\left(\left|y^2+1\right|\right)$ [4].

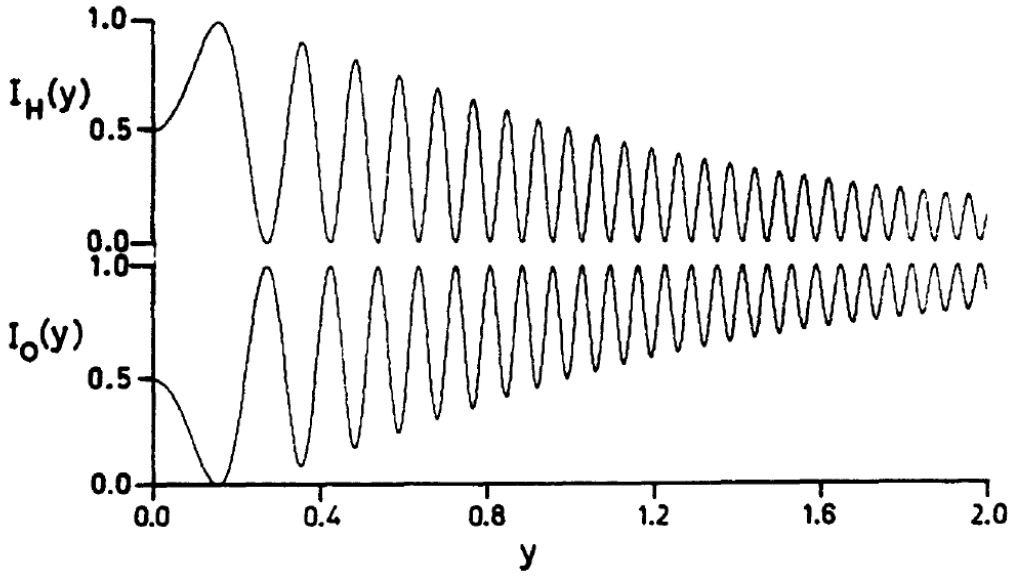

Fig.6 The intensities of the forward (I_O) and diffracted (I_H) beams exiting a parallel face crystal slab in the symmetric Laue configuration as a function of the reduced incidence angle y for the slab thickness $t = 20.25\ \Delta_S$ [4].

2.4 Symmetric LLL neutron interferometer operation

A neutron wave can be split with a single crystal into two spatially separated O and H waves bearing a definite phase relationship with each other (Eqs.(38a-38b). The coherently split waves can be recombined after travelling a certain distance using a 'mirror' crystal, to produce interference fringes with a period d. Since no detectors with spatial resolutions ~ Å for neutrons are

currently available, the interference pattern is analysed with an ‘analyser’ crystal by monitoring the intensity of waves emanating from it. The numerous configurations like BB, LL, BBB, LBBL and LLL, have been tested and operated since last 37 years [1,4,86-88,121-130]. Here the letters L and B stand for Laue and Bragg cases respectively. Though each configuration has its own merits and demerits, the LLL symmetric IFM, due primarily to its versatility and size, has been employed in our experiment (Chapter 5). Large neutron IFM inevitably permits larger path separations between the coherent wave amplitudes allowing high precision studies of materials properties e.g., neutron coherent scattering length determination.

In the configuration represented in Fig.7, the contributions of waves in the paths I and II to the O and H waves emanating from the analyser slab can, by a repetitive application of Eqs.(38a-38b), be

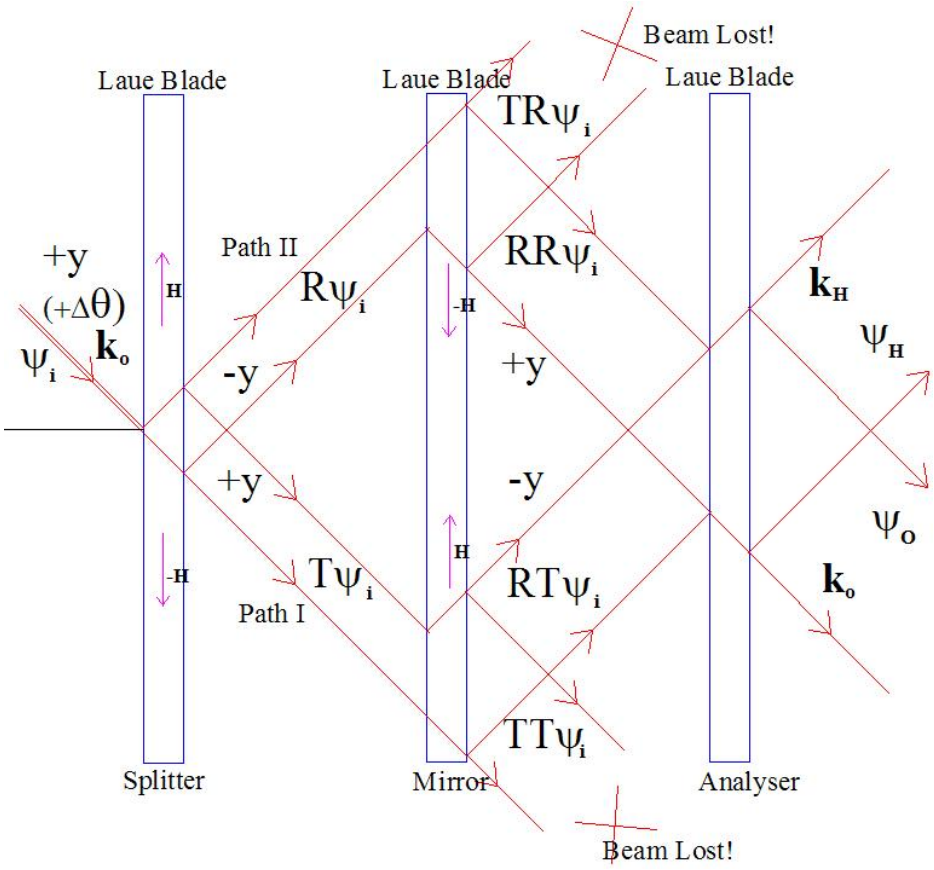

Fig.7 Operating principle of a symmetric LLL IFM.

expressed as

$$\psi_O^I = T(y,t_S)R(y,t_M)R(-y,t_A) \quad (40a)$$

$$\psi_O^{II} = R(y,t_S)R(-y,t_M)T(y,t_A) \quad (40b)$$

$$\psi_H^I = T(y,t_S)R(y,t_M)R(-y,t_A) \quad (40c)$$

and $$\psi_H^{II} = R(y,t_S)R(-y,t_M)R(y,t_A) \quad (40d)$$

Here, symbols t_S, t_A and t_M denote the thicknesses of the splitter, mirror and analyser blades respectively. The magnitudes of ψ_O^I and ψ_O^{II} both involves two Bragg reflection and one transmission hence can be made identical for all y by choosing thicknesses $t_S = t_A = t_M = t$. Further, phase difference between ψ_O^I and ψ_O^{II} is zero because separation between splitter and mirror, and mirror and analyser is identical making the traversal path for both wave amplitudes exactly same. So the two O-wave components, equal in magnitude, interfere constructively for all incidence angles. It is impossible to make the magnitudes of ψ_H^I and ψ_H^{II} equal regardless of y, since the former involves three reflections and the latter, one reflection and two transmissions. Now, if a phase difference χ is externally introduced between paths I and II using a phase shifter, the O and H beam intensities vary as

$$I_O^{LLL}(\chi,y) = \left|\psi_O\right|^2 = \left|T\right|^2\left|R\right|^4(1+\cos\chi) = I_I(y)(1+\cos\chi) \quad (41a)$$

and $$I_H^{LLL}(\chi,y) = \left|\psi_H\right|^2 = \left|R\right|^2\left[\left(\left|T\right|^4+\left|R\right|^4\right)-\left|R\right|^2\left|T\right|^2\cos\chi\right] = I_{II}(y) - I_I(y)\cos\chi\,. \quad (41b)$$

The terms I_I and I_{II} denote the intensity sums of I and II components in the O and H beams respectively. The O and H intensities thus oscillate out of phase, conserving their sum.

For $\chi = \pi$, the O-beam gets completely extinguished and H-intensity reaches its maximum. Contrast of the interference oscillation is defined as,

$$C = \frac{I_{max} - I_{min}}{I_{max} + I_{min}}. \tag{42}$$

The beam contrast equals unity for the O-beam, in ideal case. The contrast values calculated for the H beam with the illumination of the entire Bormann fan, lie below about 0.5. Further, Due to the extremely low phase space density of neutron beams (10^{-14}), one observes pure single particle self-interferences. Using Eq.(39b), the two intensities (Eqs.(41a-41b)) can be written as

$$\begin{aligned} I_O^{ttt} &= 4I_H^2(y,t)\left(1 - I_H(y,t)\right) \\ I_H^{ttt} &= I_H(y,t)\left(1 - 2I_H(y,t)\right)^2 \end{aligned} \tag{43}$$

for $\chi = 0$ and

$$\begin{aligned} I_O^{ttt} &= 0 \\ I_H^{ttt} &= I_H(y,t) \end{aligned} \tag{44}$$

for $\chi = \pi$. For $\chi = \pi$, the sum of the O and H intensities appears in the H-beam and corresponds to the total intensity diffracted by the mirror, since the two forward diffracted beams from the mirror are lost to the interferometer (Fig.7). At $\chi = 0$, the two intensities exhibit extrema in addition to those caused by the extrema in $I_H(y,t)$, discussed earlier. Thus in the region $y^2<0.5$, the O-intensity maxima of 16/27 appear at angles where $I_H(y,t) = 2/3$, whereas smaller maxima of 2/27 occur in the H-intensity over the domain $y^2<5$, wherever $I_H(y,t) = 1/6$. For $y^2 \leq 1$, additional zeros of I_H^{ttt} are located where $I_H(y,t) = 1/2$. Fig.8 shows the O and H intensity variations for $t/\Delta_S = 20.25$ with $\chi = 0$ (solid curves) and $\chi = \pi$ (dashed curves). The O-beam gets completely extinguished at $\chi = \pi$, yielding an ideal contrast equal to unity. From the areas enclosed under the two I_H^{ttt} curves between $y = 0$ and 10, the H-contrast in this case is computed to be 0.44 (which is always less than unity) [1,4]. We have so far dealt with the diffraction of neutrons by treating them as infinite plane waves. In practice, a narrow neutron beam of large angular divergence is often employed in interferometric

studies. With such beams, the α and β components of energy flow separate physically for large angles |y|, of incidence and each component independently gives rise to O and H beams at the exit face. Under these circumstances, Eqs.(38a-38b) ceases to be applicable. Further, after traversing a crystal slab of thickness t, the O and H beams become wider by $2t\sin\theta_B$ (cf.Fig.7). The effects of a finite curvature of the incident wavefront can be accounted for by using the spherical [78-79] wave approach.

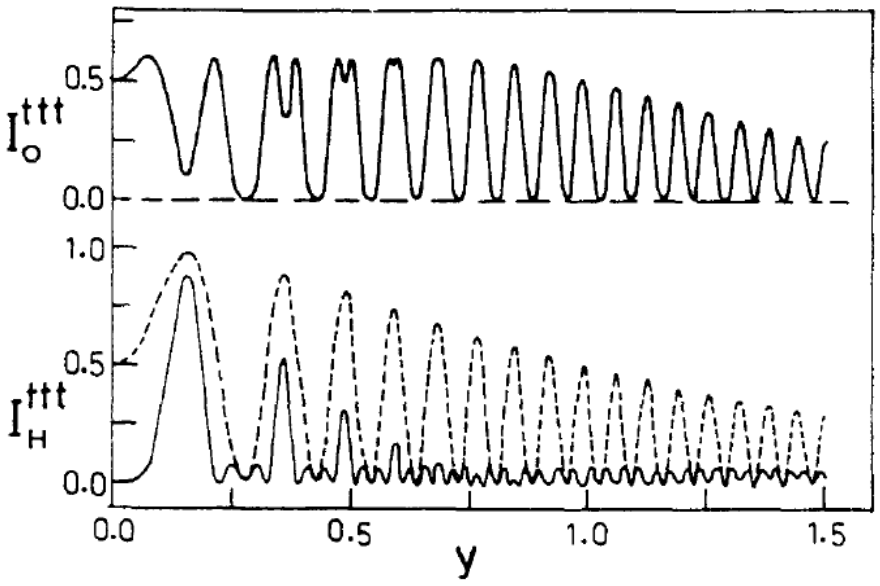

Fig.8 Intensities of the forward (O) and diffracted (H) beams emerging from a symmetric LLL interferometer ($t_S=t_M=t_A=t=20.25\Delta_S$) as a function of the reduced incidence angle y for $\chi = 0$ (solid curves) and $\chi = \pi$ (dashed curves) [4].

2.5 Detectors

In experiments described in Chapters 3, 4 and 5, neutron intensity pattern has been recorded by converting neutrons into charged particles via nuclear reactions [137]. These charged particles in turn, are detected using the conventional methods. We have mainly used gas filled counter operated in the proportional region to discriminate against γ's. For thermal neutrons, Gas filled in the cylinder is comprised of helium gas enriched with He^3, or BF_3 gas enriched with B^{10} and following nuclear reactions take place

1. $He^3 + n = T + p + 0.765$ MeV
2. $B^{10} + n = Li^7 + He^4 + 2.79$ MeV (Yield: 6%)

   $B^{10} + n = Li^{7\#} + He^4 + 2.31$ MeV (Yield: 94%)

   $\rightarrow Li^{7\#} = Li^7 + 0.480$ MeV.

CHAPTER 3

Neutron forward diffraction by Bragg prisms

For a single crystal prism operating in a Bragg configuration, dynamical diffraction effects bring about strong deviations from the amorphous prism scenario. For a single crystal prism, if neutron incidence is set close to a Bragg reflection i.e., $\theta \sim \theta_B - \theta_S$ just outside the total reflection domain, unreflected neutrons traverse the prism at an angle Δ to the incidence surface and exit the side face

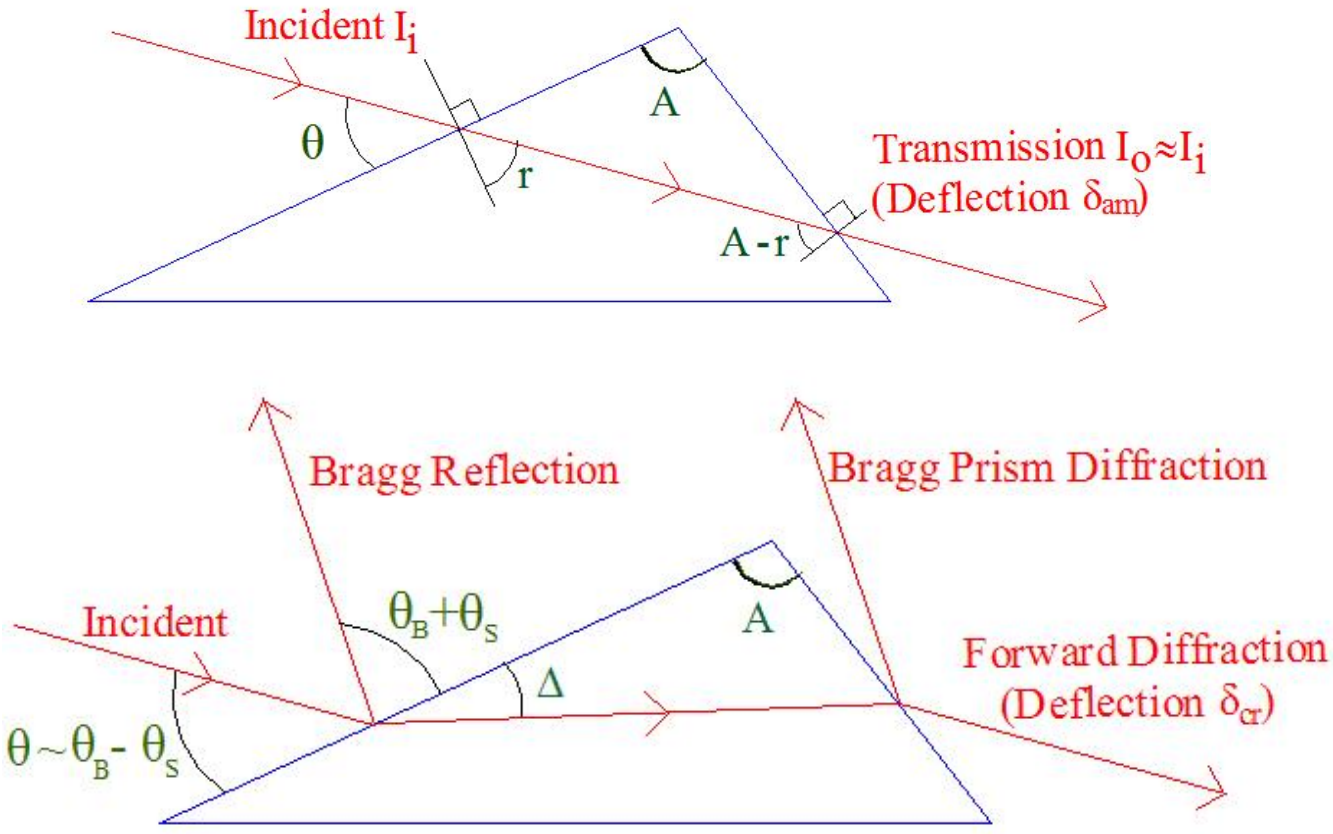

Fig.9 Neutron propagation through amorphous and single crystal prisms. For the single crystal prism, additional beams emerge from front and side faces and the transmitted beam undergoes a significant lateral displacement.

in forward diffracted (I_O) and diffracted (I_H) beams (Fig.9) [66,138]. Here, θ_B and θ_S imply their usual meaning of Bragg angle and the angle between the front surface and the diffracting planes respectively. We have coined the term 'Bragg prism for this device [139-142].

3.0 Amorphous prism

Consider incidence of a monochromatic neutron plane wave $e^{i\mathbf{k_O}.\mathbf{r}}$, on a non-absorbing amorphous prism at an angle θ (Fig.9 (top)). Because of the refractive index n of amorphous prism being very close to unity, these neutrons get almost fully transmitted through the prism (viz., $I_O \approx I_i$) and suffer a small deflection, with reflection at the incidence face being negligibly small. As alluded to earlier in Chapter 2, reciprocal space representation for an amorphous prism is depicted in Fig.10. Here, incident wave vectors $\mathbf{k_O}$ in vacuum can originate on sphere of incidence LR of radius k_O centred at reciprocal lattice point O and terminate at O of reciprocal lattice vector **OH**. For an amorphous prism, the refracted wave vectors ($|\mathbf{K}|=n|\mathbf{k_O}|$) must originate on sphere of refraction QR' of radius nk_O centred at reciprocal lattice point O and end at O. Let the vacuum wave vector $\mathbf{k_O}$ is represented by **RO** for an incidence angle equal to θ. The inside wave vector of prism is uniquely selected by continuity of the tangential component of the wave vector across the vacuum-prism interface and hence the allowed internal wave vector is **T'O** at incidence surface, since it differs from **RO** only by a vector **RT'** along the incidence surface normal $\mathbf{n_i}$ (Fig.10). By the triangle law of vectors, **T'O** and **RO** thus have identical components tangential to the incidence surface as required by the boundary conditions. We obtained the effected wave vector change –**RM** at incidence surface by extending back the inside wave vector **T'O** upto incidence sphere and located intersection point M. Negative sign indicates |n| less than unity. Thus, neutron gets deflected by $\delta_1=(n-1)\cot\theta$, away from the inward surface normal at incidence surface of the prism, with $(1-n)k_O$

being the separation of points M and T'.

Likewise, at the exit surface, which subtends an angle A with the front face, the same constraint can be effected by drawing a vector **T'S'** parallel to the exit surface normal $\mathbf{n_e}$ to intersect the sphere of incidence in S'. The emergent wave vector is hence **S'O**. Thus, –**MS'** is the effected change in wave vectors and $\delta_2=(1-n)\cot(A+\theta)$, the neutrons deflection at the exit surface. The **S'O** therefore, differs from $\mathbf{k_O}$ by –**RS'**. Thus, the net deflection viz., $\delta_{am} = -RS'/k_O$ produced by the amorphous prism is given by

$$\delta_{am} = (n-1)\{\cot\theta - \cot(A+\theta)\}\,. \tag{45}$$

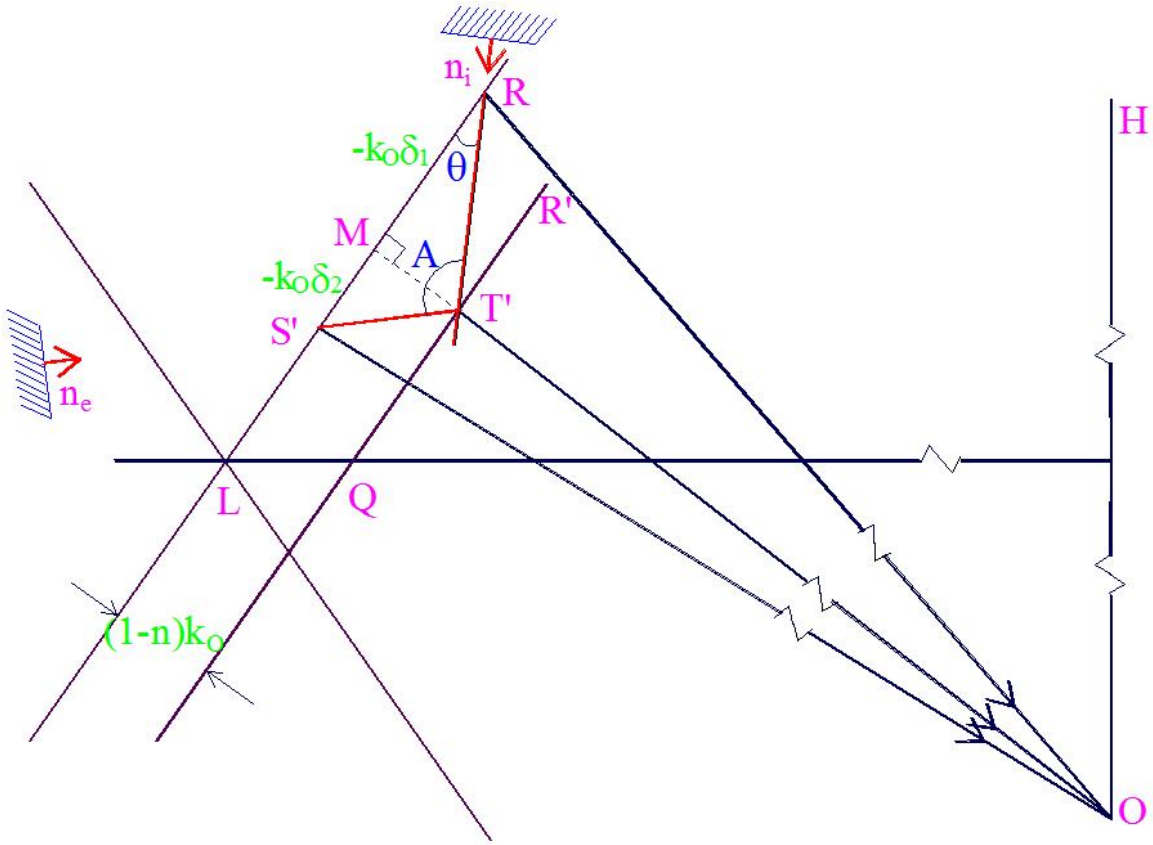

Fig.10 Boundary conditions on wave vectors dictate the allowed wave vectors at incidence and exit faces of an amorphous prism in reciprocal space.

We have derived the deflection formula (Eq.(45)) using only the boundary conditions on wave vectors and geometry of prism in reciprocal space. Since |n–1|<<1 for neutrons, the refraction angle r=π/2-θ and Eq. (45) can also be derived using Snell's law at the entrance and exit interfaces of the prism, as [109]

$$\delta_{am} = (n-1)\{\tan r + \tan(A-r)\}. \quad (46)$$

The deflection δ_{am} (Eqs.(45 or 46)) lies in the arcsec regime and Eqs.(45-46) show that at a given angle of incidence, neutron deflection depends on A and only a rotation through a few degrees of the amorphous prism varies δ_{am} by only ~ arcsec (Fig.11).

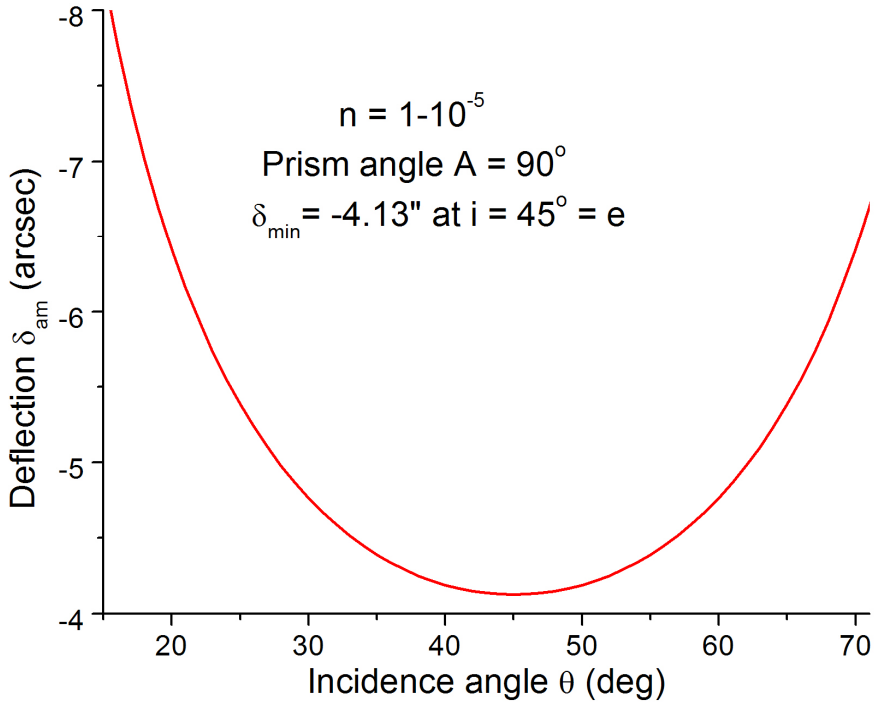

Fig.11 Calculated variation of δ_{am} with incidence angle for A=90° and n=1-10^{-5}, exhibits a minimum when both the incidence and exit angles equal.

3.1 Neutron forward diffraction

Consider a general asymmetric Bragg configuration wherein a monochromatic neutron plane wave $e^{i\mathbf{k}_O\cdot\mathbf{r}}$ with vacuum wave vector $\mathbf{k_O}$ is incident on the front surface of a thick non-absorbing single crystal at an angle θ_B-θ_S and gets diffracted at the angle θ_B+θ_S (Fig.12). The corresponding reciprocal space representation for the asymmetric Bragg configuration is depicted in Fig.13. Incidence at the Bragg angle θ_B is represented by the wave vector **LO**. Hence, the wave vector **RO** implies an incidence angle equal to θ_B+LR/k_O. For a Bragg prism, however, the allowed internal wave vector must originate on the hyperbolic dispersion surface. The continuity of the tangential components of the wave vectors at the vacuum-single crystal interfaces dictates that any change in wave vector takes place along inward normal $\mathbf{n_i}$ to the crystal surface. Therefore, for each angle of neutron incidence outside the total reflectivity domain, two tie points T and B in general, are

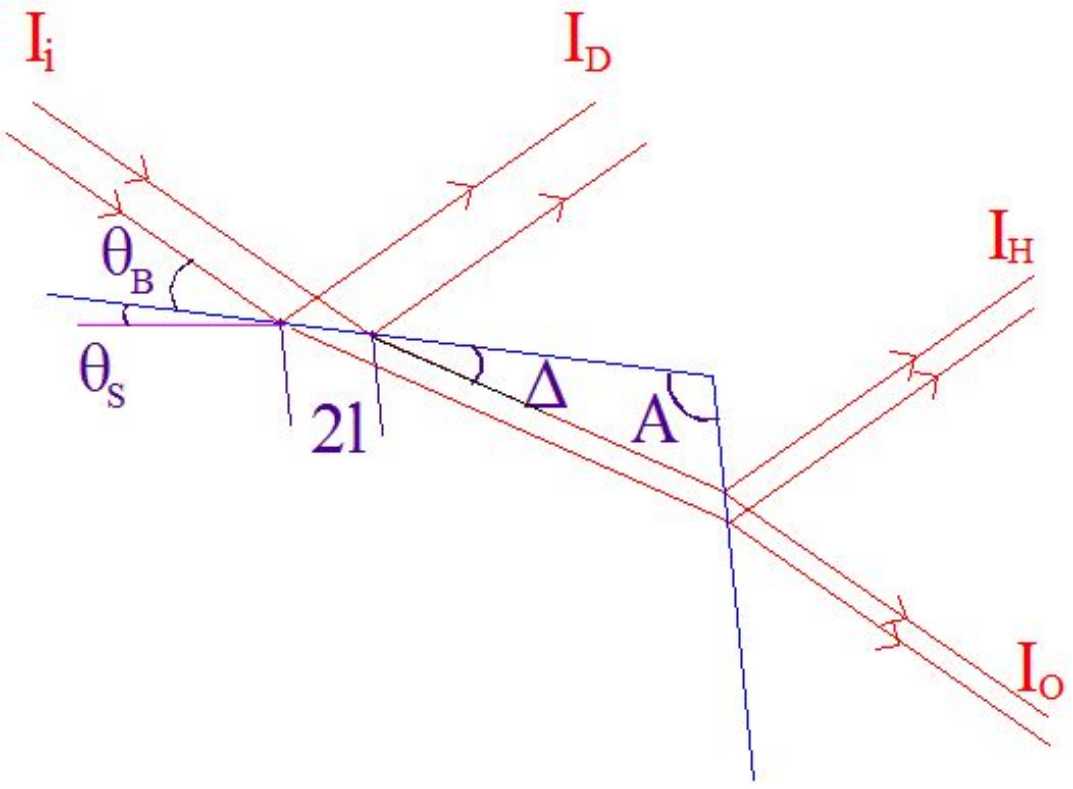

Fig.12 Bragg diffraction of a neutron beam from a thick single crystal in real space.

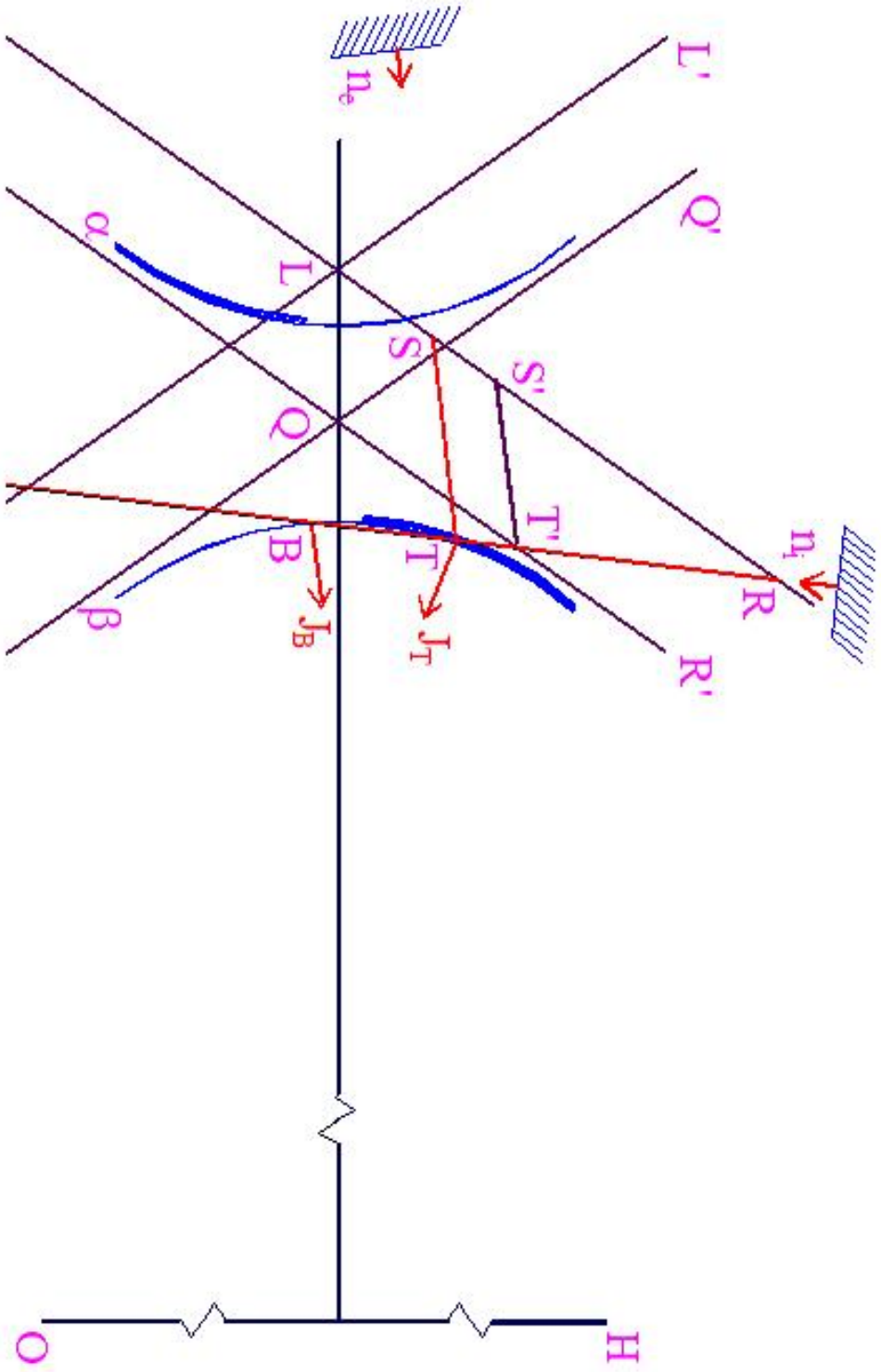

Fig.13 Bragg diffraction of a neutron beam in reciprocal space. At each incidence angle, continuity of tangential components of wave vectors across the incidence and exit faces of the prism yields unique tie points as well as internal and emergent wave vectors (see text).

excited by the incident wave (Fig.13). These tie points are obtained through the intersection of the dispersion surface with straight line drawn parallel to the $\mathbf{n_i}$. For each excited tie point on the dispersion surface, the associated energy flow vector is along local normal with $<\mathbf{J_T}>$ being directed into the crystal and $<\mathbf{J_B}>$ outward. The outward energy flow for tie point B, makes it physically unacceptable for thick single crystal [110], allowing the selection of only one tie point, T. Therefore, only the portion of the dispersion surface shown by thick lines in Fig.l3 can be excited viz., either low angle side of the α branch or higher angle side of the β branch due to energy flow considerations $<\mathbf{J}>$, inside the thick single crystal. Hence, the allowed internal wave vectors are $\mathbf{K_O}$=**TO** and $\mathbf{K_H}$=**TH** in forward diffracted and Bragg diffracted directions respectively. Inside single crystal, these two waves are coherently coupled viz., $\psi = \psi_O e^{i\mathbf{K_O}.\mathbf{r}} + \psi_H e^{i\mathbf{K_H}.\mathbf{r}}$ and propagate together like a single entity and get separated only at the exit surface [1,4,37].

3.2 Forward diffracted intensity fraction

For neutron incidence outside the total reflectivity domain $|y| > 1$ (e.g., $\theta_B+\Delta\theta$, say), the fraction of incident intensity diffracted at the front face is given by (viz., Eq.(26)),

$$I_D(\theta) = \frac{\sin(\theta_B + \theta_S)}{\sin(\theta_B - \theta_S)}\left|\frac{\psi_H}{\psi_O}\right|^2 = |b|^{-1}\left|\frac{\psi_H}{\psi_O}\right|^2 = (|y| - \sqrt{y^2-1})^2 . \quad (47)$$

Here, factor $|b|^{-1}$ has been included to account for the change in cross section of the diffracted beam vis-à-vis incident beam.

The remaining unreflected fraction $(1-I_D)$ of incident neutrons traverses the crystal, along the current density vector $\mathbf{J_T}$ (Figs.12-13) at an angle Δ to the front face [4,138], where

$$\tan\Delta = \frac{(1-I_D)}{\cot(\theta_B - \theta_S) + I_D \cot(\theta_B + \theta_S)} . \quad (48)$$

However, due to conservation of neutrons in the Bragg diffraction viz.,

$$I_i = 1 = I_D + I_O + I_H , \tag{49}$$

these neutrons reach the side face of the Bragg prism if the crystal is sufficiently thick and get separated into two beams i.e., forward diffracted (I_O) and Bragg diffracted (I_H) beams.

If 2l is the width of the beam extent on the crystal surface, the widths of the incident and forward diffracted beams (Fig.12) respectively, are

$$2l\sin(\theta_B - \theta_S)$$

$$\text{and} \quad \frac{2l\sin\Delta\sin(A+\theta_B-\theta_S)}{\sin(A+\Delta)} . \tag{50}$$

Here A denotes the apex angle of Bragg prism.

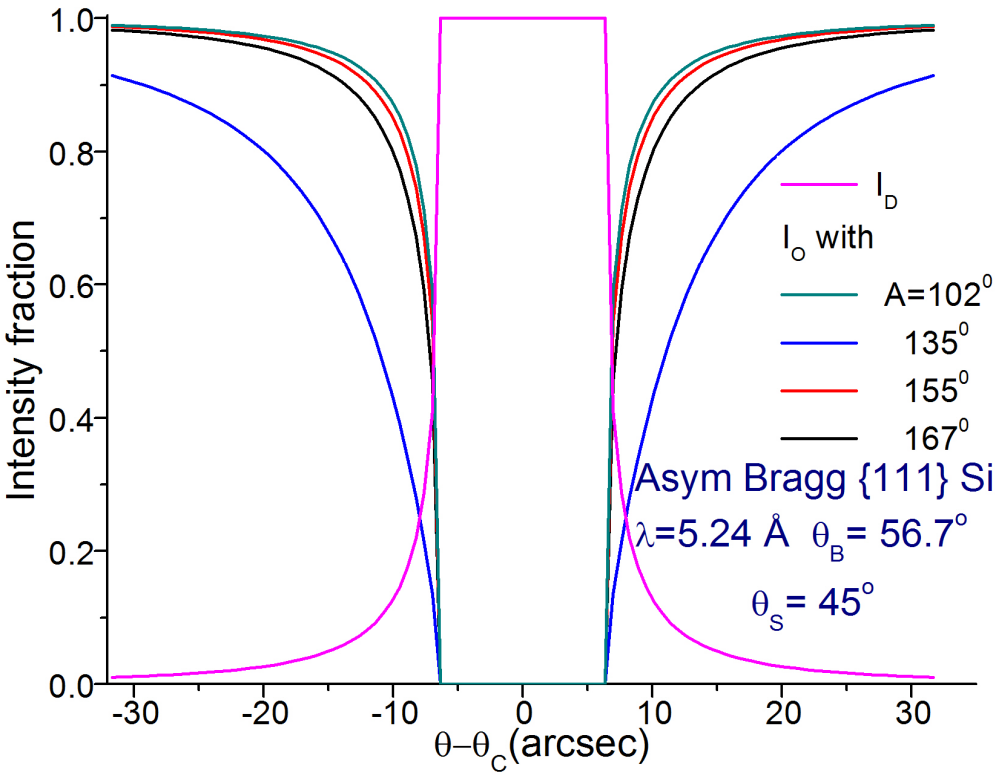

Fig.14 Variation of the diffracted (I_D) and transmitted (I_O) beam intensities with the angle of incidence for different apex angles A.

Therefore, the forward diffracted intensity (transmission) fraction as a function of incidence angle θ is given by

$$I_O(\theta) = \frac{\sin\Delta \sin(A+\theta_B-\theta_S)}{\sin(A+\Delta)\sin(\theta_B-\theta_S)}. \qquad (51)$$

The apex angle A of Bragg prism must lie between $\theta_B+\theta_S$ and $\pi-(\theta_B-\theta_S)$ to make possible the emergence of both I_O and I_H ($I_H = 1 - I_D - I_O$, expression derived in Chapter 4, cf. Eq.(61)), from the side face. Outside the total reflectivity domain, as apex angle 'A' approaches $\theta_B+\theta_S$, all the unreflected intensity $(1-I_D)$ tends to propagate in I_O (Fig.14), since the cross section for I_H approaches zero. As 'A' increases beyond $\theta_B+\theta_S$, the intensity fraction I_H rises at the expense of I_O.

3.3 Neutron deflection

We derive the neutron deflection formulae for the Bragg prisms of the forward diffracted beam by delineating the wave vectors change in reciprocal space determined by the boundary conditions at the incidence and exit faces of the prisms. The forward diffracted neutron (transmitted) beam show strong deflections sensitivities for neutron incidence close to total reflectivity regime, accompanied by a large concomitant loss of intensity due to appearance of Bragg reflection at front and Bragg prism diffraction at side faces, respectively. These transmitted neutrons exit the side face with a concomitant lateral displacement depending on the incidence angles θ and thus on the energy flow $\langle \mathbf{J_T} \rangle$ inside the crystal (Fig.12).

3.3.1 Bragg prism

To obtain the neutron deflection by a Bragg prism, we follow the same procedure as outlined for the amorphous prism except that now the internal wave vector must originate on the dispersion

surface instead of sphere QT'R' for an amorphous prism.

For neutron incidence along **RO** on the Bragg prism, the allowed internal wave vector in forward diffracted direction is hence **TO**, differing from **RO** only by the vector **RT** (Fig.13) along the incidence surface normal $\mathbf{n_i}$.

Likewise, at the exit surface, the emergent wave vector **SO** can be arrived at. The exit angle of the forward diffracted beam θ_B+LS/k_O, thus differs from the incidence angle (θ_B+LR/k_O) by the Bragg prism deflection –RS/k_O, written as

$$\delta_{cr} = (n - 1 + \frac{\xi_O}{k_O})\{\cot(\theta_B - \theta_S) - \cot(A + \theta_B - \theta_S)\}. \quad (52)$$

Here ξ_O symbolises the difference between magnitudes of **TO** and **T'O** and is obtained as

$$\xi_O = -\lambda b_C N \left\{\frac{\sin(\theta_B - \theta_S)}{\sin(\theta_B + \theta_S)}\right\}^{1/2} \left(\frac{F_H}{F_O}\right) y(1 - \sqrt{1 - y^{-2}}). \quad (53)$$

Here, symbols have their usual meanings viz., y denotes scaled deviation of incidence angle θ from centre of Bragg diffraction θ_C (cf. Eq.(27)), F_O and F_H stand for structure factor magnitude for **O** and **H** reflection respectively. ξ_O is positive and negative respectively for α (y<0) and β (y>0) branches of the dispersion surface. The difference between δ_{cr} and δ_{am} thus originates from ξ_O which vanishes for an amorphous material. ξ_O and hence the deflection δ_{cr} vary sharply with incidence angle, the reflection {hkl} and asymmetry of Bragg configuration θ_S. δ_{cr} reaches extrema at either end of the total reflection domain, viz., y=±1 and can be enhanced for the opposite asymmetry (viz., $\theta_S \sim -\theta_B$) and by employing full {hkl} reflections ($F_O \approx F_H$).

Eqs.(53) in (52), lead to the relation,

$$\delta_{cr} = \delta_{am}\left\{1 + \frac{F_H}{F_O}\sqrt{\frac{\sin(\theta_B - \theta_S)}{\sin(\theta_B + \theta_S)}}\, y\left(1 - \sqrt{1 - y^{-2}}\right)\right\}. \quad (54)$$

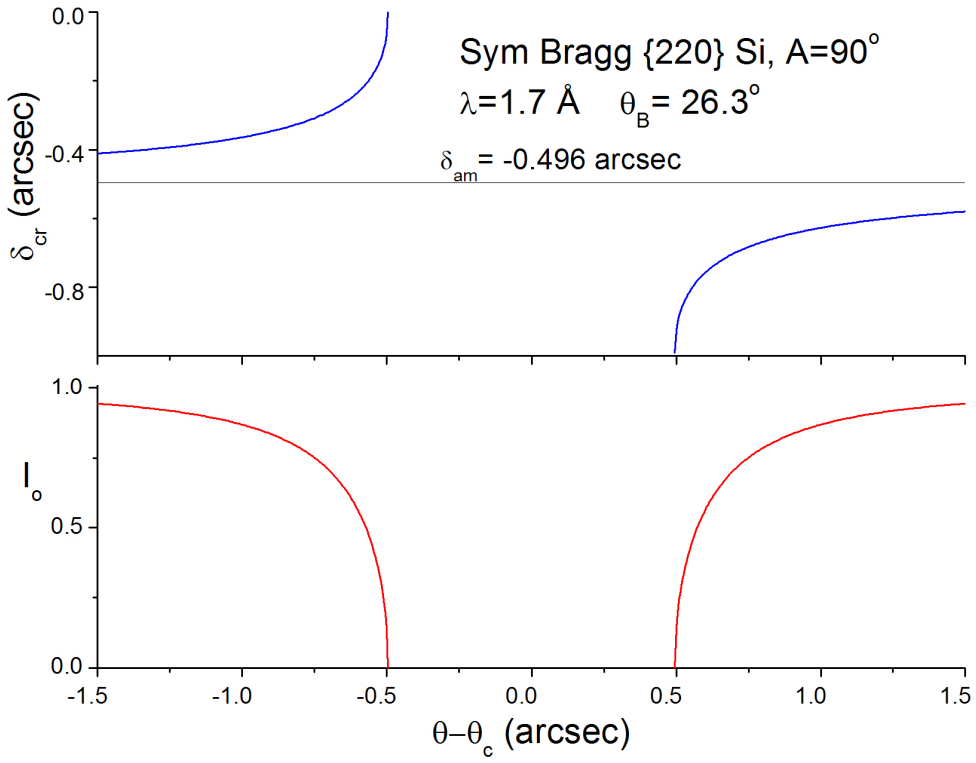

Fig.15 Calculated δ_{cr} and I_O for a symmetric Bragg prism.

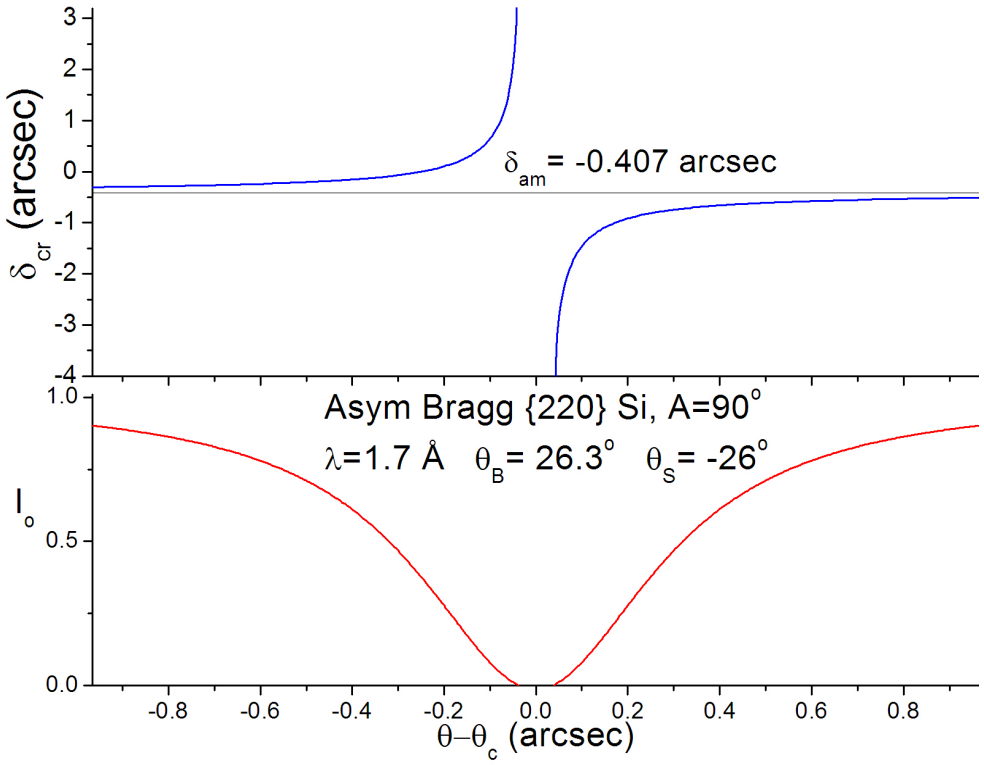

Fig.16 Calculated δ_{cr} and I_O for an asymmetric Bragg prism.

The high sensitivity of neutron deflection δ_{cr} of Bragg prism stems from dynamical diffraction effects. Figs.15 and 16 depict the deflection and forward diffracted intensity fraction by a right-angled Bragg prisms for symmetric and asymmetric {220} configurations. At incidence angles well off a Bragg reflection, δ_{cr} equals the amorphous prism deflection δ_{am}. As the Bragg reflection is approached from the low θ-side, δ_{cr} increases monotonically, reaching a maximum at the onset of total reflectivity. On approaching the Bragg reflection from the higher angle side, the deflection decreases symmetrically by the same amount, attaining a corresponding minimum at the other extreme of total reflectivity. Si {220} being a full reflection ($F_H \approx F_O$), the maximum in δ_{cr} at $y = -1$ nearly equals zero in the symmetric (cf. Eq.(54)) configuration (Fig.15). In the asymmetric case (Fig.16), the deflection even changes sign on the low θ-side, eventually exceeding $-7\delta_{am}$ and displaying a much greater sensitivity to θ-variation. For partial reflection like Si {111}, δ_{cr} deviation from δ_{am} is reduced to 70.7% of the full reflection value as $F_H/F_O \approx .707$. Contrary to the typical $|d\delta_{am}/d\theta|$ values of arcsec/deg attainable with an amorphous prism, a Bragg prism affords several orders of magnitude greater sensitivities $|d\delta_{cr}/d\theta| \sim$ arcsec/arcsec.

3.3.2 Back Face contribution to neutron forward diffraction

If the crystal is thin in the direction normal to the incidence surface, at moderate values of the angle Δ, the neutron flow along $\mathbf{J_T}$ reaches the back face (assumed parallel to the incidence surface). At the back face, two beams viz., partially transmitted and partially reflected, are generated with amplitudes and wave vectors determined by the respective boundary conditions. Boundary conditions at the back face excite the other tie point B. These partially reflected neutrons travel along current density vector $\mathbf{J_B}$ at an angle Δ_b, say, to the back face, (Figs.12-13) given by

$$\tan\Delta_b = \frac{(1-I_D)}{I_D\cot(\theta_B-\theta_S)+\cot(\theta_B+\theta_S)}. \qquad (55)$$

These neutrons reach the side face and an intensity fraction

$$I_O^b(\theta) = \frac{I_D^2 \sin\Delta_b \sin(A+\theta_B-\theta_S)}{\sin(A-\Delta_b)\sin(\theta_B-\theta_S)}, \qquad (56)$$

emerges deflected from the incident direction by the angle

$$\delta_{cr}^b = \delta_{am}\left\{1+\frac{F_H}{F_O}\sqrt{\frac{\sin(\theta_B-\theta_S)}{\sin(\theta_B+\theta_S)}}y\left(1+\sqrt{1-y^{-2}}\right)\right\}. \qquad (57)$$

The back face intensity fraction is tiny compared to the side face intensity fraction (Fig.17). By a judicious choice of the Bragg reflection and its asymmetry, $d\delta_{cr}^b/d\theta$ can be made equal to –1 at a reasonable y^2-value. The prism will then act as a collimator for the neutron beam, albeit with a concomitant large loss in the beam intensity.

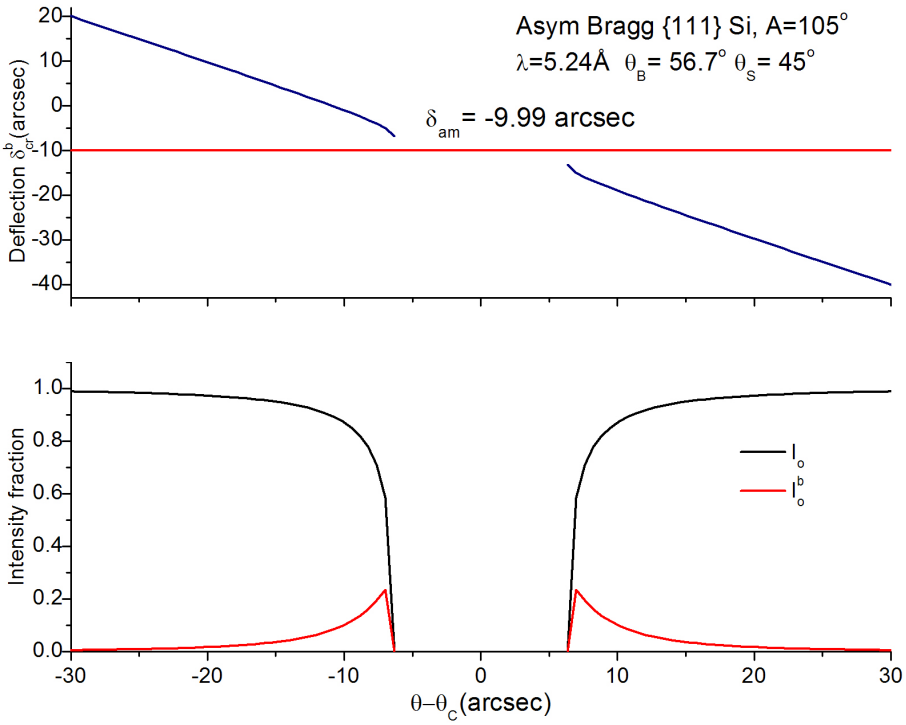

Fig.17 Calculated δ_{cr}^b and I_{cr}^b for an asymmetric Bragg prism.

3.4 Experimental

The experiment was carried out with the Bonse-Hart camera set up at the V12b double crystal spectrometer (Fig.18) at the BERII 10 MW reactor of Helmholtz Zentrum Berlin. Within the channel-cut monochromator as well as analyser silicon crystals, each performing 7 {111} Ewald reflections, a Si wedge each was inserted after 3 reflections to deflect neutrons of 5.24 Å by about 4 arcsec. An analyser rocking curve width ~ 2 arcsec was thus attained. The large wavelengths allowed only the {111} silicon Bragg prisms since for all other planar spacings of allowed Si reflections, $2d<\lambda$. Si {111} reflection eliminated higher order contamination in the diffracted beam. Si crystal is ideal for these studies due to its low absorption and low incoherent scattering cross section for neutrons. Moreover, large single crystals of Si are readily available at a reasonable price.

Two symmetric {111} prisms of apex angles A equal to 56.7° and 90° and two asymmetric {111} prisms with asymmetry angles θ_S of 35° and 41° and apex angles of 94° and 98° respectively were investigated. The Bragg Si prisms were prepared from dislocation free Si ingots. The ingot was mounted on a goniometer and its {111} planes were located and marked using Bragg reflection of neutrons at the Dhruva reactor in Mumbai, India. Precision cuts were made by employing a wobble free diamond cutting wheel aligned at the desired asymmetry angles θ_S with {111} planes. The side face was then cut at the required apex angle A. Cuts were performed at a carefully optimised rotation speed to avoid scratches on the front as well as side faces of the Bragg prisms. The prisms were then slowly etched in a solution of hydrofluoric acid (HF) and nitric acid (HNO_3) in 1:20 ratio for 20 minutes to remove all strain and damage introduced during the cutting process.

A Bragg prism was placed between the monochromator and analyser. Only a part of the neutron beam illuminated the Bragg prism, the remaining beam reaching the analyser directly to serve as a

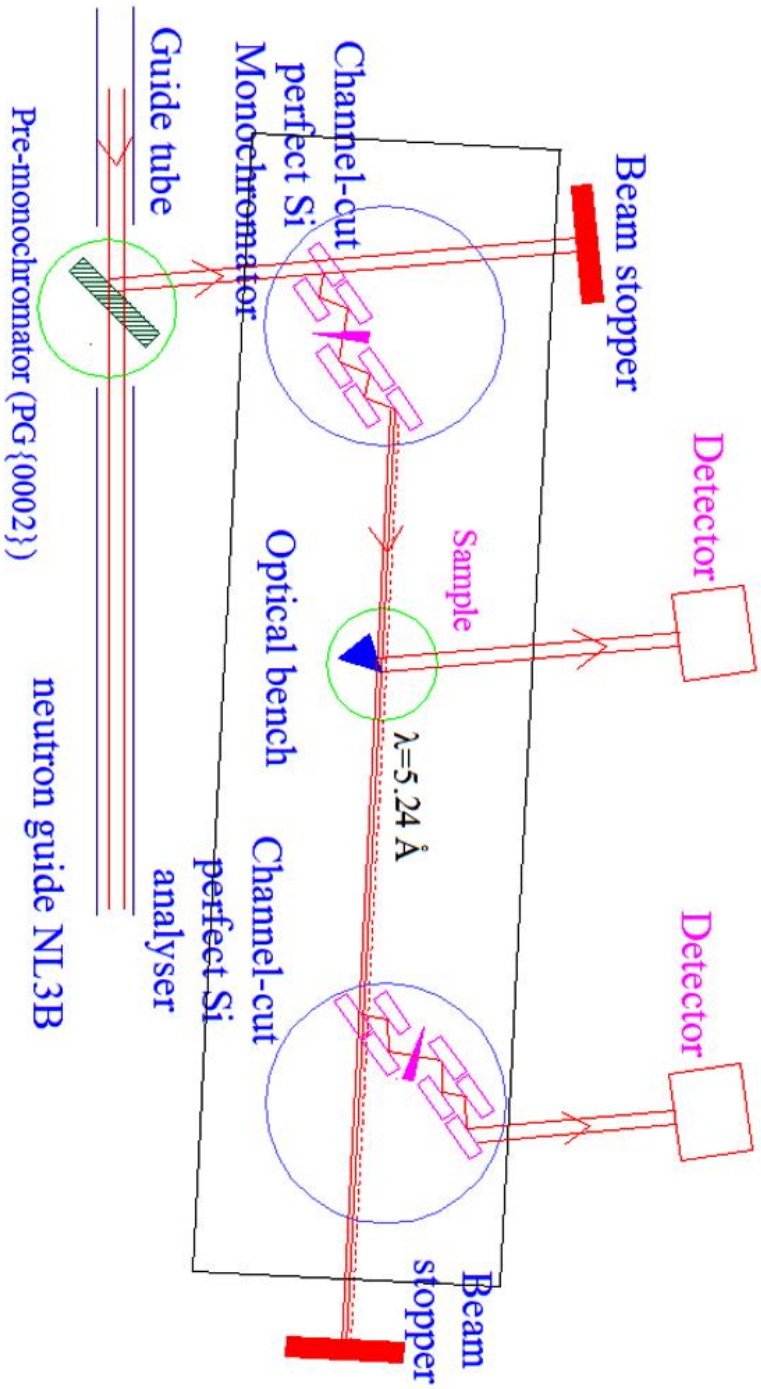

Fig.18 Experimental layout to measure neutron deflection and transmission by a Bragg prism. The set up employs 7X7 reflections each in the monochromator and analyser channel-cut crystals of a 5.24 Å neutron beam with a silicon prism suspended in each crystal between 3rd and 4th reflections and sample (Bragg prism) was placed between the monochromator and analyser.

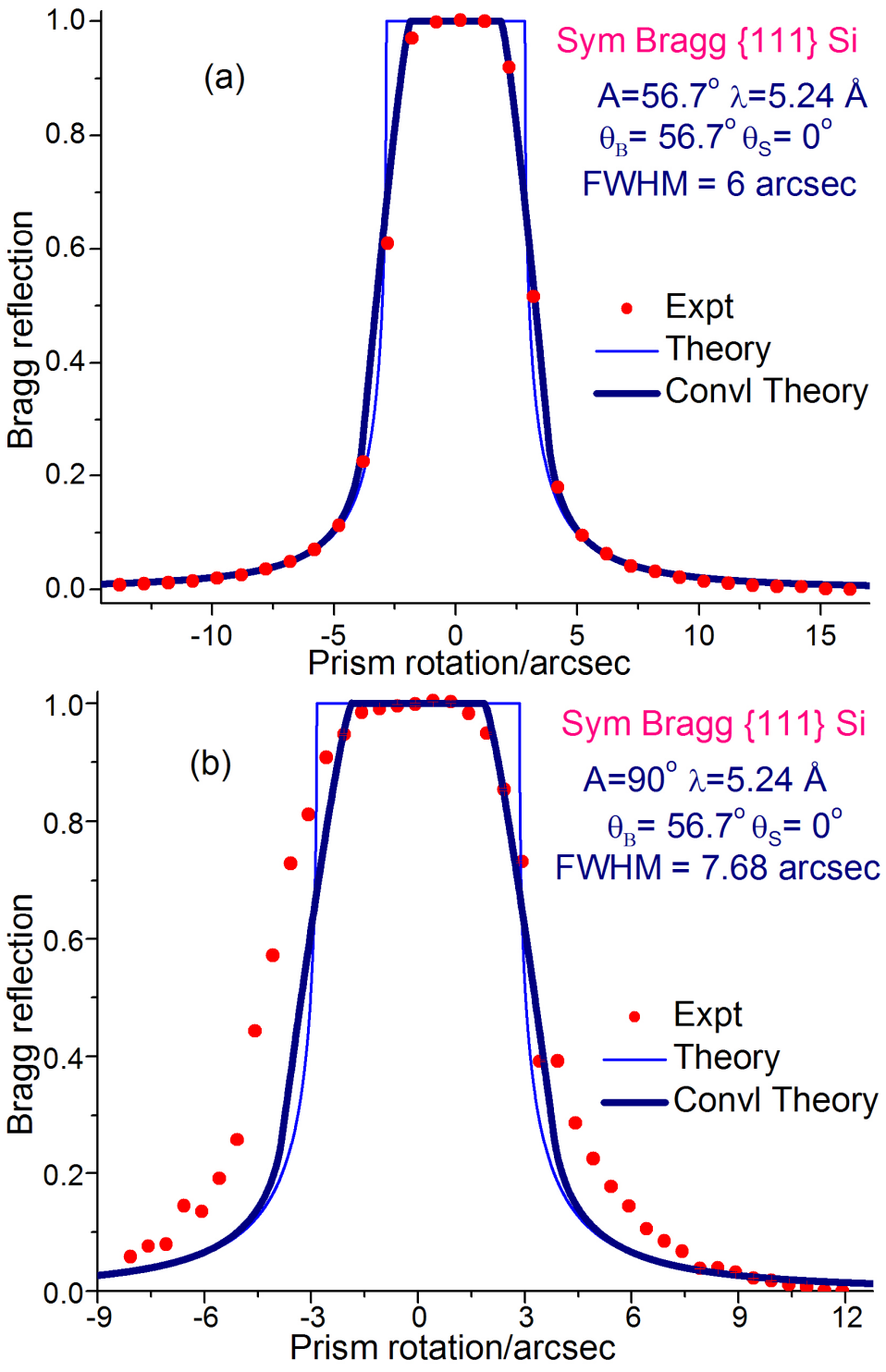

Fig.19 Bragg reflection intensity fraction as a function of prism rotation for the symmetric Bragg {111} prism reflection with apex angles A of (a) 56.7° and (b) 90°, respectively.

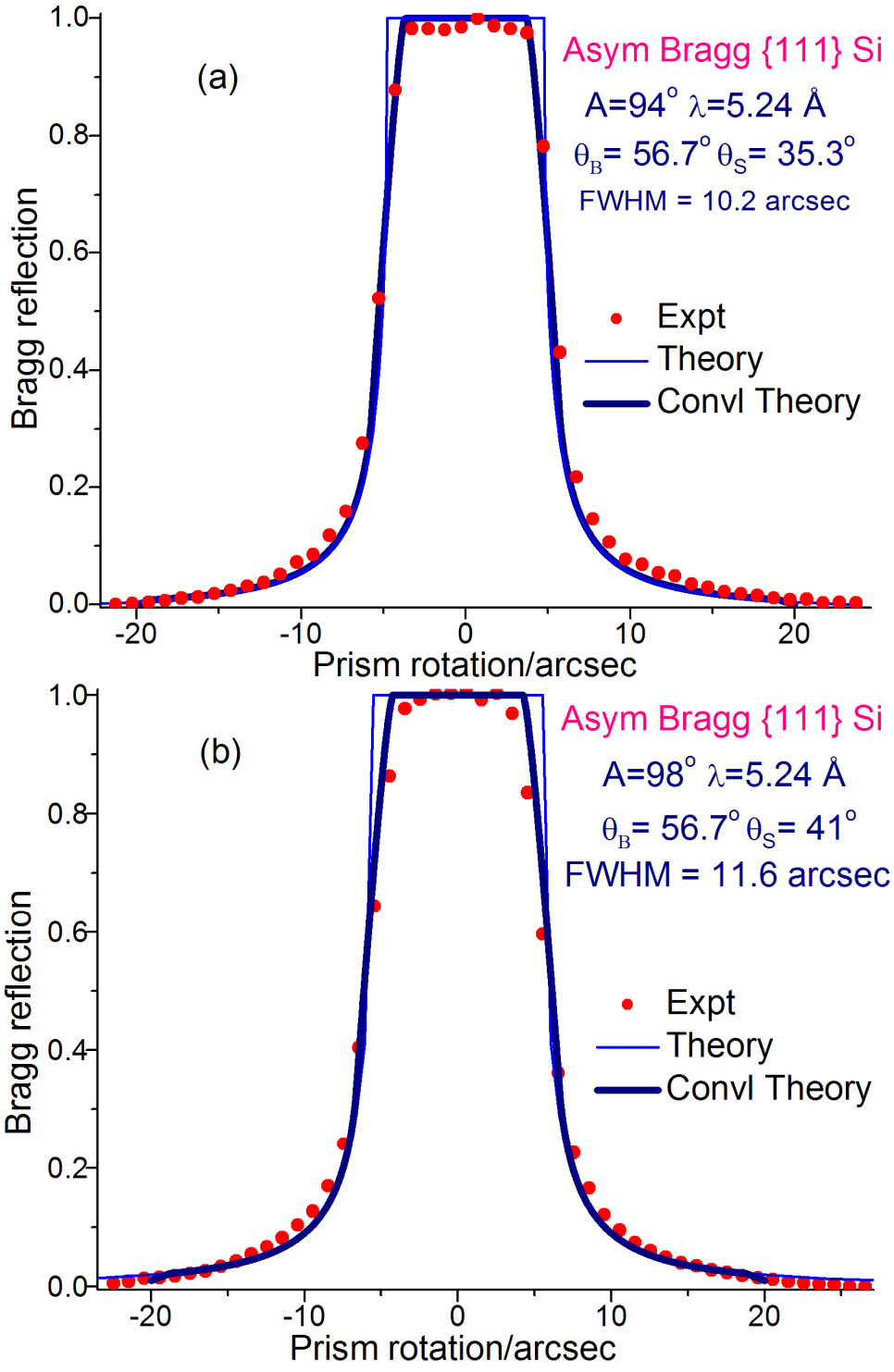

Fig.20 Bragg reflection intensity fraction as a function of prism rotation for the asymmetric Bragg {111} prism reflection with asymmetry angles θ_S and apex angles A being (a) 35° and 94° (b) 41° and 98°, respectively.

reference for the prism deflection measurement (Fig.18). Using an additional detector to record neutrons Bragg reflected from the prism, the few arcsec wide Bragg reflection of the prism was located and optimised by adjusting the prism tilt. The analyser rocking curves were recorded for several angles of incidence at the prism covering a span of about 40 arcsec centred at the total reflectivity domain. The direct and deflected neutron peaks were thus simultaneously recorded in each analyser scan. The Bragg reflection intensity of the prism was continuously monitored to confirm the stability of the prism orientation. The observed full width at half maximum (FWHM) of 6 arcsec for the Bragg reflection of the symmetric prism with apex angle A of 57° confirmed the absence of strains and defects in the prism (Fig.19a). However, the other symmetric prism (A = 90°) yielded a FWHM of 7.68 arcsec instead of 6 arcsec predicted by theory, indicating residual strain and a slight asymmetry ($\theta_S \neq 0°$) of the prism (Fig.19b). For the other two asymmetric Si {111} Bragg prisms with θ_S of 35° and 41° and apex angles 94° and 98° respectively, the measured rocking curve FWHMS were 10.2 arcsec (Fig.20a) and 11.6 arcsec (Fig.20b) respectively in agreement with those expected for the corresponding asymmetry angles θ_S of these prisms. The term 'Convl Theory' in Figs., signifies theoretical curves convoluted with 2 arcsec wide rectangular angular profile of the monochromated beam.

3.5 Results and Discussion

The analyser rocking curve recorded at two typical incidence angles for a Bragg prism is displayed in Fig.21. Least-squares Voigt function fits (smooth curves) were made to the direct and deflected neutron peaks in the rocking curve. At each θ, the neutron deflection δ_{cr} was determined from the angular shift between the fitted peaks for the direct and deflected beams. The area under the deflected peak corrected for the background was computed to infer the transmitted intensity

fraction I_O through the Bragg prism. The area parameter of the fitted Voigt peak for deflected neutrons also yielded the same I_O. Figs.22, 23, 24 and 25 depict the experimental (points) and theoretical (curves) deflections δ_{cr} and transmitted neutron fractions I_O by the four Bragg prisms mentioned above. The thin curves represent Eqs.(51) and (54), incorporating the appropriate Debye Waller factor for {111} Si reflections at 293^{o}K. To explain the significant departures of the observed δ_{cr} and I_O from the thin curves for incidence near and within the total Bragg reflectivity domain, we accounted for the finite instrument resolution. We convoluted the 2 arcsec wide incident neutron angular profile, deflected and attenuated by the Bragg prism vide Eqs.(51) and (54), with the 2 arcsec wide acceptance curve of the analyser to simulate the deflected neutron peak. Each thick curve in Figs.22, 23, 24 and 25 represents δ_{cr} or I_O obtained for such simulated peaks. Near the total reflectivity region, I_O (cf. Eq.(51)) drops sharply on the total reflectivity side of the incident angular profile (bottom curve, Fig.21). The deflected peak thus gets skewed on the other side. The resultant low weightages for I_O and δ_{cr} on the total reflectivity side of the asymmetric deflected peak rounds off the sharp (thin) I_O curve and turns the δ_{cr} curve back towards δ_{am}. The neutron deflection and transmitted intensity fraction data agree well with these convoluted (thick) curves. The observed maximum deflection sensitivities $|d\delta_{cr}/d\theta|$ viz., the rate of δ_{cr} variation with incidence angle θ, corresponding transmissions and percentage variations in maximum δ_{cr} from their δ_{am} values respectively, for various Bragg prisms are presented in table 2. The quantities $|d\delta_{cr}/d\theta|$ and $|\delta_{cr} - \delta_{am}|/|\delta_{am}|$ vary sharply near the total reflectivity region. The observed δ_{cr} deviate from δ_{am} by >29% for symmetric prism (A = 90°), but it exhibited $|d\delta_{cr}/d\theta|$ of only 0.22 arcsec/arcsec corresponding to a small transmission of 0.47, further, the observed δ_{cr} and I_O curves showed deviations from the theoretical curves for this Bragg prism.

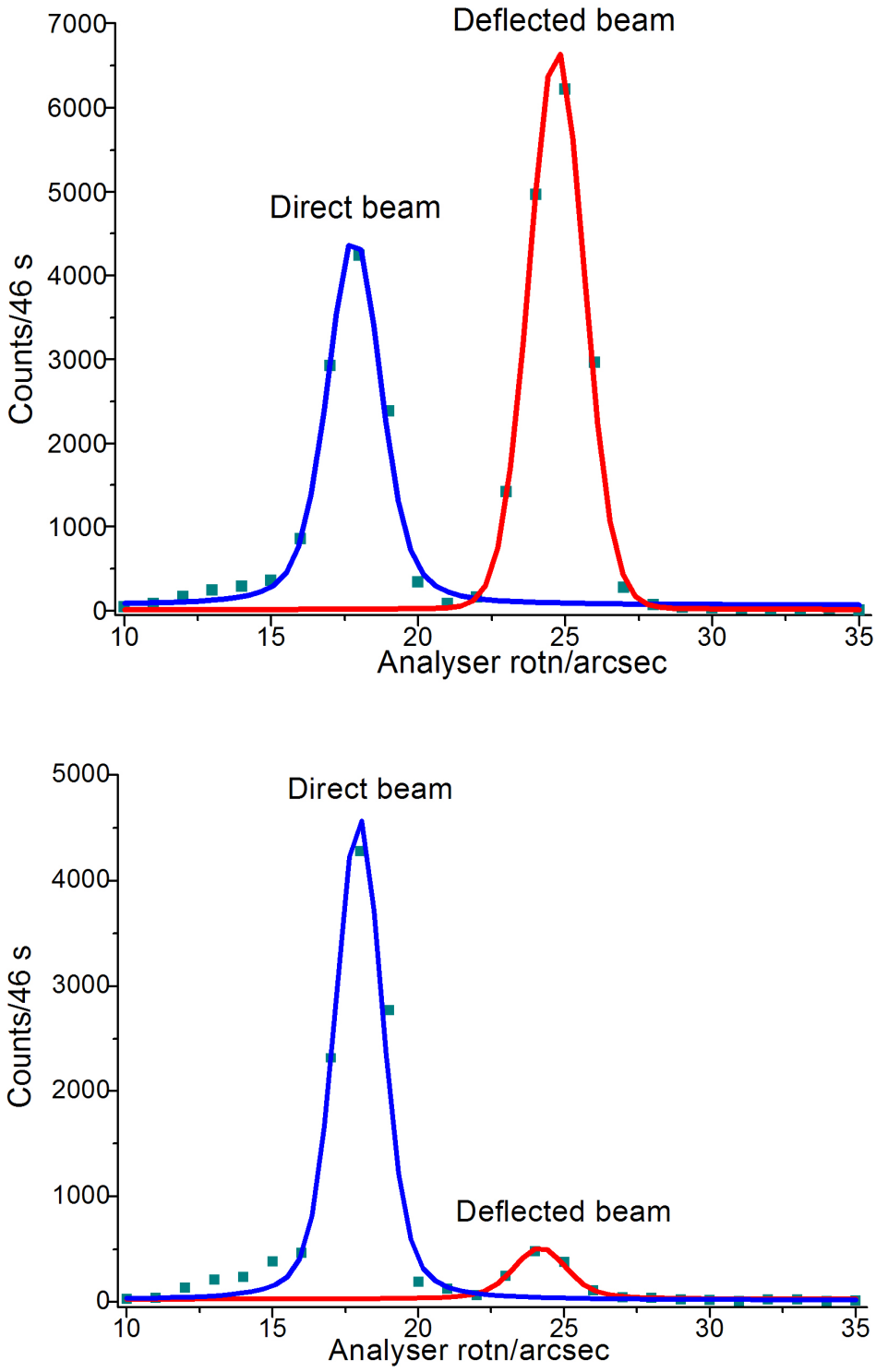

Fig.21 Typical Voigt function fits (curves) to the direct and deflected beam scans (points) for an asymmetric Bragg prism: θ_S=41° and A=98° at off Bragg condition (θ= -12.85) (top) and near Bragg condition (θ= -4.85) (bottom).

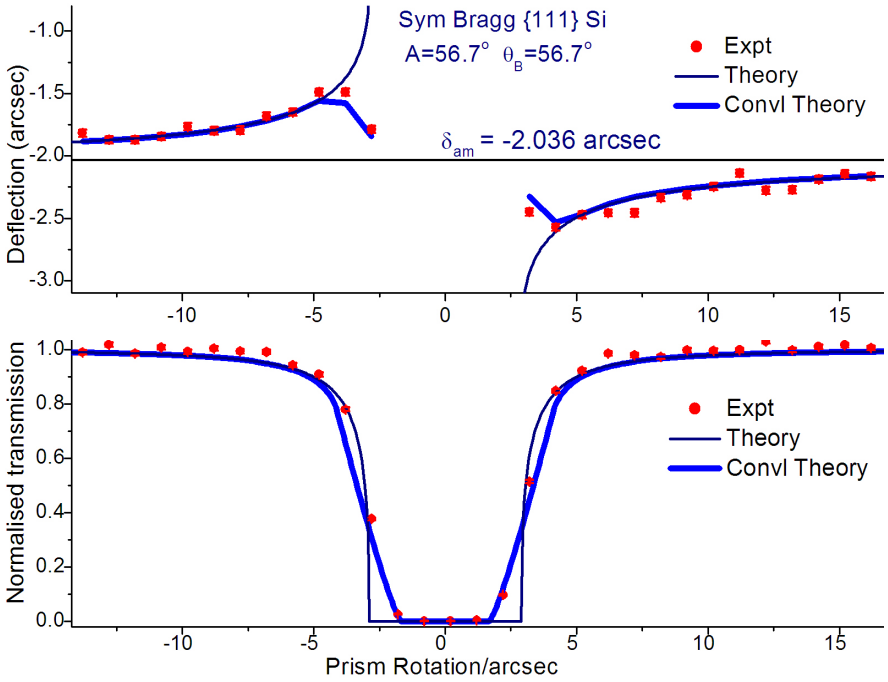

Fig.22 Experimental (points) and theoretical (curves) values of δ_{cr} and I_O for a symmetric Bragg prism with A=56.7°.

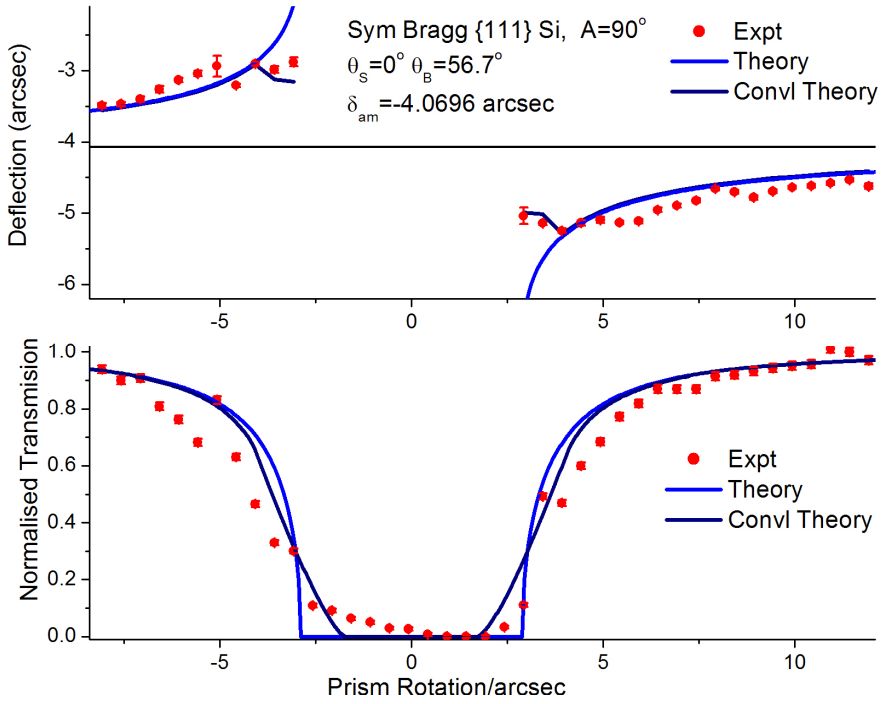

Fig.23 Experimental (points) and theoretical (curves) values of δ_{cr} and I_O for a symmetric Bragg prism with A=90°.

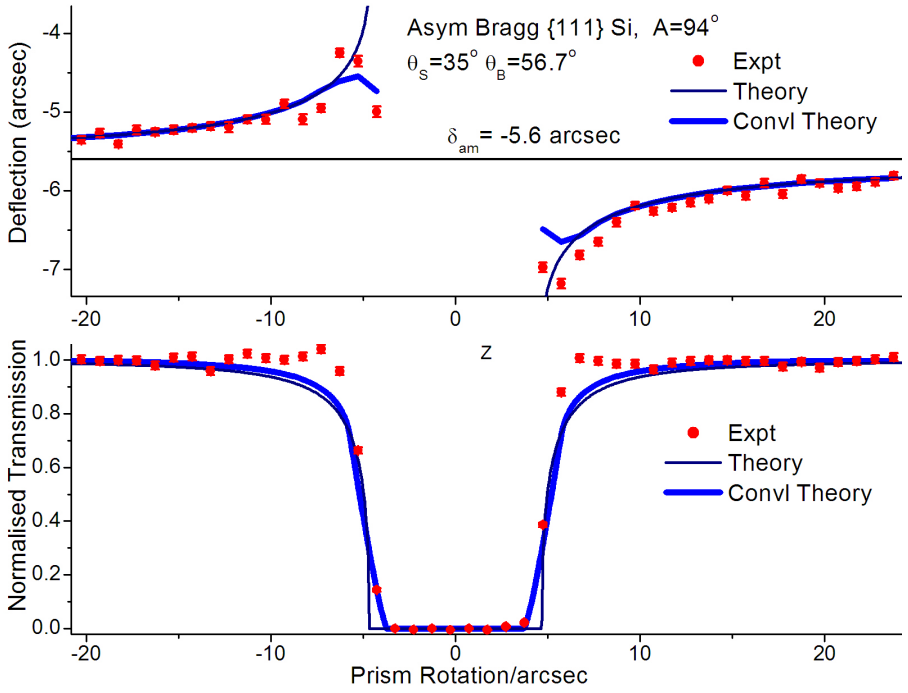

Fig.24 Experimental (points) and theoretical (curves) values of δ_{cr} and I_O for an asymmetric Bragg prism: θ_S=35° and A=94°.

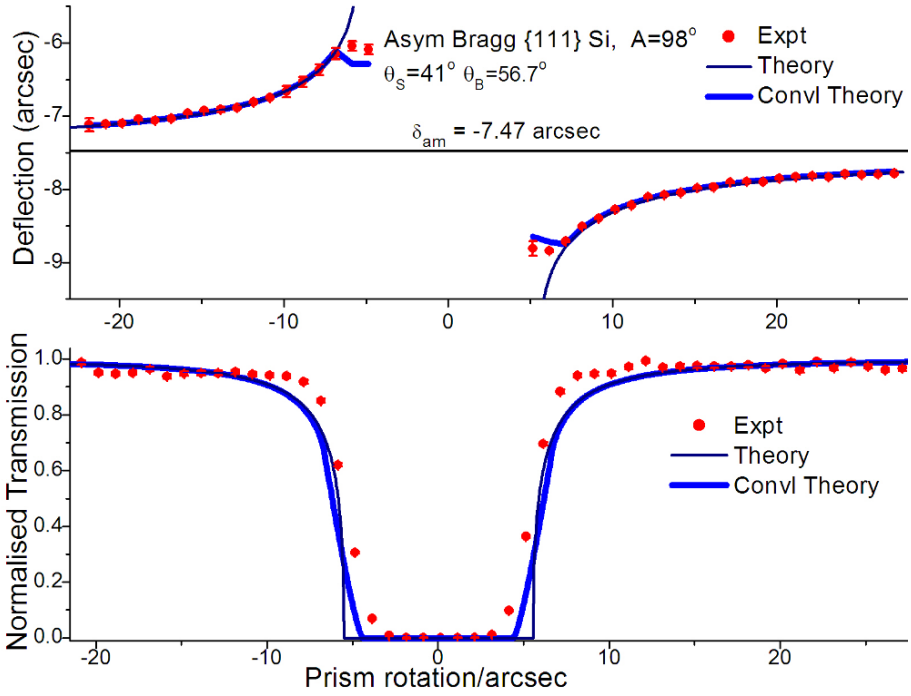

Fig.25 Experimental (points) and theoretical (curves) values of δ_{cr} and I_O for an asymmetric Bragg prism: θ_S=41° and A=98°.

Table 2: Observed deflection sensitivities, corresponding transmissions and percentage variations in the deflections for various Bragg prisms from their respective amorphous prisms.

Bragg Prisms	Sensitivity $\lvert d\delta_{cr}/d\theta \rvert$ (arcsec/arcsec)	Transmission I_O	$100\cdot(\lvert\delta_{cr}-\delta_{am}\rvert/\lvert\delta_{am}\rvert)_{max.}$ (%)
Sym. (θ_S=0°) and A=56.7°	0.16	0.78	27
Sym. (θ_S=0°) and A=90°	0.22	0.47	29.5
Asym. (θ_S=35°) and A=94°	0.43	0.96	27
Asym. (θ_S=41°) and A=98°	0.23	0.88	19

The best results however, were observed with the asymmetric prism of θ_S=35° and A=94°, exhibiting δ_{cr} deviation from δ_{am} by upto 27% with sensitivities $\lvert d\delta_{cr}/d\theta \rvert$ upto 0.43 arcsec/arcsec corresponding to a transmission of 0.96. These observed sensitivities $\lvert d\delta_{cr}/d\theta \rvert$ are several orders of magnitude greater than those obtainable with amorphous prisms [139-145].

Encouraged by this experimental verification of predictions of the dynamical diffraction theory, we designed, fabricated and successfully operated a super-collimator monochromator delivering a Bragg prism diffracted (I_H) neutron beam of sub-arcsec angular width described in Chapter 4.

CHAPTER 4

First sub-arcsec collimation of a monochromatic neutron beam

4.0 Introduction

I present in this chapter, a novel device producing a tail-free plane-wave-like neutron beam of sub-arcsec angular width. Neutrons incident on a single crystal prism in an asymmetric Bragg configuration undergo, in addition to the Bragg reflection, diffraction at the exit face [138] of the prism. Two small diffraction peaks I_H, one on either side of the Bragg reflection, appear outside the

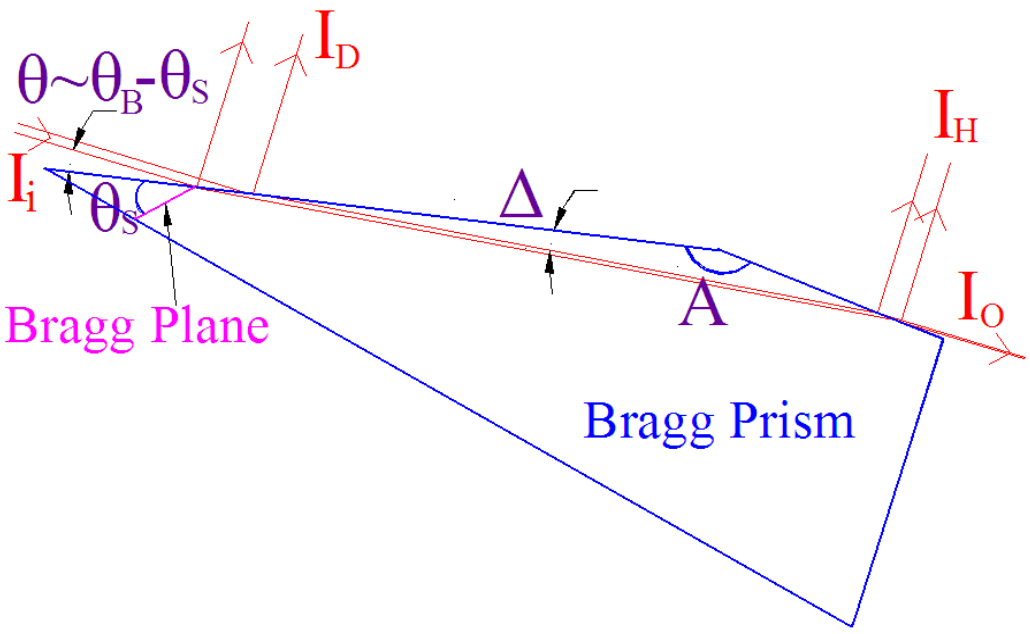

Fig.26 Asymmetric Bragg prism diffraction (schematic). Outside the total reflectivity domain, unreflected neutrons traverse the prism at an angle Δ to the incidence surface and exit the side face in diffracted (I_H) and forward diffracted (I_O) beams. At large enough angles Δ, neutrons reach the part of the side face cut along the diffracted beam direction and exit wholly into the I_O beam, thus truncating I_H on the larger-$|y|$ side as well to yield a tail-free, sharp angular profile.

total reflectivity domain. These arise since unreflected neutrons propagate into the crystal at an angle Δ to the incidence surface due to dynamical diffraction and emerge from the side face, if the apex angle A between the front and side faces lies between $\theta_B+\theta_S$ and $\pi-\theta_B+\theta_S$ (cf. Fig.12, Chapter 3). The prism diffracted beam, albeit weaker than the Bragg reflection, can be made much narrower. Its intensity can furthermore be made to drop to zero within a fraction of an arcsec on either side of the peak centre by judiciously positioning the incident beam and tailoring the exit face orientation at large depths. We have named this super collimator-monochromator device a 'Bragg prism collimator' (Fig.26).

4.1 Bragg prism diffraction

We revisit neutron beam incidence on a single crystal prism (Fig.12) just outside the total reflectivity domain such that the incident vacuum wave vector is **RO** in reciprocal space corresponding to the angle of incidence, θ_B+LR/k_O (Fig.27). Continuity of the tangential components of the wave vectors at the incidence interface and physical constraint on the energy flow direction into the thick single crystal allow the excitation of only a single tie point T on the dispersion surface (Chapter 3). At the exit surface, which subtends an angle A with the front face, following the same boundary condition, a line is drawn from T along the exit surface normal $\mathbf{n_e}$ to intersect vacuum spheres of incidence and diffraction at point S and E respectively. The emergent wave vectors are therefore **SO** and **EH** in forward diffracted and Bragg diffracted directions, respectively.

The Bragg diffracted intensity fraction I_H of the Bragg prism as a function of the incidence angle can be written as

$$I_H(\theta) = C(\theta) \bullet \left| \frac{\psi_H}{\psi_O} \right|^2 . \qquad (58)$$

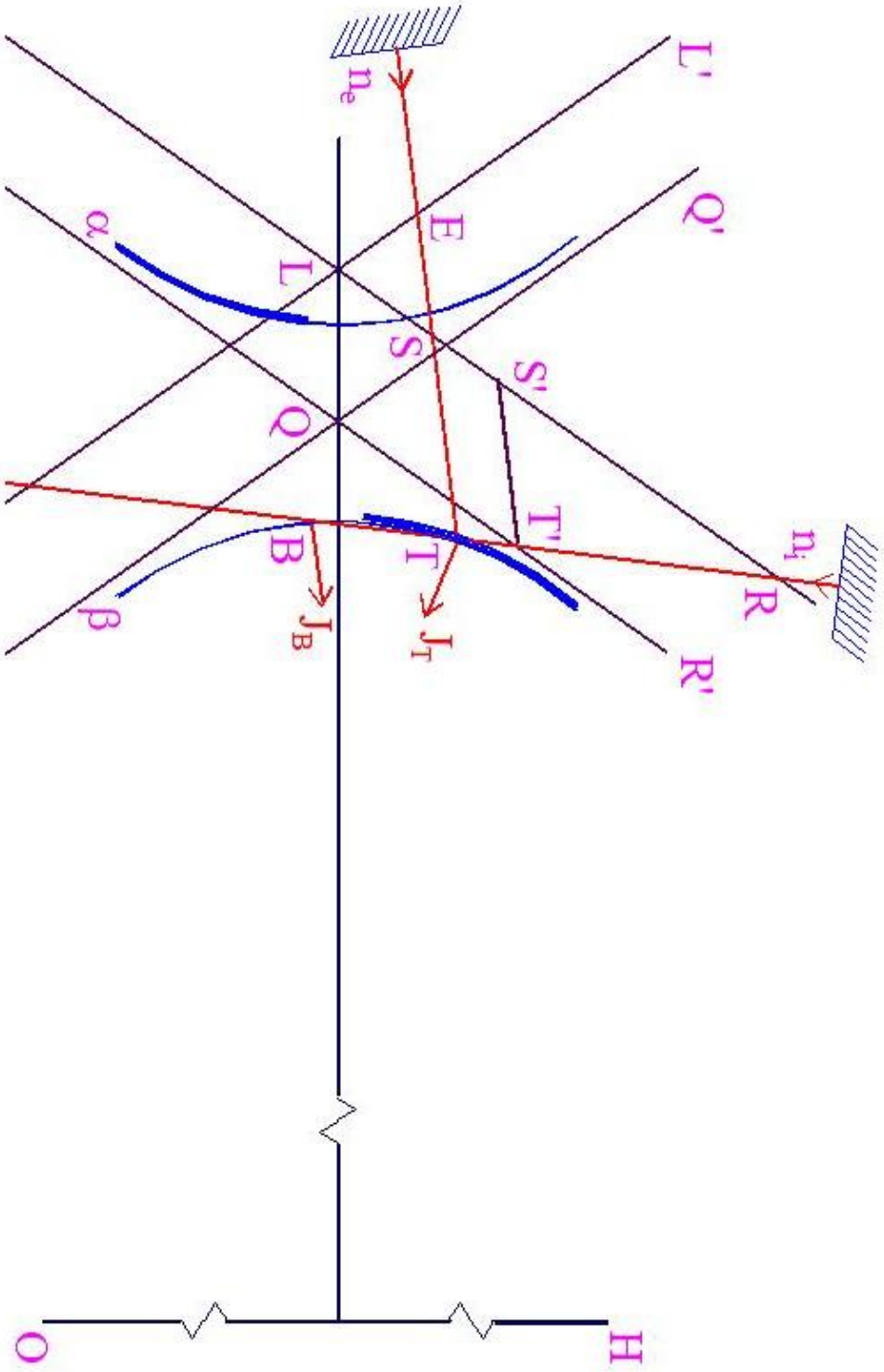

Fig.27 Bragg diffraction of a neutron beam in reciprocal space. At each incidence angle, continuity of tangential components of wave vectors across the incidence and exit faces of the prism yields unique tie points as well as internal and emergent wave vectors.

Here the term C(θ) accounts for the phase space volume conservation of the neutron beam, and is calculated in the same manner as in Eq.(51) i.e., by computing the H-beam cross section,

$$C(\theta) = \frac{\sin\Delta \sin(A-\theta_B-\theta_S)}{\sin(\theta_B-\theta_S)\sin(A+\Delta)} \ . \tag{59}$$

Employing Eq.(48), Bragg diffraction fraction can be written as

$$\left|\frac{\psi_H}{\psi_O}\right|^2 = \frac{\sin(\theta_B-\theta_S-\Delta)}{\sin(\theta_B+\theta_S+\Delta)}. \tag{60}$$

Thus, Eq.(58) becomes,

$$I_H(\theta) = \frac{\sin\Delta \sin(A-\theta_B-\theta_S)\sin(\theta_B-\theta_S-\Delta)}{\sin(\theta_B-\theta_S)\sin(A+\Delta)\sin(\theta_B+\theta_S+\Delta)}. \tag{61}$$

Bragg diffracted H-beam cross section C(θ), vanishes at $A=\theta_B+\theta_S$ (cf. Eq.(61)) making forward diffracted beam $I_O(\theta)$ stronger at the expense of H-beam. To obtain strong $I_H(\theta)$ beam from side face, the apex angle A must lie close to $\pi-\theta_B+\theta_S$.

The exit angle θ_B–LE/k_O, of the Bragg Diffracted neutron beam $I_H(\theta)$ from side face is derived to be

$$\theta_H(\theta) = -\frac{\chi_H y}{\sin(A-\theta_B-\theta_S)\sqrt{|b|}}\left\{\frac{\sin(A+\theta_B-\theta_S)}{\sin(2\theta_B)} - \frac{\sin A\left(1-\sqrt{1-y^{-2}}\right)}{2\sin(\theta_B+\theta_S)}\right\}, \tag{62}$$

up to an additive constant.

We rewrite Eq. (62) as

$$\theta_H(\theta) = -\frac{2|n-1|\,y}{\sin(A-\theta_B-\theta_S)\sqrt{|b|}}\left|\frac{F_H}{F_O}\right|\left\{\frac{\sin(A+\theta_B-\theta_S)}{\sin(2\theta_B)} - \frac{\sin A\left(1-\sqrt{1-y^{-2}}\right)}{2\sin(\theta_B+\theta_S)}\right\}. \tag{63}$$

As can be seen from Eq.(63), θ_H depends on the Bragg reflection through F_H, θ_S and the apex angle A. So a judicious choice of these parameters can make the derivative $\partial\theta_H/\partial\theta$ approach 0. The single

crystal then acts as a super collimator for the neutron beam. Similarly an analyser, in the opposite asymmetric crystal configuration ($|b|\rightarrow|b|^{-1}$), can be made to accept an extremely narrow angular range. An odd Bragg reflection such as {111}, where $F_H/F_O \approx 0.707$, reduces the θ as well as θ_H variations to about 70.7% of those for a full reflection ($F_H \approx F_O$) like {220}, effecting better neutron collimation. The exit angle variation rate with incidence angle may be expressed as

$$\frac{\partial\theta_H}{\partial\theta} = -\frac{\sin(\theta_B-\theta_S)\sin(A+\Delta)}{\sin\Delta\sin(A-\theta_B-\theta_S)}. \qquad (64)$$

The angular compression factor of the collimator is then the negative reciprocal of this derivative. For neutron incidence well off the Bragg incidence, viz, $|y|>>1$, $\Delta\rightarrow\theta_B-\theta_S$ and $\partial\theta_H/\partial\theta$ approaches $-\sin(A+\theta_B-\theta_S)/\sin(A-\theta_B-\theta_S)$ affording a large compression factor. In the other extreme close to the total reflectivity regime however, $|y|\rightarrow1$, $\Delta\rightarrow0$ and θ_H varies sharply, the θ_H slope tending to $-\infty$ at $|y|=1$ thus yielding zero compression. An overall compression factor of about 10 in θ_H can thus be attained over the full I_H peak. In the next section, we describe the Bragg prism design in detail.

4.2 Bragg prism design

Consider 5.26 Å neutron beam incidence on a single crystal Si {111} prism with $\theta_S=50.1^o$ and $A=172^o$. Fig.28 depicts Bragg reflection and prism diffraction intensity fraction variation curves with incidence angle for this Bragg prism. The Bragg reflection peak exhibits an FWHM of 17.3 arcsec. Outside the total reflectivity window, two Bragg prism diffraction $I_H(\theta)$ peaks, of 9.9 arcsec FWHM each, appear with long tails.

For glancing incidence, the diffracted beam cross section gets enhanced over that of the incident beam. Conservation of the phase space volume occupied by the beam dictates that the exit angle

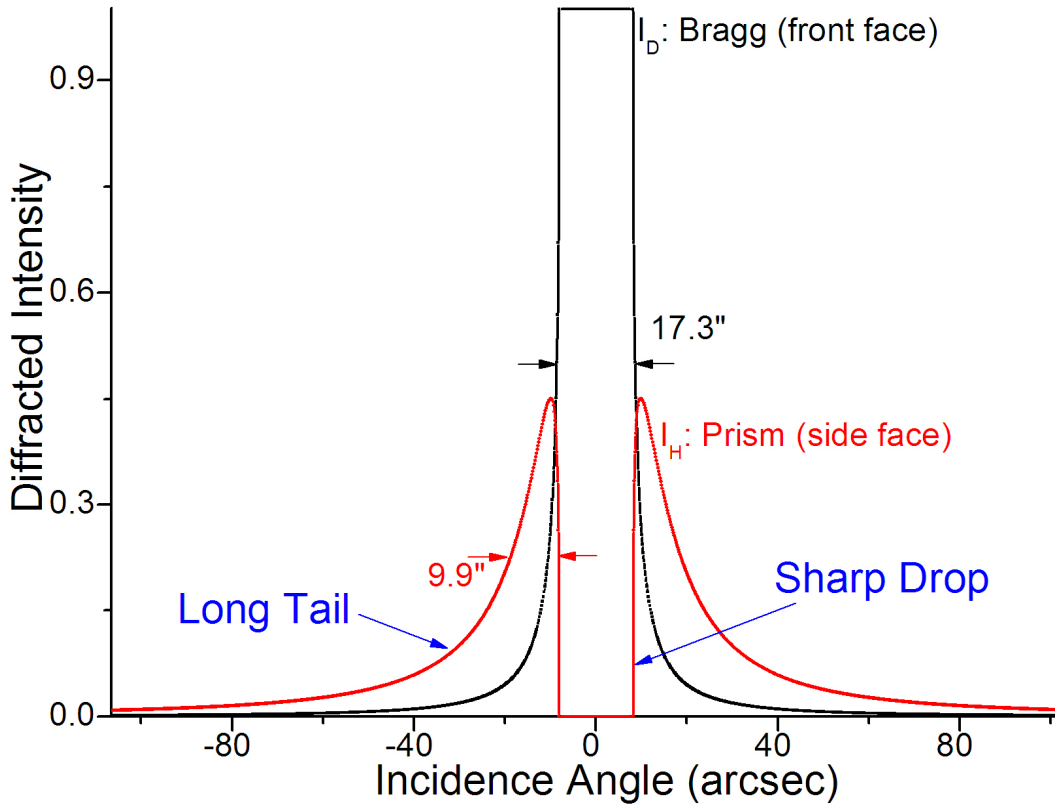

Fig.28 Theoretical curves for Si {111} Bragg reflection and prism diffraction of 5.26 Å neutrons with A=172^o and θ_S=50.1^o as a function of the incidence angle.

scale gets compressed by the same factor relative to θ (cf. Eq.(64)). The dependence of the diffracted intensity on the exit angle thus becomes (cf. intensity curves in Figs.29-31)

$$I_H(\theta_H) = \left(\frac{\sin\Delta\sin(A-\theta_B-\theta_S)}{\sin(\theta_B-\theta_S)\sin(A+\Delta)}\right)^2 \frac{\sin(\theta_B-\theta_S-\Delta)}{\sin(\theta_B+\theta_S+\Delta)}. \qquad (65)$$

On either side of the total reflectivity domain, θ_H decreases on increasing y for all apex angles (cf. Eq.(63)), but for apex angles greater than a crossover value A_x, $\theta_H(y=1)$ becomes greater than $\theta_H(y=-1)$ where

$$A_x = \pi - \tan^{-1}\left(\frac{2\sin^2\theta_B}{\sin 2\theta_S} - \tan\theta_S\right). \qquad (66)$$

The two $I_H(\theta)$ peaks are separated by a forbidden gap corresponding to the full reflectivity domain ($-1<y<1$) and slowly tail to zero on opposite sides (cf. Fig.28). Figs.29-31 depict the important and relevant quantities for the design of Bragg prism viz., variations of neutron exit angles with incidence angle (left) and prism diffraction intensity $I_H(\theta_H)$ (right) for three different apex angles, each with $\theta_S=50.1^o$ and 5.26 Å neutrons incidence. For A equal to 160^o ($<A_x=166.85^o$), the two

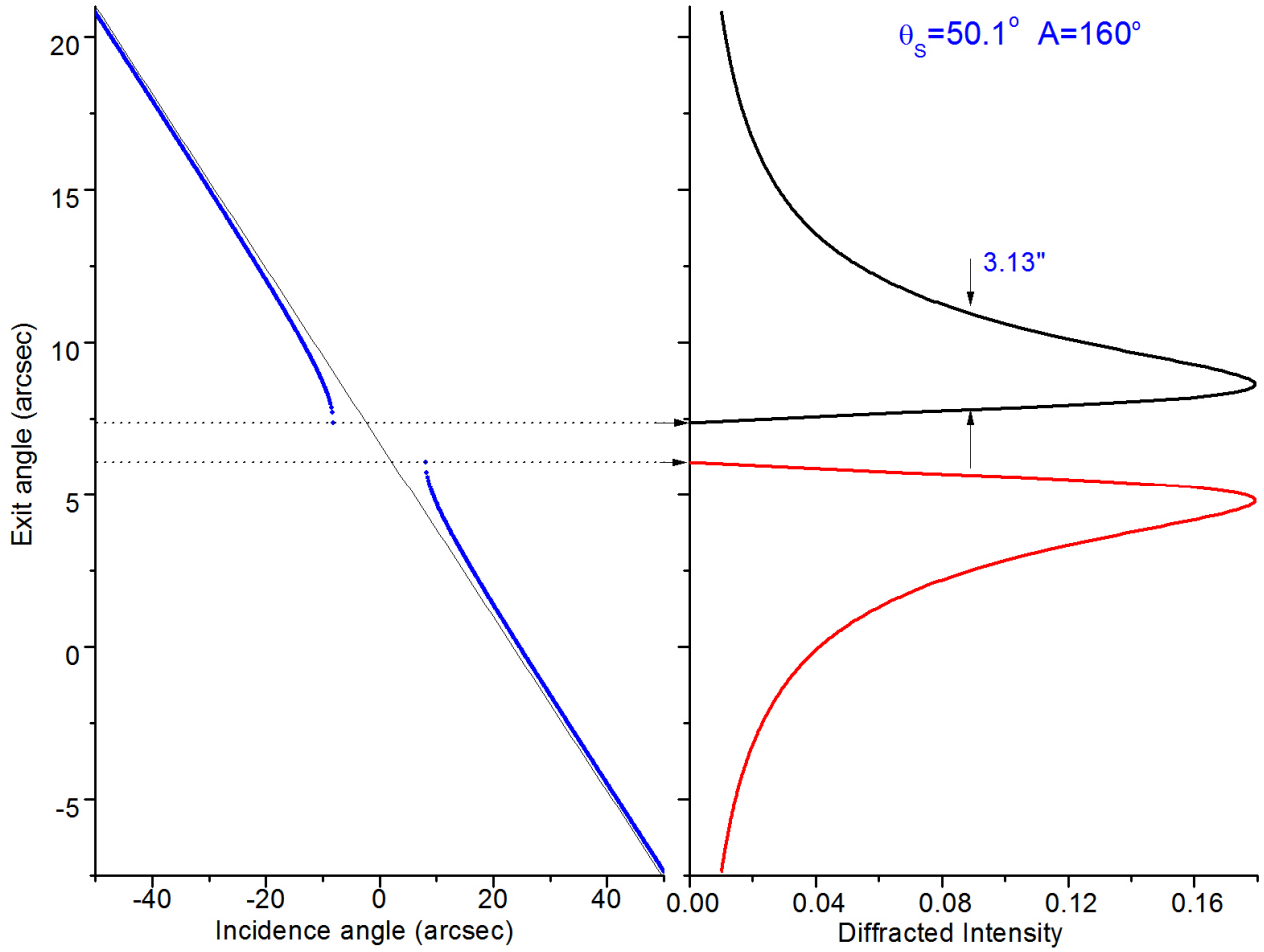

Fig.29 Exit angle as a function of incidence angle and Diffracted intensity for the Bragg prism monochromator with $A=160^o$ and $\theta_S=50.1^o$. For $A<A_x$, neutron exit angles corresponding to incidence angles on the two sides of the Bragg reflection do not overlap yielding two separated peaks.

$I_H(\theta_H)$ peaks of 0.18 height and 3.13 arcsec FWHM each separated by a 1.29 arcsec forbidden gap, tail off back to back (Fig.29). The compression factor limit is 3.52 for this Bragg prism. At A $=A_x$, exit angles of neutrons corresponding to incidence angles on the two sides of the Bragg reflection become exactly equal (i.e., $\theta_H(y=1) = \theta_H(y=-1)$) and forbidden gap just gets closed

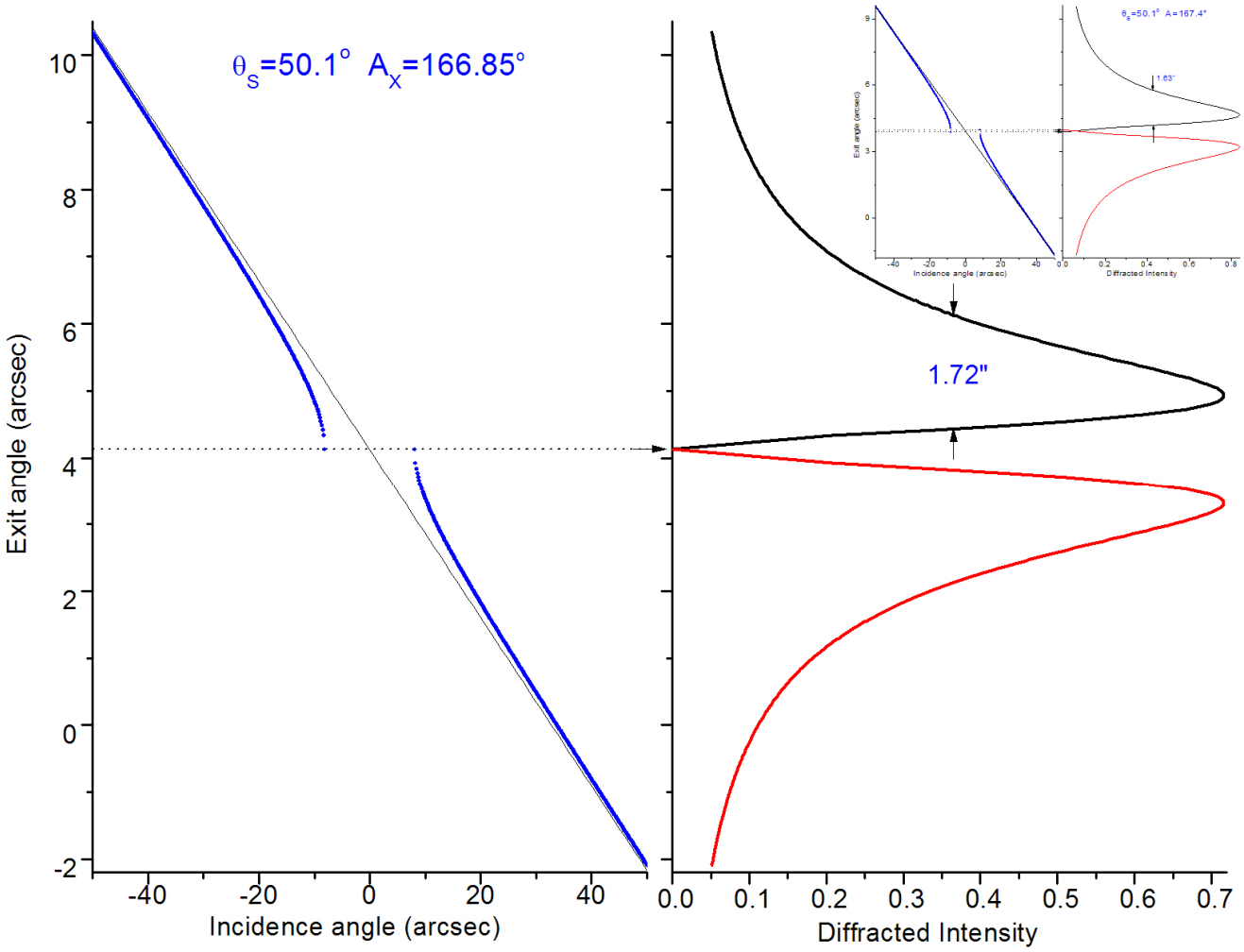

Fig.30 Exit angle as a function of incidence angle and Diffracted intensity for Bragg prism monochromator (A_x =166.85° and θ_S=50.1°). For A=A_x, exit angles of neutrons corresponding to incidence angles on the two sides of the Bragg reflection become exactly equal and peaks begin to overlap for A even slightly greater (e.g., A =167.4) than A_x (inset).

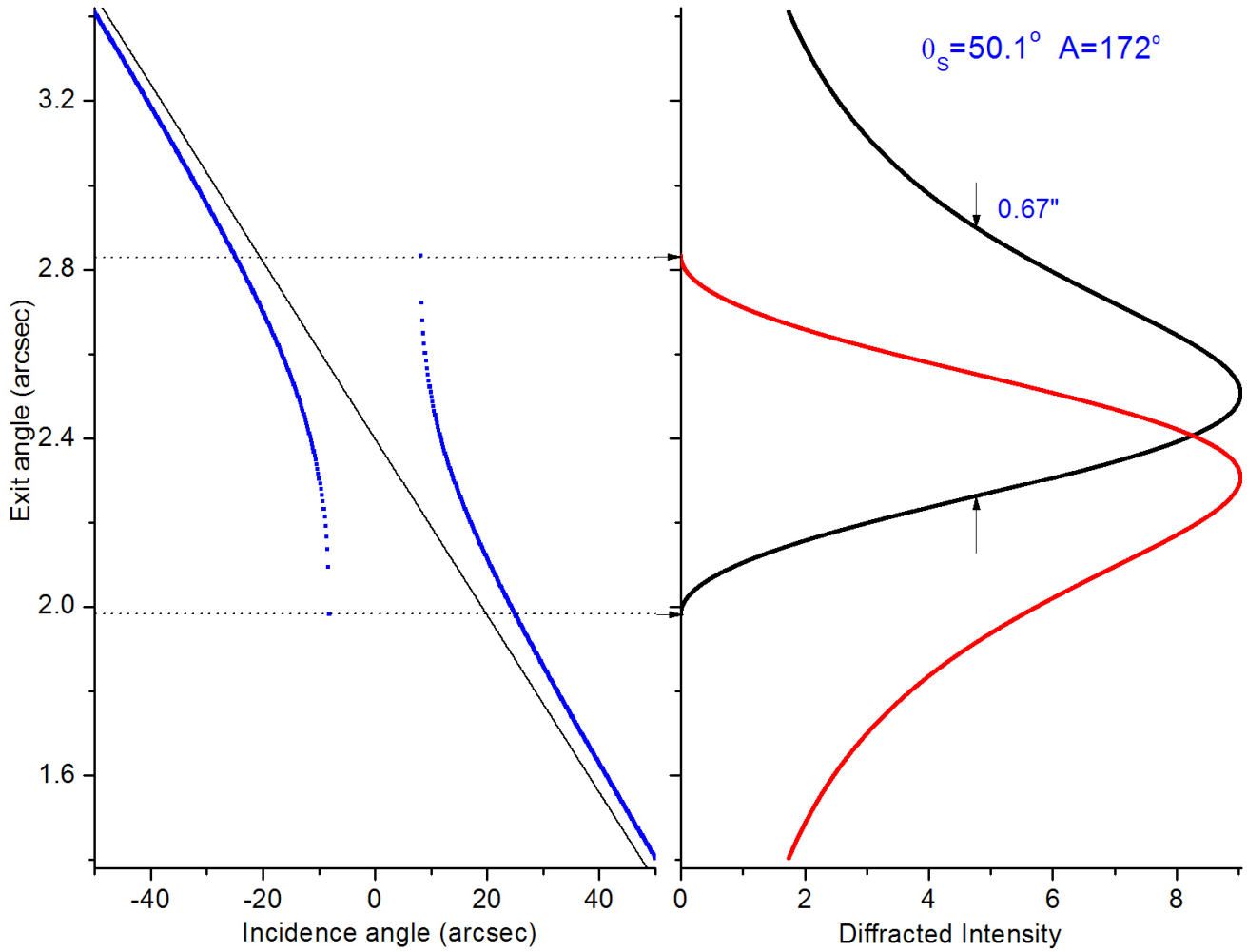

Fig.31 Exit angle as a function of incidence angle and Diffracted intensity for the optimised Bragg prism monochromator (A=172^o and θ_S=50.1^o). At this A, exit angles of neutrons corresponding to incidence on the two sides of the Bragg reflection significantly overlap to yield a single peak with long tails.

(Fig.30), reaching a compression factor limit of 7.95 and for A >A_x, $I_H(\theta_H)$ peaks start overlapping each other. At A equal to 167.4^o (slightly greater than A_x), the two peaks marginally cross each other as shown in inset of Fig.30. With A=172^o however, there is no forbidden gap since $\theta_H(y=1)>\theta_H(y=-1)$. The two peaks of 9.02 height and 0.67 arcsec FWHM each tail towards each

other with a compression factor limit of 47.62 (Fig.31) adding up to a single large peak. Thus by increasing A, we achieve stronger and narrower diffraction peaks due to better compression and hence superior collimation.

By a judicious optimisation of the Bragg reflection, the asymmetry of the Bragg configuration and apex angle A, the angular profile of the diffracted beam emerging from the side face can be narrowed down to the sub-arcsec domain. For 5.26 Å neutrons and Si {111} reflection, the optimal monochromator with A=172^o and θ_S=50.1^o yields vide Eq.(65) a pair of diffraction peaks each of 9.9 arcsec FWHM in incidence angle which get compressed to 0.67 arcsec FWHM in exit angle (Fig.32). Thus the variation in the compression factor from 0 at |y|=1 to 47.62 at |y|>>1 results in

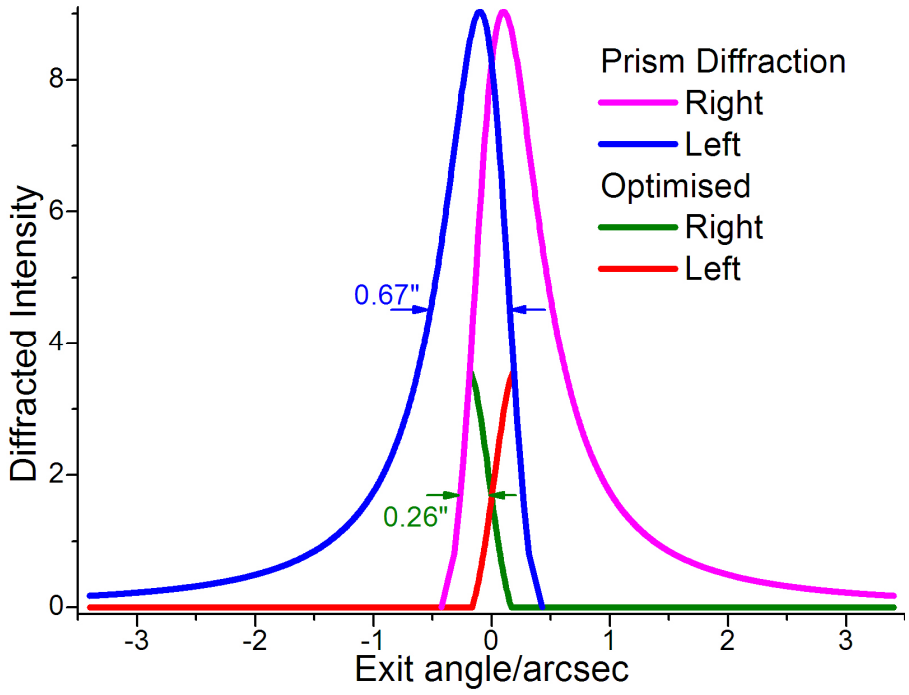

Fig.32 Exit angular profiles of prism diffraction (theory) for parameters as in Fig.28. Long tails of the large curves obtainable with the Bragg prism get clipped (small curves) on cutting the prism side face along the diffracted beam direction beyond a depth of 5 mm.

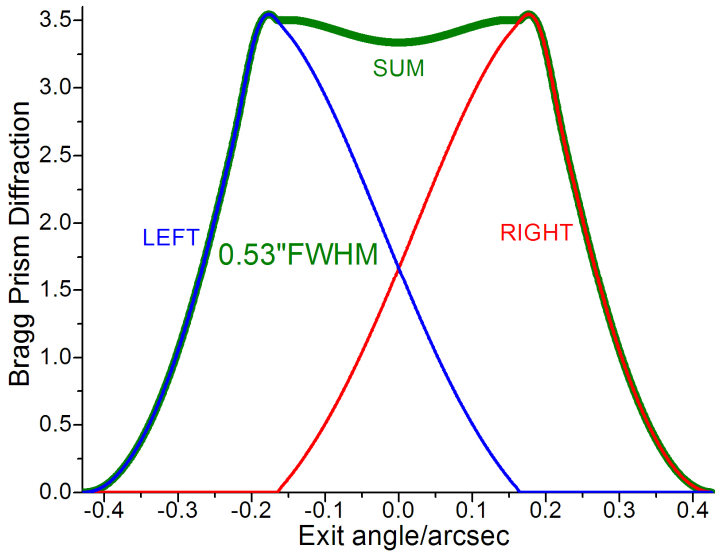

Fig.33 Theoretical flat-topped angular profile of the optimally tailored Bragg prism monochromator (A=172^{o} and θ_S=50.1^{o}). The angular width at zero intensity of the net peak is ($\theta_H|_{y=1} - \theta_H|_{y=-1}$)=0.86 arcsec.

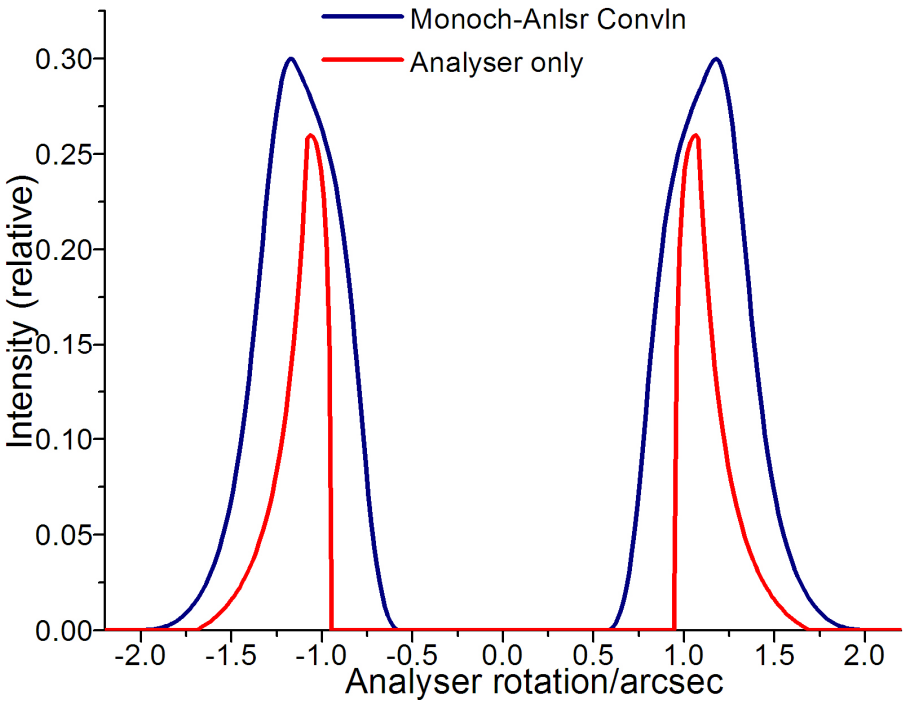

Fig.34 Numerically computed acceptance curve of the optimal Bragg prism analyser (A=16^{o} and θ_S=−51^{o}) for 5.26 Å neutrons (theory) and its convolution with the monochromator angular profile of Fig.33.

an overall compression factor of 14.78 for each peak. Each of these $I_H(\theta_H)$ peaks drops to zero intensity at |y|=1 incidence due to the onset of total reflectivity regime and tails towards the other peak. The tails can be clipped by cutting the side face of the prism parallel to the I_H beam direction, beyond a preset depth (cf. Fig.26). Neutrons incident at large |y| and propagating at large enough angles Δ reach this specially cut part of the side face, with an effective apex angle $A'=\theta_B+\theta_S$, which forbids them from exiting into the I_H beam. This side-face cut approach proposed in [138], has been employed extensively over the past two decades by experimenters in Vienna, Berlin, Mumbai and ILL (cf., [111-112]) to attain Bonse-Hart angular profiles free of I_H beam contamination. Each $I_H(\theta_H)$ peak thus drops to zero intensity for incidence beyond $\pm y_C$, say, as well. The critical incidence angles $-y_C$, y_C and the corresponding exit angles θ_{H1} and θ_{H2} beyond which the I_H peak becomes zero are geometrically determined by the distance of closest neutron incidence from the apex. By locating the incident beam optimally between 9 and 32 mm from the prism apex and applying the special cut to the side face beyond a depth of 5 mm from the incidence face, we attain $\theta_{H1}<\theta_H|_{y=1}$ and $\theta_{H2}>\theta_H|_{y=-1}$. The net peak made up of a smaller peak pair of 0.26 arcsec FWHM each (Fig.32) dropping to zero intensity on either side is hence contained completely within the full width at bottom equal to $(\theta_H|_{y=1} - \theta_H|_{y=-1})$. The configuration has been optimised to make these two peaks add to a tail-free and nearly flat-topped single peak of 0.53 arcsec FWHM (Fig.33) dropping to zero intensity at angular deviations from the centre greater than 0.43 arcsec on either side.

Similarly, a Bragg prism analyser configuration of opposite asymmetry with the optimum angles $A=16^o$ and $\theta_S=-51^o$, the $\theta_B+\theta_S$ cut made at depths beyond 8.3 mm and beam incidence between 34 and 67 mm from the prism apex, is expected to accept two 0.22 arcsec wide neutron peaks separated by 2.13 arcsec (Fig.34). The convolution of the monochromator peak with this analyser acceptance curve, constituting a pair of peaks with an FWHM of 0.57 arcsec each, separated by

2.35 arcsec, is also displayed in Fig.34. Fig.35 depicts our SUSANS experimental setup incorporating this optimised Bragg prism monochromator-analyser pair [146-149].

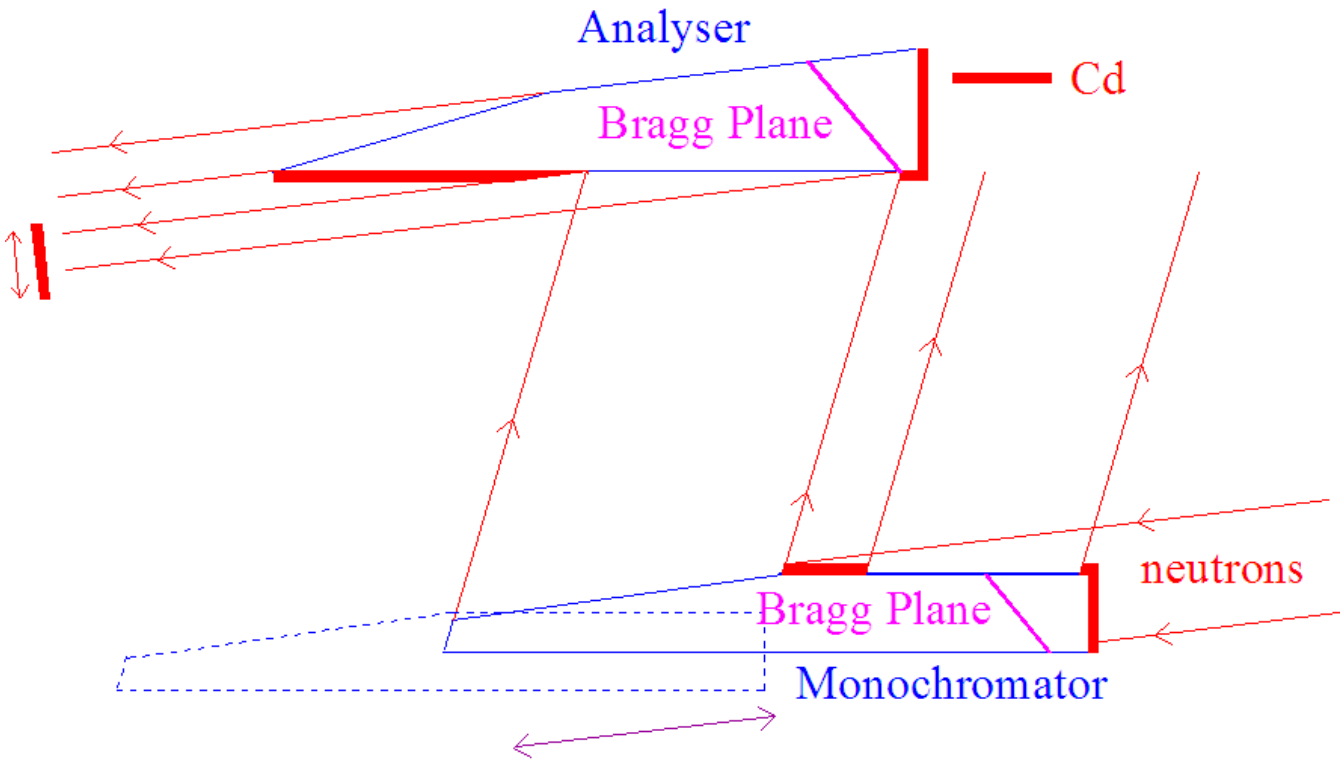

Fig.35 SUSANS experimental arrangement of the optimised monochromator-analyser pair of Si {111} Bragg prisms. A translation of the monochromator chooses between its Bragg reflection and prism diffraction to illuminate the analyser. Cd sheet downstream of the analyser can be translated to allow or forbid the analyser Bragg reflection into the detector (not shown).

4.3 Experimental

4.3.1 Bragg prism preparation

Several Bragg prism monochromators with θ_S close to 50^o and one analyser with $\theta_S = -51^o$ were fabricated with the apex angle A of 172^o (Fig.36) at Centre for Design and Manufacture (CDM), Bhabha Atomic Research Centre (BARC), Mumbai, India. The {111} planar direction in a <100> dislocation free, single crystal Si ingot was located using {220} and {111} reflections of 1.2 Å neutrons at the Triple Axis Spectrometer (TAS) in the Dhruva reactor, Mumbai-India and marked on the ingot with a diamond point. Precision cuts were made at the required θ_S to {111} on a Blohm precision grinding machine with a wobble-free diamond wheel of 350 mm diameter and 1.5 mm thickness to obtain several 9 mm thick monochromator slices and one 13.1 mm thick analyser slice. A cut at $A=172^o$ was made on the incidence face of each monochromator at 33 mm from the incidence edge. The side face was then cut along $\theta_B+\theta_S$ to the incidence face beyond a depth of 5 mm from the incidence face. Similar cuts were made to the analyser slice at the desired angles and depth. The Bragg prisms were then polished and ground to within 1 μm uniformity using another smaller 35 mm thick diamond wheel. The polished prisms were cleaned ultrasonically with water, methanol, acetone and trichloroethylene. They were subsequently subjected to a slow etch in a mixture of hydrofluoric acid (HF) and nitric acid (HNO_3) in ratio of 1:20 for 20 minutes to remove about 20 μm of each prism surface and purge all residual surface strain and damage introduced during the cutting and polishing stages. Final sub-μm polishing and slow etching operations were performed at the Chemical Laboratory of Helmholtz Zentrum Berlin (HZB) in Germany.

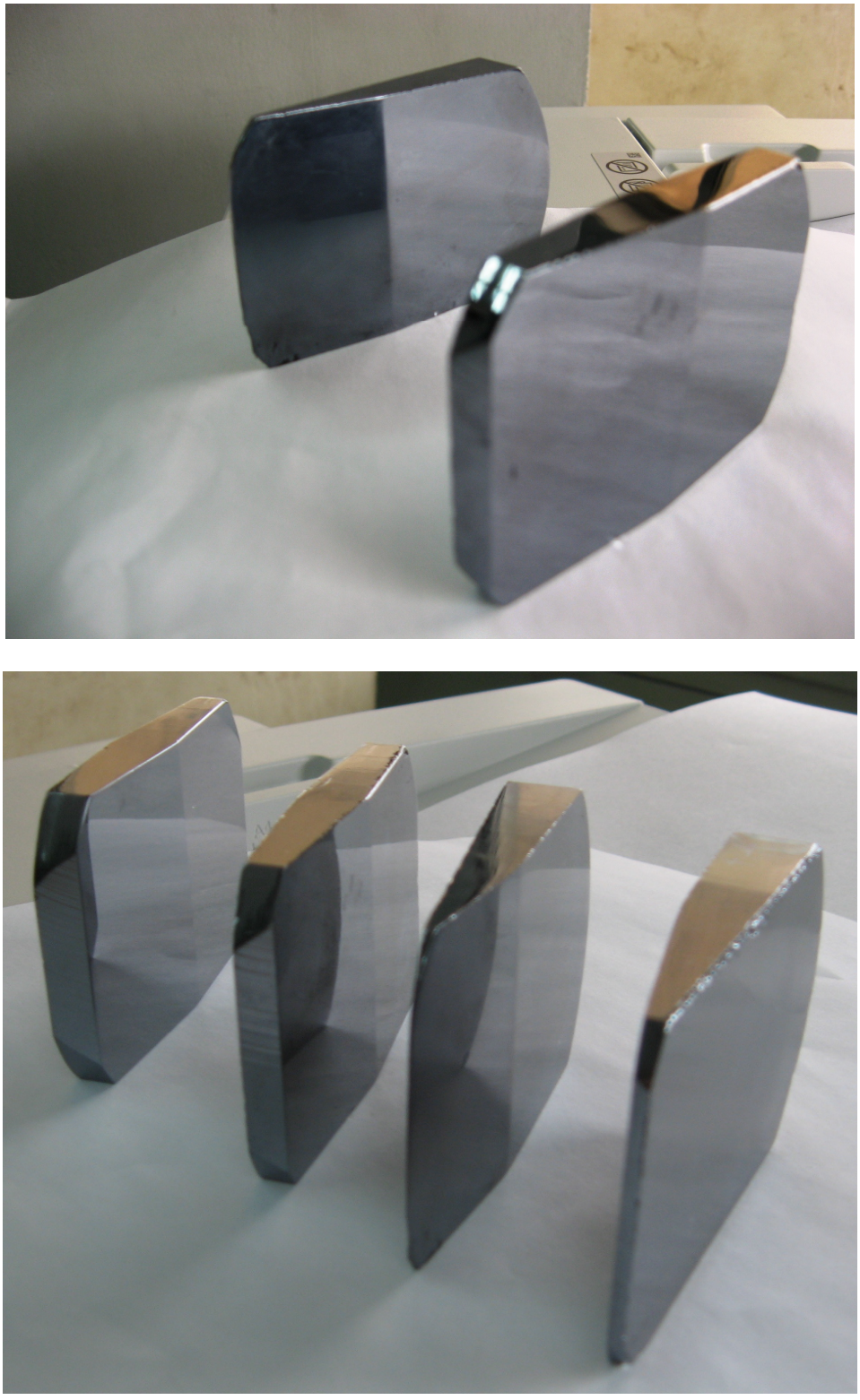

Fig.36 Photographs of Bragg prisms. Top: Monochromator-analyser setup. Bottom: Three monochromators and one analyser (3rd from the left).

4.3.2 Experiment

The experiment was carried out at the V12b Double Crystal Diffractometer setup of BER II 10 MW Reactor in HZB, Germany. The analyser rotation could be adjusted in two stages; first in 1 arcsec steps with a geared step motor and then with a piezocrystal driven stage, with the smallest step size of 0.156 arcsec. The analyser tilt could be set to within 0.9 arcsec. The monochromator (Fig.35), covered strategically with Cd sheets, could be translated along the incident beam direction to direct either its Bragg reflection or prism diffraction towards the analyser. A Cd sheet could be translated in front of the He^3 detector to cut off the Bragg reflection from the analyser.

4.3.3 1st ever sub-arcsec collimation

An asymmetric monochromator (θ_S=53.5^o) was placed in the 5.26 Å neutron beam from the PG pre-monochromator and its rotation and tilt angles adjusted to maximise its Bragg reflection. The analyser was illuminated with this Bragg reflection and aligned using its prism diffraction. The analyser tilt had to be set to within 9 arcsec. The analyser rocking curve comprised a well resolved pair of ~1.7 arcsec wide peaks (circles) (Fig.37). The theoretical convolution (smooth curve) of monochromator Bragg reflection and analyser acceptance is also plotted for comparison. The experimental curve reproduces the theoretical peak widths [150-151] fairly well vindicating the analyser Bragg prism performance. The flat tops of the theoretical peaks however have got rounded off in the observed spectrum. The relative intensities of the two peaks do vary statistically from spectrum to spectrum, but more often than not, the higher-angle peak is weaker. The reason for this left-right asymmetry in Figs.37, 40-42 is not clear.

A Bragg prism monochromator with θ_S=50.1^o was next tested. Its direct Bragg reflection, being much stronger and wider than prism diffraction, was first used, facilitating a quick and easy

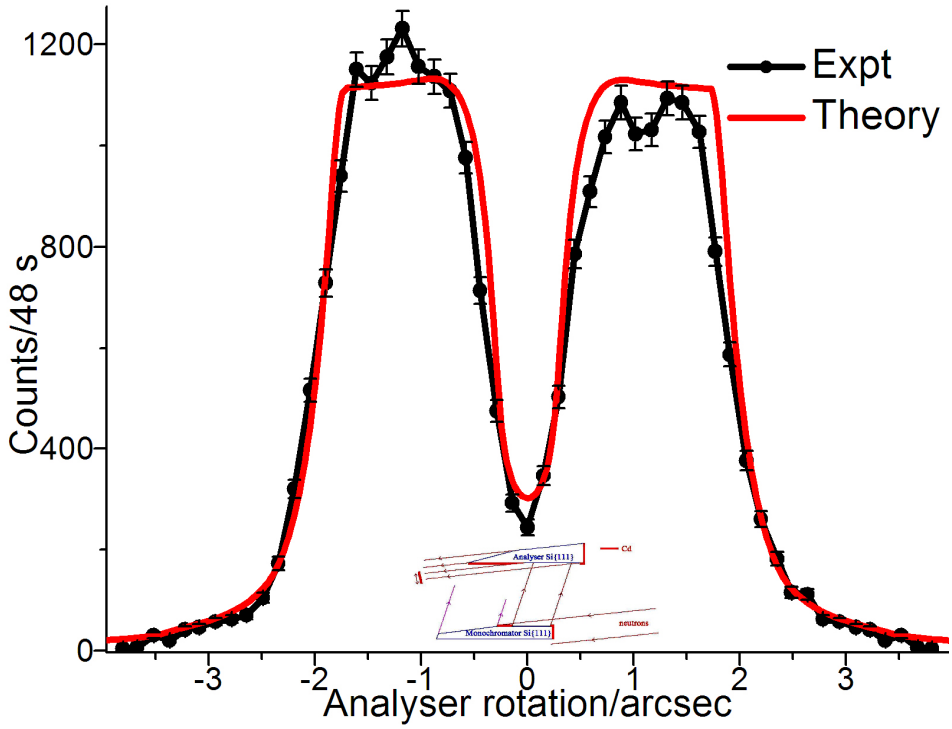

Fig.37 Bragg reflection from the θ_S=53.5^o monochromator observed with prism diffraction (cf. inset) of the optimal analyser.

alignment of the analyser whose Bragg reflection as well as prism diffraction were monitored (Fig.38). The analyser rocking curve yielded the expected ~ 3.1 arcsec wide peak (circles) with a peak intensity of about 468 neutrons/s. The monochromator was then translated to illuminate the analyser with its prism diffraction alone. The corresponding analyser rocking curve of ~ 2.5 arcsec FWHM (cf. Fig.39) agrees well with theory (smooth blue curve), displaying a peak intensity of 68.5 neutrons/s, After optimising the analyser alignment, the Cd sheet before the detector was translated to stop Bragg reflected neutrons from the analyser. With these Bragg prism diffractions, the analyser tilt adjustment became even more critical and had to be made in 0.9 arcsec steps, since prism diffraction peaks are narrower and sharper than the Bragg reflections. The rocking curve (Fig.40) consisting of a pair of 0.62 arcsec wide peaks separated by 2.2 arcsec (squares), is in fair

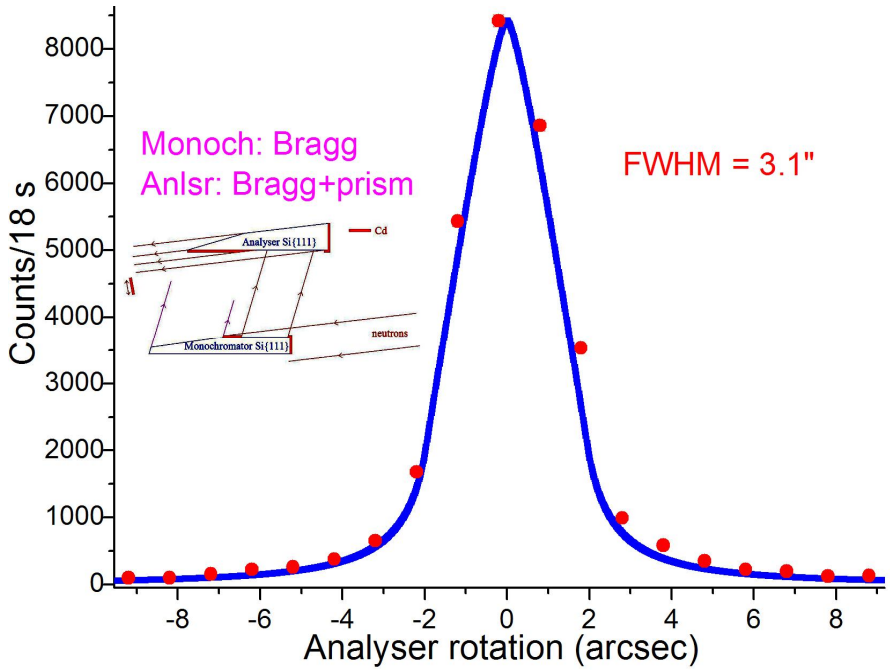

Fig.38 Bragg reflection rocking curve of the monochromator (A=172^o and θ_S=50.1^o) observed with Bragg reflection and prism diffraction (cf. inset) of the optimal analyser.

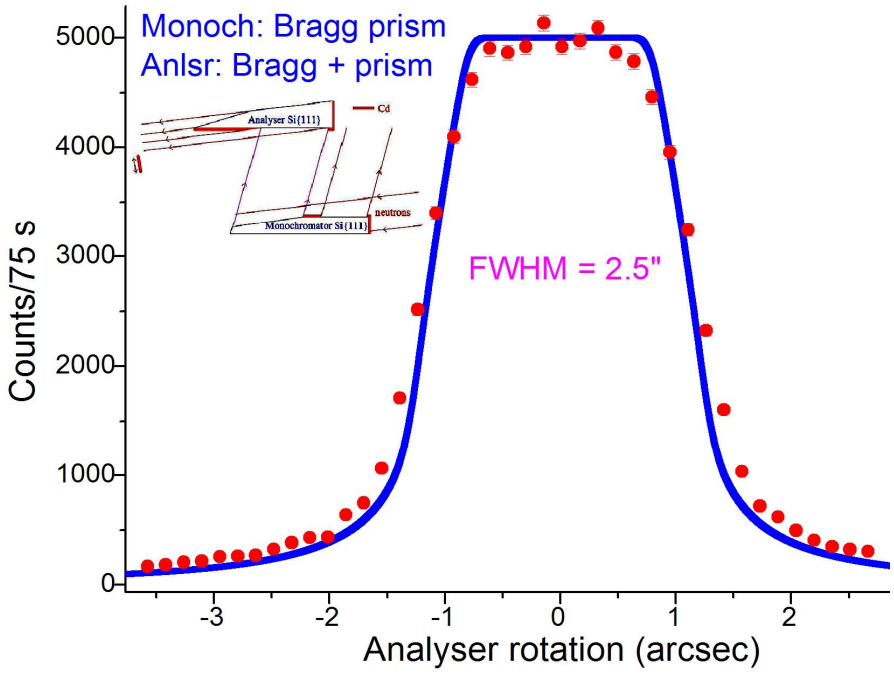

Fig.39 Bragg Prism diffraction rocking curve of monochromator (A=172^o and θ_S=50.1^o) observed with Bragg reflection and prism diffraction (cf. inset) of the optimal analyser.

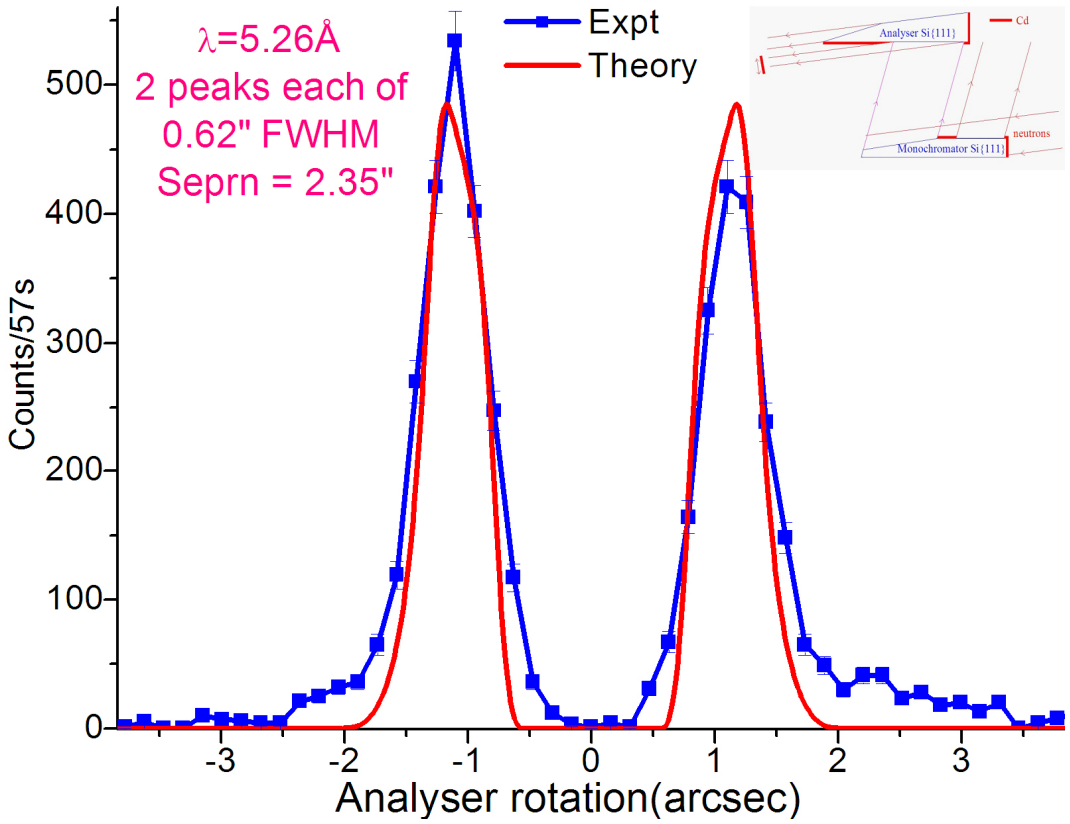

Fig.40 1st sub-arcsec neutron collimation: observed (data points) and calculated (curve) rocking curves (cf. inset) for prism diffractions of the monochromator (A=172° and θ_S=50.1°) and the optimal analyser.

agreement with the theoretical prediction (smooth curve), with a peak of ~ 10.1 neutrons/s. This is the best instrumental resolution recorded to date. The monochromator prism diffraction peaks are about 4 times as narrow as the monochromator Bragg reflection rocking curve, both being recorded by the analyser prism diffraction, albeit having 6.5 times as weak peak intensity. In comparison with the Bragg-Bragg curve on the other hand, they are 5 times as narrow, but with about 46.3 times as weak peak intensity. The deconvolution of the observed rocking curve from the analyser acceptance curve yields an FWHM ~ 0.58 arcsec for the beam delivered by the monochromator. This constitutes the tightest neutron collimation attained to date [152].

4.4 Applications of novel SUSANS setup

4.4.1 Super Ultra small angle neutron scattering (SUSANS) of a protein sample

With this highly collimated, nearly plane-wave neutron beam, we recorded the first SUSANS spectrum in the wave vector transfer Q ~ 10^{-6} $Å^{-1}$ regime with a hydroxyapatite casein protein sample placed between the monochromator and analyser. The virgin rocking curve that consists of a pair of 0.62 arcsec wide peaks separated by 2.2 arcsec constitutes the instrumental resolution. This is basically the convolution of the monochromator peak with the analyser acceptance curve riding on an unavoidable background. The bottom axis in Fig.41 labelled as Q ($Å^{-1}$) is derived from the analyser Bragg prism rotation θ and neutron wave number k_O through relation $Q = 2k_O\sin(\theta/2)$. The corresponding instrumental resolution of about $3.4x10^{-6}$ $Å^{-1}$ for this novel instrument is

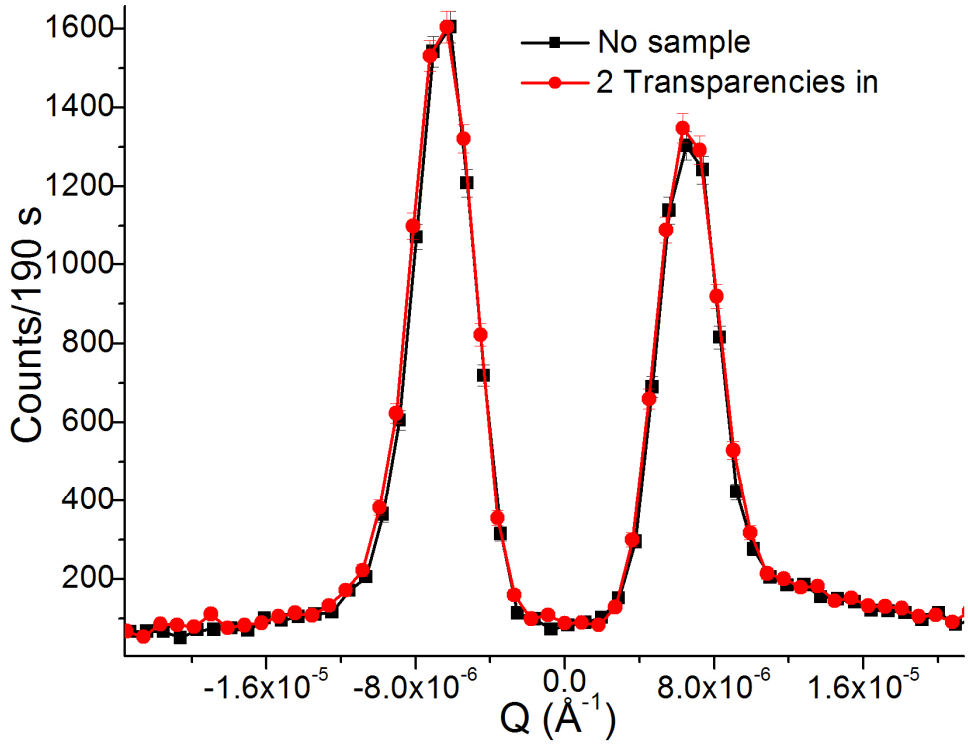

Fig.41 SUSANS spectra without and with a sample holder, viz. a pair of overhead projection transparencies.

superior by a factor of about 6 to the Q-resolution of $2x10^{-5}Å^{-1}$ possible at the next best USANS facility on S18 beamport of ILL (France). The Q-resolution is inversely proportional to the spatial extent of agglomerates that can be probed by the instrument. The hydroxyapatite casein protein sample was placed between a pair of transparencies used for overhead projection. To ascertain the small angle scattering contribution from the transparencies, a SUSANS spectrum was recorded (Fig.41) with the transparencies as the sample. Within the experimental error, the transparencies left the instrument rocking curve essentially unaltered over the Q-domain of interest. This enabled us to ignore the scattering from transparencies during the final data analysis. Analyser rocking curves were recorded without and with the protein sample placed in the holder (Fig.42). The observed broadening of the SUSANS spectrum by the protein sample in the 10^{-6} - 10^{-5} $Å^{-1}$ region yielded information on the size distribution of agglomerates in the sample (Fig.43).

SUSANS data analysis

The intensity of neutrons scattered through a small wave vector transfer of magnitude Q from spherical agglomerates in a homogeneous sample can be expressed as

$$I(Q) = C[\rho_s - \rho_a]^2 \int N_o[V(R)]^2 \left|F(QR)\right|^2 D(R)dR\,, \qquad (67)$$

where C denotes a constant, N_o signifies the number of scattering objects in the sample, V(R) stands for the volume of the scattering object of radius R and ρ_s and ρ_a symbolise scattering densities of the scattering sample and the surrounding ambient matrix respectively. The form factor F(QR) is the Fourier transform of the spatial distribution of the scattering sphere, viz.

$$F(QR) = \frac{3\{\sin(QR) - QR\cos(QR)\}}{Q^3R^3}. \qquad (68)$$

We assumed a log-normal distribution function D(R) of spherical agglomerates with radii R in the

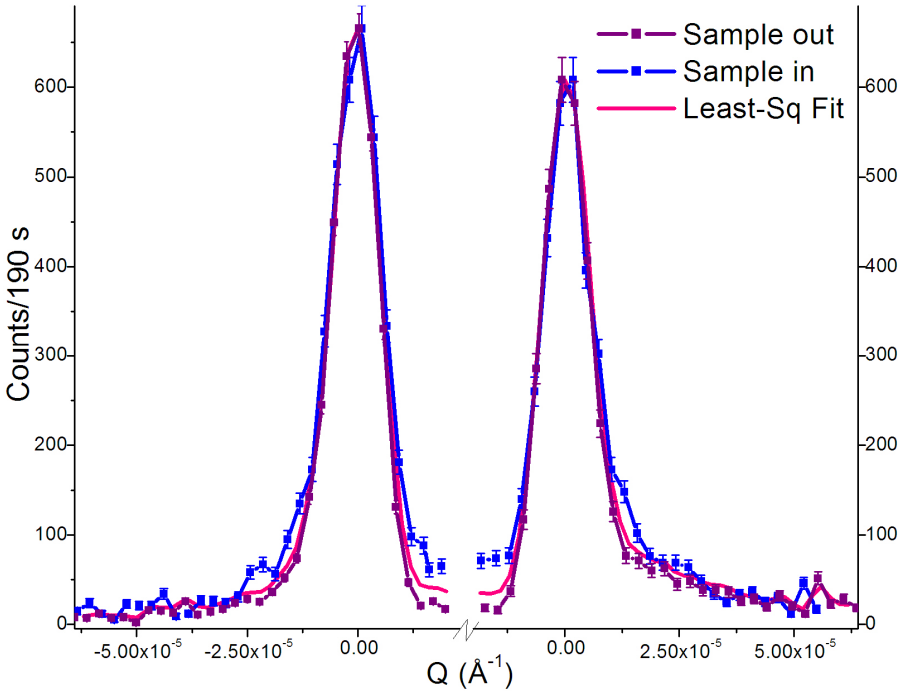

Fig.42 First Q ~ 10^{-6} Å^{-1} SUSANS spectra without and with a Hydroxyapatite casein sample. Least-squares fit to the sample spectrum (smooth curve) implies the instrument capability of characterising ~ 150 μm-size agglomerates in a sample.

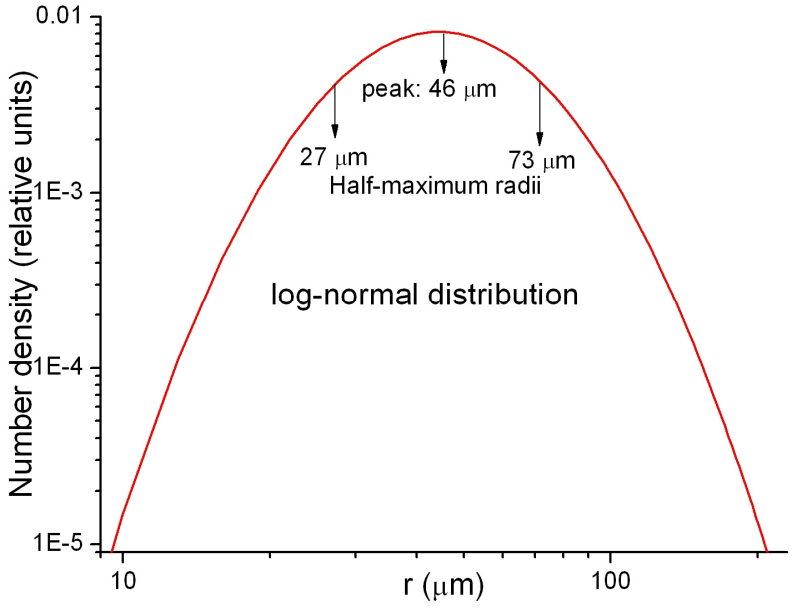

Fig.43 Sphere size distribution inferred from Fig.42.

sample, i.e.,

$$D(R) = \frac{1}{R\sigma\sqrt{2\pi}} e^{-\{\ln(\frac{R}{R_m})/\sigma\sqrt{2}\}^2} . \quad (69)$$

Here, R_m and σ denote the median radius and dimensionless standard deviation of the distribution, respectively. Substituting Eqs. (68) and (69) in Eq. (67), we express the scattered intensity as

$$I(Q) \alpha \int_0^\infty R^6 |F(QR)|^2 D(R) dR . \quad (70)$$

The rocking curve recorded with the sample is then least-square fitted to the convolution of I(Q) with the instrument resolution curve, viz. the rocking curve observed without the sample, i.e.

$$I_S(Q) = I_{nS}(Q) \otimes I(Q). \quad (71)$$

The log-normal size distribution of spherical agglomerates in the sample inferred [153] from the least-squares fit is characterised by R_m of 53 μm and σ = 0.38 respectively. This distribution peaks at 46 μm, dropping to Half Maximum at 27 and 73 μm respectively. The greater half-maximum of this distribution corresponds to the instrument capability of characterising agglomerates up to 150 μm in size.

4.4.2 Coherence properties of the beam

Coherence properties of the amplitude of a beam are described by the coherence function [1,51]

$$\Gamma^{(1)}(\boldsymbol{\Delta}) \cong \int g(\mathbf{k}) e^{i\mathbf{k}.\boldsymbol{\Delta}} d\mathbf{k} , \quad (72)$$

viz. the Fourier transform of the wave vector (momentum) distribution g(**k**) of the beam. For Gaussian wave vector distributions having widths δk_i in each of the three orthogonal directions (i=x,y,z), a Gaussian coherence function of the form

$$\Gamma^{(1)}(\Delta) = \prod_{i=x,y,z} e^{-(\delta k_i . \Delta_i)^2/2}, \quad (73)$$

is obtained. In this case, the wave vector distribution and coherence length Δ_i are related by Heisenberg uncertainty relation [95],

$$\delta k_i \Delta_i = 1/2. \quad (74)$$

Diffraction from a macroscopic grating

Diffraction of neutrons of wavelength λ for near normal incidence at a grating of period $d >> \lambda$ gives rise to a pattern with an angular separation ~ λ/d between successive intensity maxima. With a grating period of even a few microns, scattering angles become as small as a few arcsec for thermal and cold neutrons. A collimation of the incident neutron beam to within ~ arcsec is therefore necessary to record a well resolved diffraction pattern. Our super collimated beam facilitated measurement of the diffraction pattern from a large-period grating and determination therefrom of the transverse coherence length of the beam.

A grating of ~ 200 μm period, made by winding a steel wire of 100 μm diameter tightly on a 50x50 mm^2 aluminium frame (inset of Fig.44), was mounted between the monochromator and analyser for near normal neutron incidence. SUSANS (Super Ultra-Small Angle Neutron Scattering) spectra recorded with and without the grating in the mount are depicted in Fig.47. The two peaks in the grating pattern are considerably broadened due to multiple scattering and refraction in the cylindrical wires, and modulated by clearly resolved diffraction oscillations corresponding to the grating period [154]. The average peak broadening on transmission through the steel wires in the grating was least-square fitted to a Gaussian angular profile of standard deviation equal to about 0.41 arcsec, by deconvoluting each peak from that in the no-grating SUSANS pattern. At a

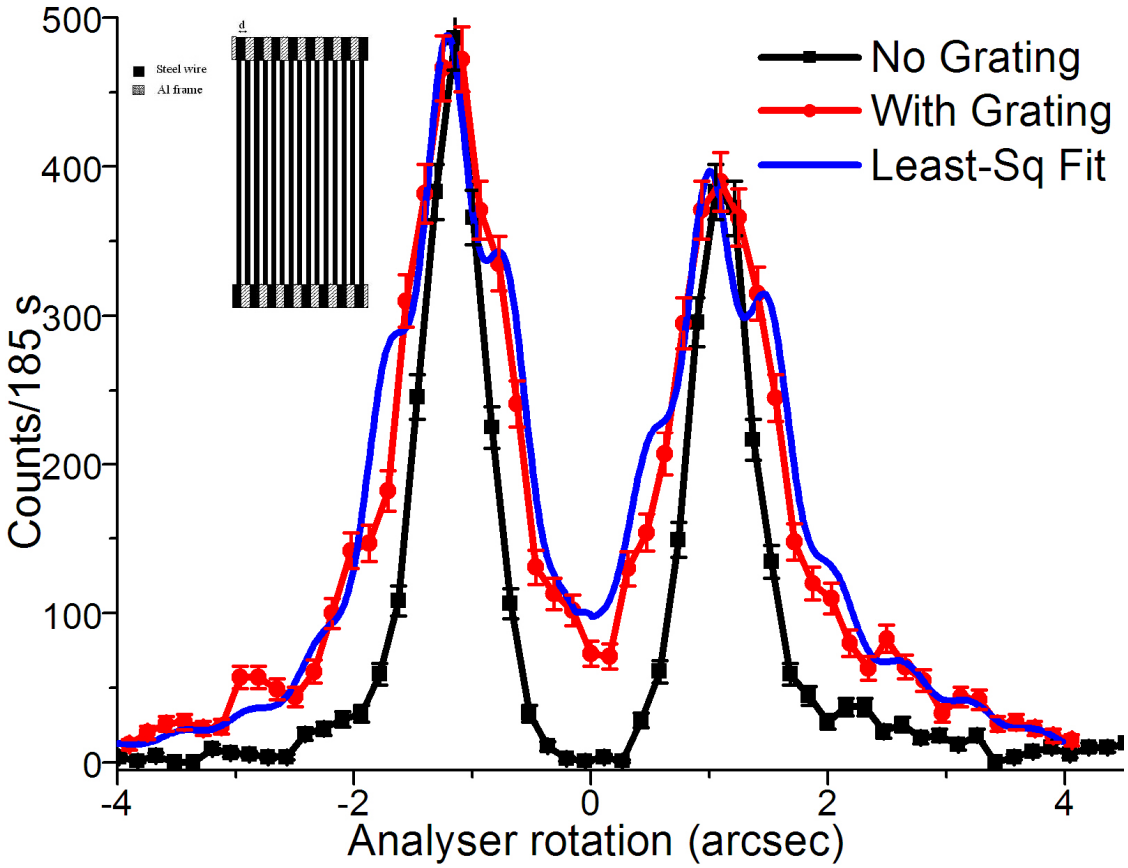

Fig.44 1st neutron diffraction pattern of a macroscopic grating (inset) of period d ~ 200 μm. The least-squares fit to the pattern (smooth curve) corresponds to a transverse coherence length of 175 μm, the highest value reported to date for Å wavelength neutrons.

scattering angle θ, partial neutron wave amplitudes diffracted from successive elements of the grating with concomitant phases add coherently to form a net complex amplitude

$$A(\theta) = \sum_{n=-\infty}^{\infty} e^{-\frac{(nd)^2}{2\sigma^2}} e^{i\left(\frac{2\pi nd}{\lambda}\sin\theta\right)} . \qquad (75)$$

Here n is a running index for the illuminated elements of the grating and $\sigma_\perp$ denotes the transverse coherence length for amplitudes of the incident neutron wave. The corresponding intensity is given by

$$I(\theta) = \left|A(\theta)\right|^2 . \tag{76}$$

The least squares fit (smooth curves in Fig.44) to the data, yields a transverse coherence length $\sigma_\perp$ equal to 74 μm for the monochromated neutron beam. The corresponding transverse coherence length for intensity equals 53 μm which is greater than $1/(2\sigma_{k\perp})$ = 35 μm expected for a Gaussian angular distribution with the observed FWHM of 0.58 arcsec. The corresponding FWHM transverse coherence length of 175 μm far exceeds the previous best value of 80 μm [112] obtained for a 1.4 arcsec wide beam as well as the highest (5 μm) achieved in neutron interferometry [1].

The peak broadening was also analysed by considering SUSANS from steel wires. The intensity of neutrons scattered through a small wave vector transfer of magnitude Q in a homogeneous sample is governed by Eq.(67) with the form factor term $|F(QR)|^2$ being replaced by $\int_0^{\pi/2} \left|F(QR,\alpha)\right|^2 \sin\alpha \, d\alpha$ where F(QR,α) is given by

$$F(QR,\alpha) = 2\frac{\sin(QL/2\cos\alpha)}{QL/2\cos\alpha}\frac{J_1(QR\sin\alpha)}{QR\sin\alpha}. \tag{77}$$

Here $J_1(x)$ is the first order Bessel functions of the first kind, L is length of cylindrical wire, α the angle between the scattering vector **Q** and wire axis, V_{cyl} the volume of the wire and R denotes the radius of the wire. In our experiment, the wires are vertical and **Q** lies in the horizontal plane. Hence α equals π/2 and

$$F(QR) = \frac{2J_1(QR)}{QR}. \tag{78}$$

We assumed a log- normal distribution in radii and a form factor given by Eq.(78) for steel wires. The least-squares fit to the broadened peaks vide Eq.(67) yielded a median radius of 54 μm with a standard deviation of 0.1, i.e. a peak radius of 53.5 μm and Half Maximum radii of 47.5 and 60 μm

respectively, for the grating wires. The least-squares fit (smooth curves in Fig.45) to the data with this broadening fit vide Eqs.(75-76) yielded the same transverse coherence length $\sigma_{\perp}$.

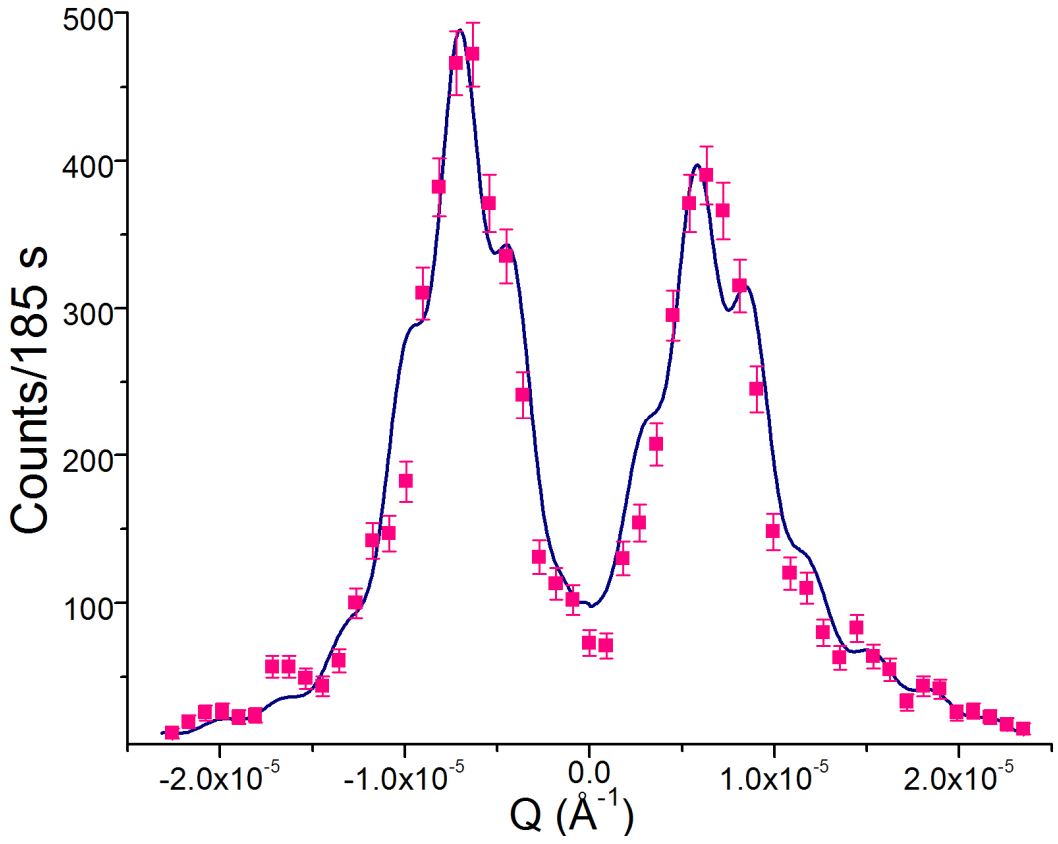

Fig.45 Neutron diffraction pattern (points) from a macroscopic grating of period d ~ 200 μm and the least-squares fit (smooth curve) to the pattern.

4.4.3 Versatility of the instrument

We also investigated the mesoscopic length scale with this novel instrument. The analyser rocking curve was recorded with and without a magnetic sample $Fe_{73}Al_5Ga_2P_8C_5B_4Si_3$ placed between the monochromator and analyser. Since the neutron beam was unpolarised, we could infer only the nuclear scattering length density distribution in the sample. Fig.46 depicts the fitted scattering length density distribution which extends upto a few μm.

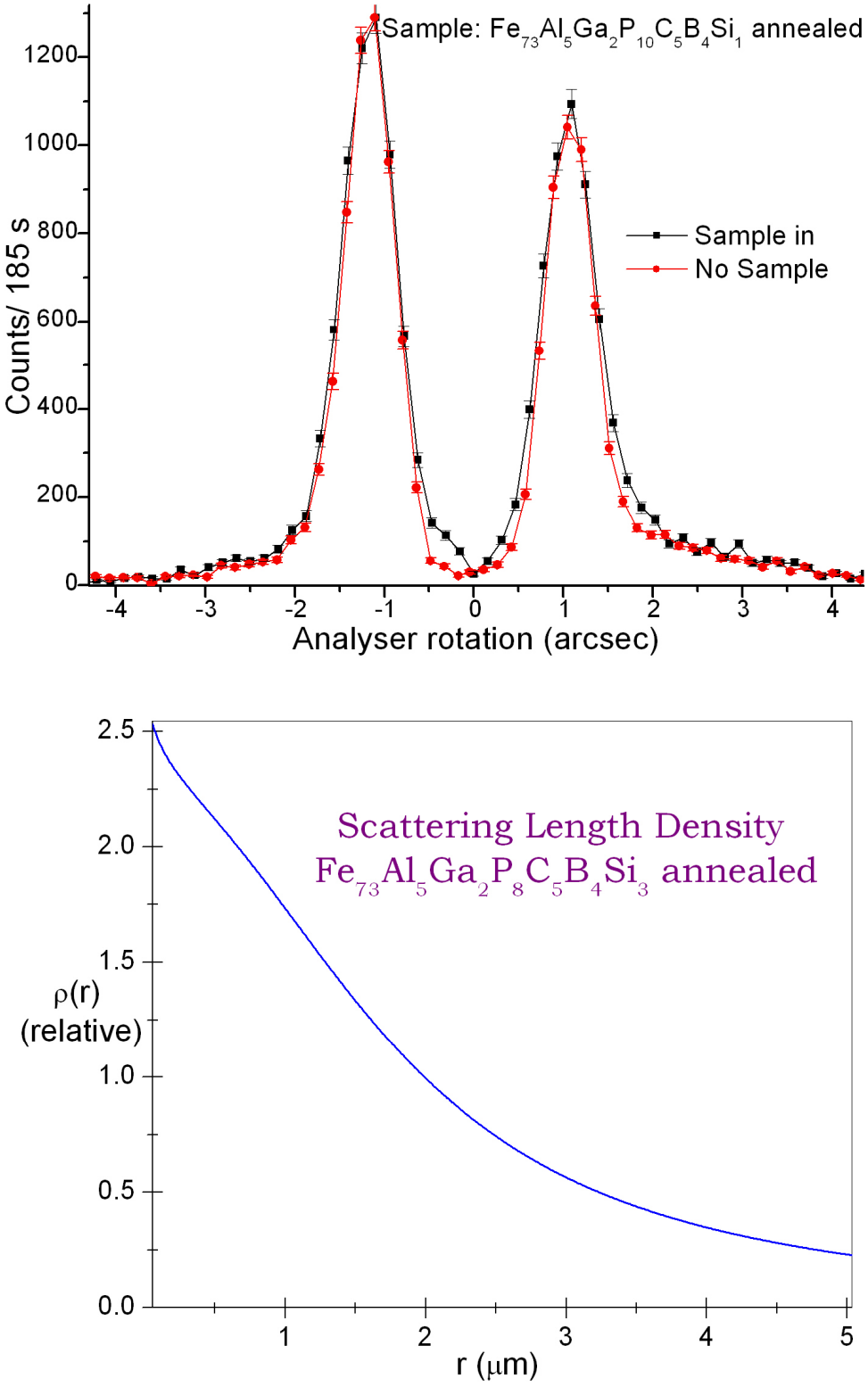

Fig.46 Analyser rocking curve for an iron sample (top) and inferred scattering length density distribution (bottom).

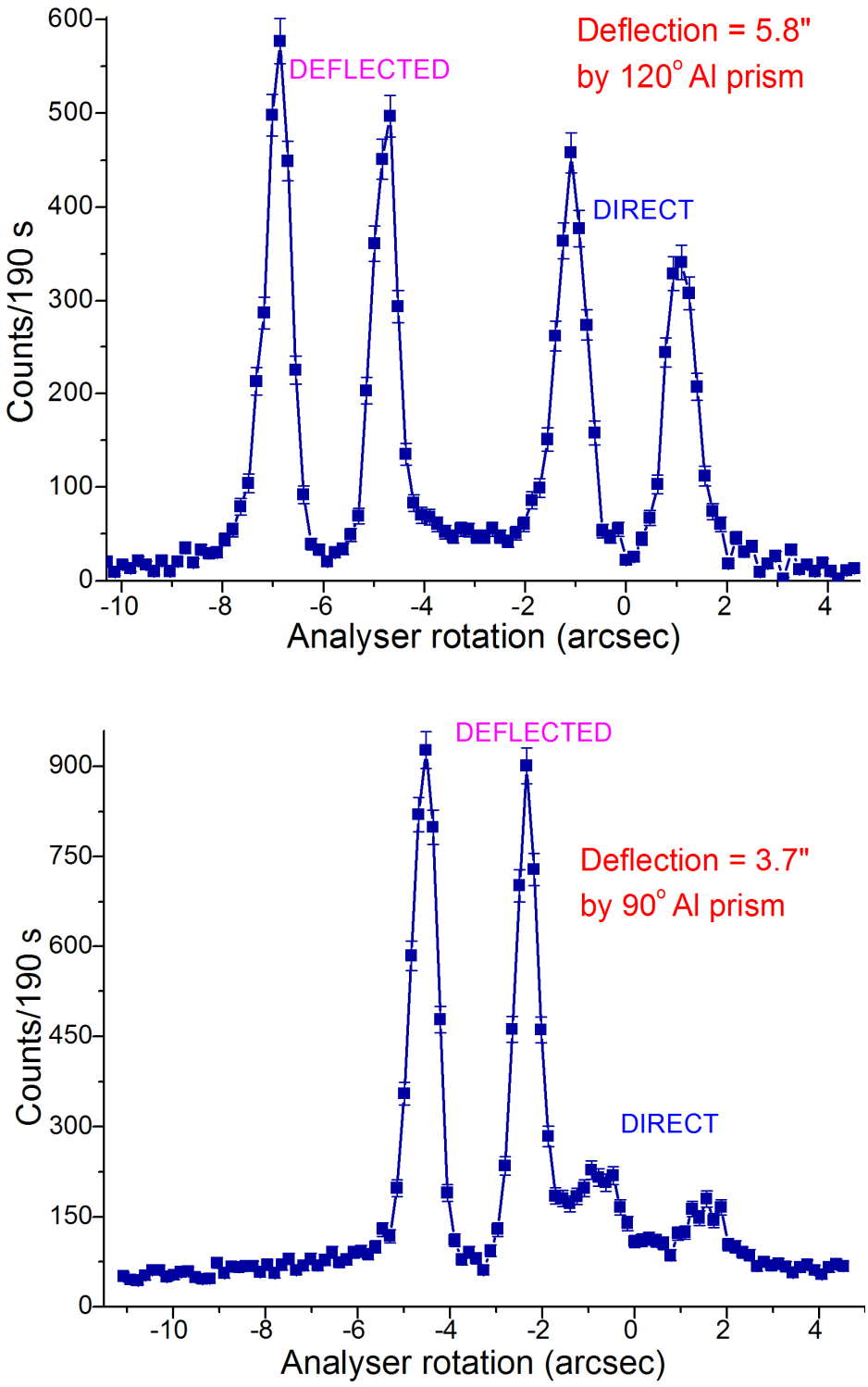

Fig.47 Analyser rocking curve for amorphous aluminium prisms of apex angles 120^{o} (top) and 90^{o} (bottom) to observe ~ arcsec deflections.

This instrument was also employed to observe arcsec neutron deflections from amorphous aluminium prisms of apex angles 120^o and 90^o. These prisms were placed between the monochromator and analyser. Only a part of the neutron beam illuminated the prism, the remaining beam reaching the analyser directly to serve as a reference for the prism deflection measurement. The direct and deflected neutron peaks were simultaneously recorded in each analyser scan. The analyser rocking curve recorded at a typical incidence angle for a Bragg prism is displayed in Fig.47. Least-squares Voigt function fits were made to the direct and deflected neutron peaks in the rocking curve. The neutron deflection was determined from the angular shift between the fitted peaks for the direct and deflected beams. The observed deflections for 120 deg and 90 deg prisms were determined to be 5.8 and 3.7 arcsec respectively [155].

This SUSANS setup thus can effectively probe length scales ranging from a few hundred nm to 150 μm. It is also capable of measuring ultra-small deflections ~ arcsec.

To put the things in proper perspective, Bragg reflections from single crystals yield angular widths of a few arcsec for thermal neutron beams with long tails. The Bonse-Hart proposal [115] of attaining a sharp and nearly rectangular profile by Bragg reflecting neutrons successively from a channel-cut single crystal was realised in its totality by Wagh et al [111]. They achieved the Darwin reflection curves ~ 5.7 arcsec for 5.23 Å neutrons. Treimer et al. [112] employed 7X7 bounces of a 5.4 Å neutron beam in the monochromator and analyser channel-cut crystals. A silicon prism suspended in each crystal without touching it, deflected the neutron beam between the third and fourth bounce by about 4 arcsec, thus misaligning the beam for the subsequent four bounces and yielding a 1.6 arcsec wide rocking curve. We now achieve the first ever sub-arcsec collimation of ~ 0.58 arcsec for a 5.26 Å neutron beam by introducing a novel Si{111}Bragg prism.

4.5 Tightening the neutron collimation still further

The tight collimation of neutrons increases their transverse coherence length to greater than 100 μm FWHM and hence forms a nearly plane wave of monochromatic neutrons. The neutron collimation may be tightened further by reducing the neutron wavelength. For instance, the same Bragg prism monochromator-analyser pair optimised for 5.26 Å neutrons can super collimate 1.75 Å neutrons using the {333} reflection in the same geometric configuration down further by a factor of 9. The {333} Si Debye Waller factor is less than that for {111}, since $DW = \exp\left(-(B+\Delta B)\left(\sin\theta_B/\lambda\right)^2\right)$ with parameters B=0.422Å^2, ΔB=0.028Å^2 at 293 K [157]. The corresponding reduction in F_H should improve the collimation further. With an optimised 1.75 Å neutron incidence between 8 and 32 mm from the prism apex, the Bragg prism monochromator is expected to deliver an angular profile of 0.062 arcsec FWHM (Fig.48). An analyser operating in opposite asymmetry with $\theta_s = -51^o$ and A=16^o with neutron incidence between 34 and 67 mm from the prism apex would likewise accept a pair of 0.023 arcsec wide neutron peaks separated by 0.22 arcsec (black curve in Fig.49). The rocking curve of the analyser, viz. the convolution of the monochromator beam profile with analyser acceptance, comprises two 0.065 arcsec wide peaks separated by 0.25 arcsec (red curve in Fig.49).

One may envisage tightening the neutron collimation further with Bragg prisms operating at still smaller wavelengths.

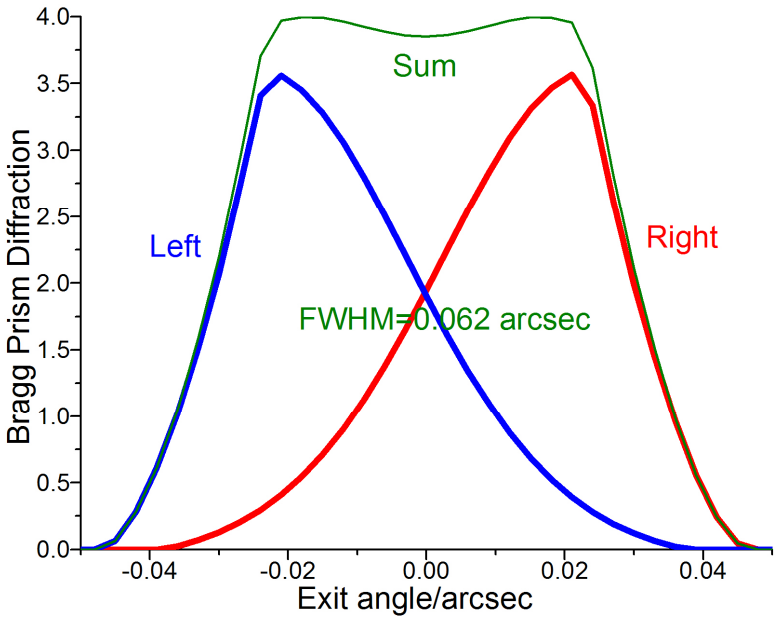

Fig.48 Theoretical flat-topped angular profile from the optimally tailored Bragg prism monochromator (A=172^{o} and θ_S=50.1^{o}) for 1.75 Å neutrons.

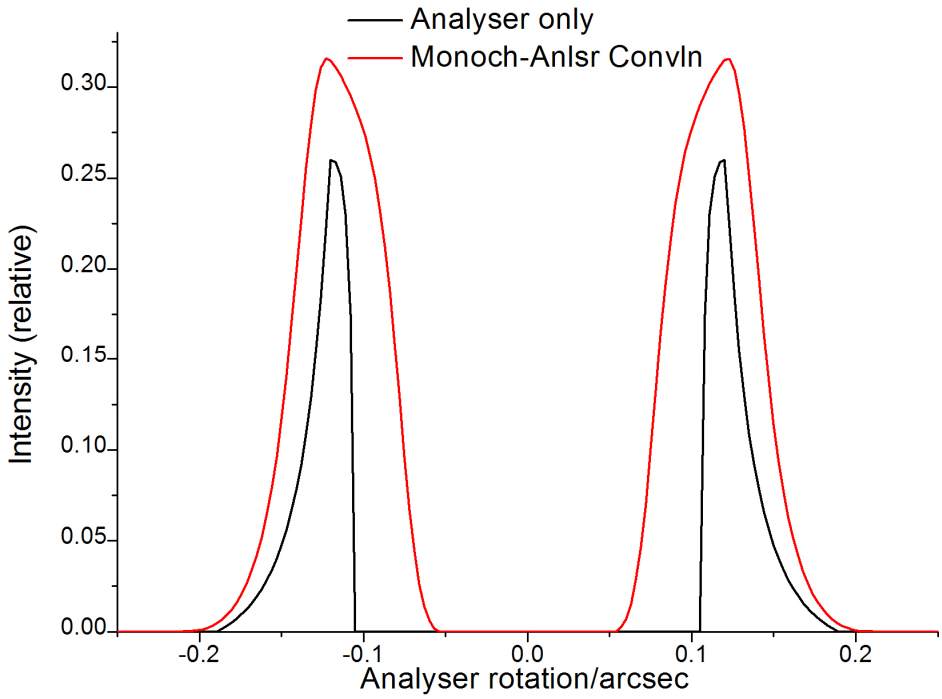

Fig.49 Theoretical acceptance curve (black) of the optimal Bragg prism analyser (A=16^{o} and θ_S=−51^{o}) for 1.75 Å neutrons and its convolution (red) with the monochromator angular profile of Fig.48.

CHAPTER 5

High precision determination of the neutron coherent scattering length

5.0 Introduction

Neutron interferometry as alluded to earlier, affords the most precise determination of the coherent scattering length. Dynamical diffraction of neutrons in a single crystal enables splitting of the neutron wave amplitude into two coherently coupled subbeams separated by a few cm. Insertion of a sample into one of the beam paths introduces a phase shift proportional to the optical path

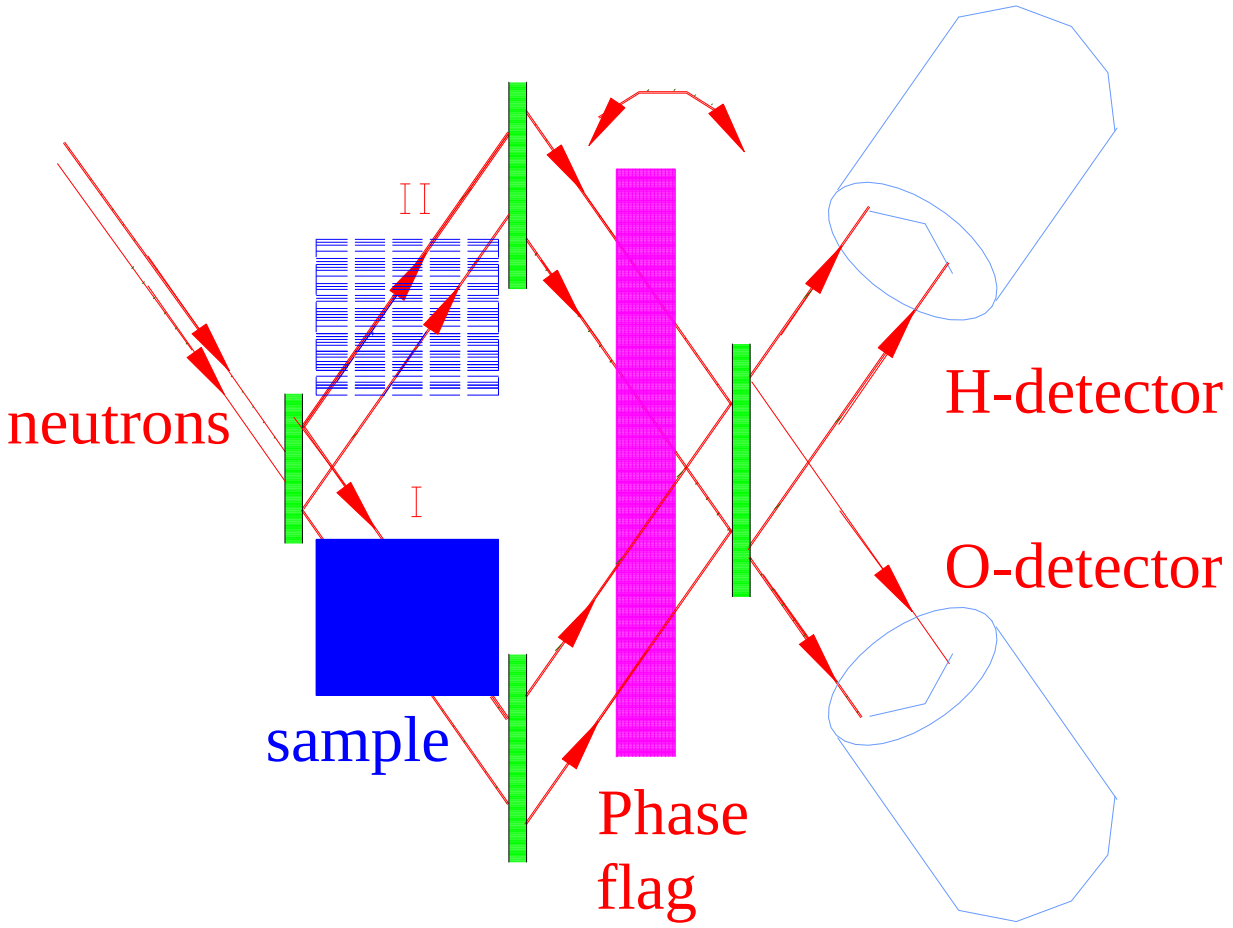

Fig.50 Our proposal depicting the phase measurement by recording the interferograms with the thick sample placed alternately in subbeams I and II of the symmetric LLL IFM.

difference between the two neutron subbeams. Single crystal mirrors recombine the subbeams at the 'analyser' crystal. Rotation of an auxiliary phase flag (Fig.50) generates intensity oscillation patterns of the O & H beams emerging from the analyser. The phase shift caused by the sample insertion, is observable through the shift in the O & H intensity modulation patterns.

5.1 Our proposal: Theory

A sample of refractive index n relative to the ambient changes the neutron wave vector magnitude from k_O to $K= nk_O$. Let us consider a parallel-faced sample slab of thickness D and atomic density N placed in one subbeam of the IFM with neutron incidence angle θ to its front surface (Fig.51). The continuity of tangential components of wave vectors across the ambient-sample interfaces dictates that the wave vector **K** inside the sample can differ from $\mathbf{k_O}$ in ambient air only along the surface normal. The respective normal components $K_\perp$ and $k_\perp$ hence differ by $\Delta K=K_\perp–k_\perp$. Snell's law ($K_{//} =k_{//}$) enables us to write $K_\perp$ as

$$K_\perp = \sqrt{K^2 - K^2 \cos^2\theta'} = k_O \sqrt{n^2 - \cos^2\theta}. \tag{79}$$

The symbol θ′ denotes the glancing angle of refraction. The phase introduced by inserting a sample of thickness D on path I of the IFM is given by

$$\Phi_I = \int \Delta\mathbf{K}.d\mathbf{r} = \left(K_\perp - k_\perp\right) D. \tag{80}$$

Using Eqs.(79) and (80), we arrive at the exact phase formula for neutrons,

$$\Phi_I = k_O D\left(\sqrt{n^2 - \cos^2\theta} - \sin\theta\right), \tag{81}$$

which can be approximated as

$$\Phi_I \approx -\frac{\left(Nb_C - N_a b_a\right) D\lambda}{\sin\theta}, \tag{82}$$

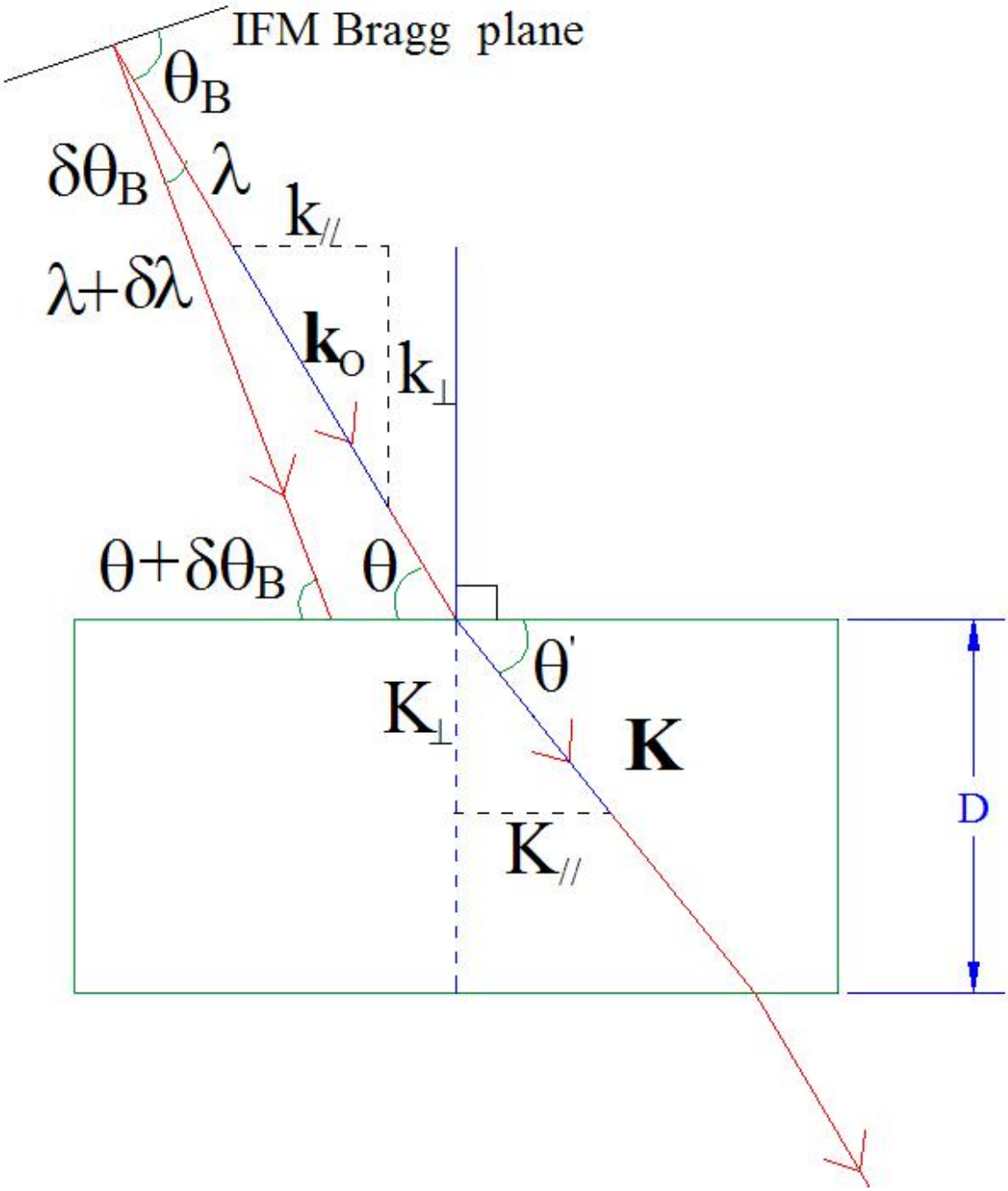

Fig.51 In a symmetric LLL IFM, neutrons of wavelengths λ and λ+δλ propagate at corresponding Bragg angles θ_B and $\theta_B+\delta\theta_B$ to the IFM Bragg planes and hence are incident at angles θ and $\theta+\delta\theta_B$ on the sample. Neutron refraction at the air-sample interfaces introduces a small correction to the phase due to the sample.

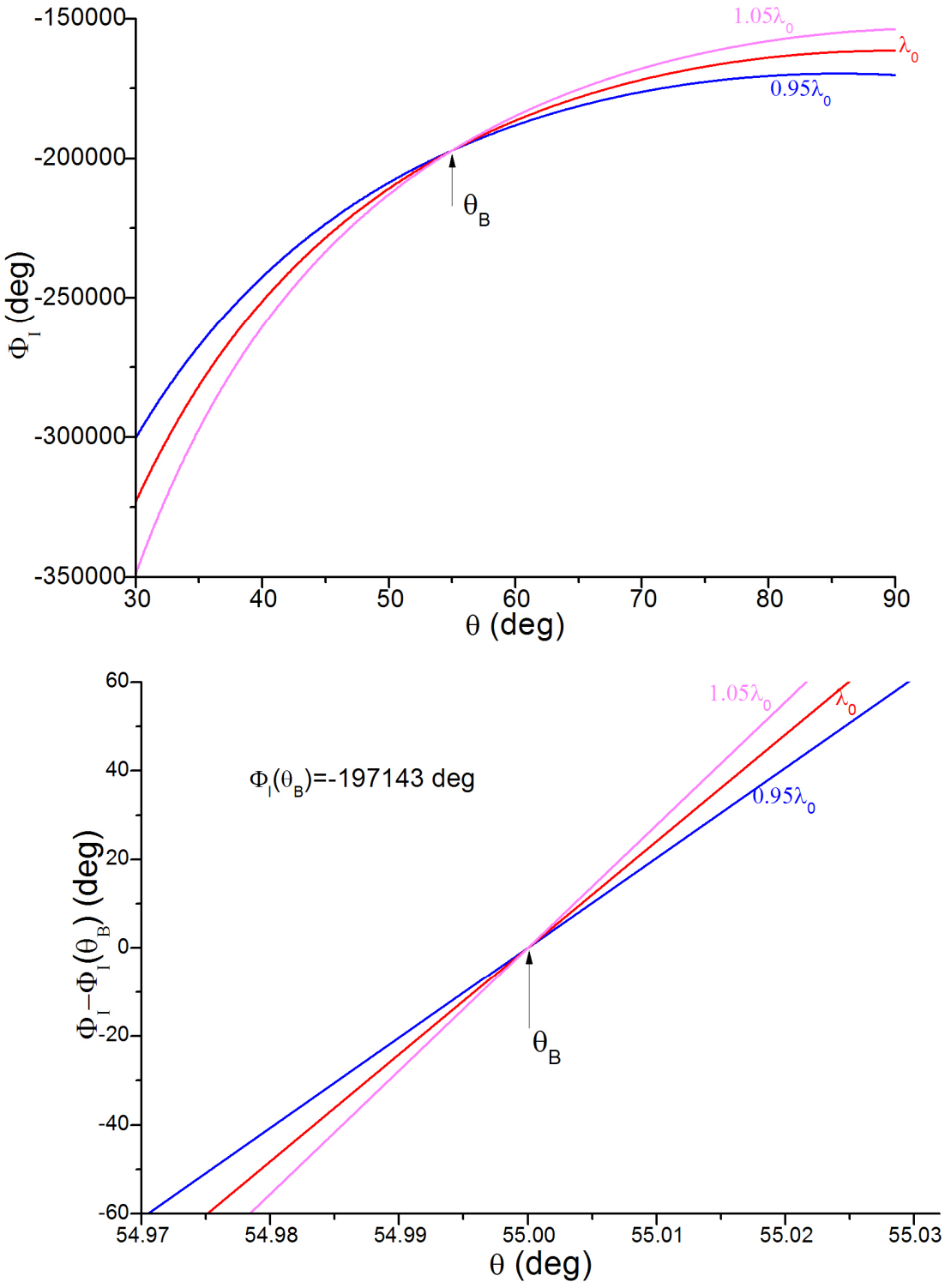

Fig.52 Phase dispersion in a 26.5 mm thick Si sample placed on path I of an IFM as a function of neutron incidence angle θ at central wavelength λ_0 (=5.14Å). The phase becomes nondispersive only for incidence at the Bragg angle θ_B and hence mandates sample alignment to arcsec precision.

since $|n^2-1|< 10^{-5}$. Eq.(82) is the approximate formula hitherto used by earlier researchers. Here, b_C signifies the coherent scattering length of sample, N_a and b_a stand for atomic number density and coherent scattering length respectively, of air and λ denotes the neutron wavelength. Precision of b_C determination can be improved by increasing Φ_I. However, in a symmetric LLL IFM, neutrons of wavelengths λ and $\lambda+\delta\lambda$ propagate at corresponding Bragg angles θ_B and $\theta_B+\delta\theta_B$ to the IFM Bragg planes and hence are incident at angles θ and $\theta+\delta\theta_B$ on the sample (Fig.51). The phase Φ_I, acquired by neutrons with wavelength $\lambda+\delta\lambda$ can be written as

$$\Phi_I = \frac{\pi D}{d}\left(\sqrt{\frac{\sin^2(\theta+\delta\theta_B)}{\sin^2(\theta_B+\delta\theta_B)} - \frac{4d^2(Nb_C - Nb_C)}{\pi}} - \frac{\sin(\theta+\delta\theta_B)}{\sin(\theta_B+\delta\theta_B)}\right), \tag{83}$$

using Eq.(81). Here d denotes Bragg planar spacing of the IFM single crystal. The phase Φ_I at $\lambda+\delta\lambda$ differs from Φ_I at λ. The λ-dependence of Φ_I (Fig.52), thus smears out interferograms, reducing the interference contrast and hence b_C precision since $\int I_O(\lambda)e^{i\Phi_I(\lambda)}d\lambda / \int I_O(\lambda)d\lambda = fe^{i\Phi_{IO}}$ with $f<1$. The large variations in Φ_I with λ allows b_C determination only to within about 1 part in 10^3 [1,4]. Rauch et al. [126] lowered the b_C imprecision to about 4.7 parts in 10^4 by following Scherm's suggestion to insert the sample with its surface parallel to the Bragg planes of the IFM. Neutrons of each wavelength are then incident at its corresponding IFM Bragg angle to the sample ($\lambda=2d\sin\theta$) and the phase (relative to no sample)

$$\Phi_{I-0} = 2\pi D\left(\sqrt{\frac{1}{4d^2} - \frac{Nb_c - N_a b_a}{\pi}} - \frac{1}{2d}\right) \approx -2(Nb_c - N_a b_a)Dd, \tag{84}$$

is nondispersive (Figs.52-53). The major advantage is the elimination of the requirement of precise wavelength determination. The interference pattern does not depend on the wavelength spread of

the beam and remains visible up to very high interference orders [1]. However, here the phase varies significantly with θ as

$$\Phi_{I-0} \approx -2\left(Nb_c - N_a b_a\right) Dd \left(1 - \delta\theta \cot\theta_B + \left(\delta\theta\right)^2 \{1 + 2\cot^2\theta_B\}/2\right), \tag{85}$$

introducing dispersion due to a horizontal sample misalignment δθ. The nondispersivity condition therefore requires the sample to be aligned with arcsec precision (cf. Fig.52 and $\Phi_{0\text{-}I}$ and $\Phi_{II\text{-}0}$ curves in Fig.53 (bottom)). Only at the exact nondispersive setting (viz., $\theta = \theta_B$, to within arcsec), can Φ_I be increased to arbitrarily large values by increasing D without losing interference contrast. At even a slight misalignment δθ, the λ-dependence of the first order term in δθ of the $\Phi_{I\text{-}0}$ variation (85) is large enough to make the phase dispersive (Fig.52), thereby limiting b_C precision.

Ioffe et al. [127] obviated the need for this precise sample alignment by measuring the phase shift between interferograms recorded with the sample placed alternately in subbeams I and II (Fig.50). For a symmetric LLL IFM, this method requires that the sample be parallel translated from path I to path II. Upon translation, the horizontal misset angle δθ changes sign. The phase shift then equals $\Phi(\delta\theta) - (-\Phi(-\delta\theta)) = \Phi(\delta\theta) + \Phi(-\delta\theta)$. This eliminates the large first order variation of the phase (cf. Eq.(85) and $\Phi_{0\text{-}I}$ and $\Phi_{II\text{-}0}$ curves in Fig.53 (bottom) for λ_0) with δθ. The sample alignment thus requires only arcminute precision to locate the minimum in the magnitude of $\Phi_{I\text{-}II}$ (cf. $\Phi_{I\text{-}II}$ curves in Fig.53), occurring at the intersection of $\Phi_{0\text{-}I}$ and $\Phi_{II\text{-}0}$ curves. For small deviations in the incidence angles, the nondispersive phase shift

$$\Phi_{I-II} \approx -\frac{2\left(Nb_c - N_a b_a\right) Dd}{\cos\delta\gamma} \left(2 + \left(\delta\theta\right)^2 \{1 + 2\cot^2\theta_B\}\right), \tag{86}$$

then determines the coherent scattering length

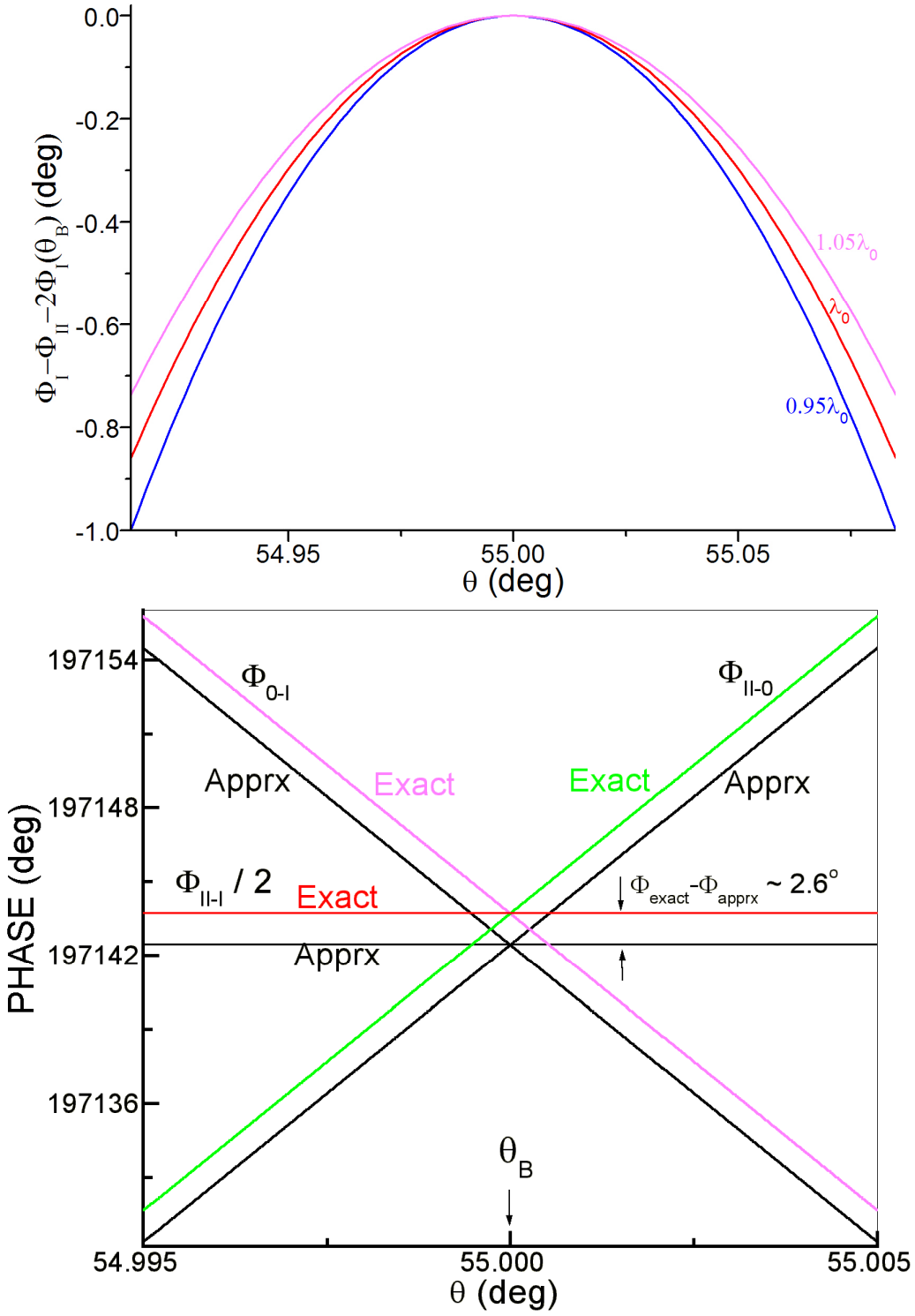

Fig.53 Variation in the difference Φ_I-Φ_{II} between phases arising with the sample on paths I and II with θ near θ_B for three wavelengths (top). The approximate phases for λ_0 are also shown (bottom). Φ_I-Φ_{II} remains nondispersive over ~ arcminute, relaxing the required sample alignment precision.

$$b_C \approx -\frac{\Phi_{I-II}\cos\delta\gamma}{4NDd\left(1+\frac{\delta\theta^2}{2}\left(1+2\cot^2\theta_B\right)\right)}+\frac{N_a b_a}{N}. \quad (87)$$

Here $\delta\gamma$ denotes the vertical misalignment of the sample. The phase Φ_{I-II} is a quadratic function of $\delta\theta$ as well as $\delta\gamma$, (vide Eq.(86)). The exact nondispersive sample alignment hence yields the minimum phase magnitude. Ioffe et al. thus measured parabolic variations Φ_{I-II} individually in each path I and II by changing $\delta\theta$ and $\delta\gamma$ by a few degrees in the vicinity of θ_B incidence and located the corresponding minimum in the phase magnitude to arrive at $\delta\theta = \delta\gamma=0$ settings. With this method, Ioffe et al., [127] achieved $\Delta b_C/b_C$ of $5.1\text{x}10^{-5}$, whose source-wise constituents are listed in the first column of Table 3.

However, it must be noted here that phase vide Eqs.(82 and 86) and hence b_C (Eq.(87)) formulas used hitherto, are approximate. The exact phase formula that accounts for refraction corrections at the ambient-sample interfaces for the sample placed in path I is given by Eq.(81) and for path II, $\Phi_{II} = -\Phi_I$. Thus, the difference of exactly non-dispersive phases for the sample placed in path I and II alternatively with its surfaces aligned parallel to the IFM Bragg planes, equals

$$\Phi_{I-II} = 4\pi D\left(\sqrt{\frac{1}{4d^2}-\frac{Nb_c - N_a b_a}{\pi}}-\frac{1}{2d}\right). \quad (88)$$

This phase is rigorously nondispersive not only in vacuum but also in air. Eq.(88) yields the coherent scattering length

$$b_C = -\frac{\Phi_{I-II}}{4NDd}-\frac{\Phi_{I-II}^2}{16\pi ND^2}+\frac{N_a b_a}{N}. \quad (89)$$

Therefore the correction to the inferred b_C due to the refraction effects

$$\frac{\Delta b_c}{b_c} \approx -\frac{Nb_c d^2}{\pi}. \quad (90)$$

5.1.1 Achieving high precision b_C through optimisation of various parameters

From Eq.(86), it is inferred that to increase the determination of b_C precision, the errors in phase $\Phi_{I\text{-}II}$ measurement and systematic variation in sample thickness D must be reduced. By far, the most predominant contribution arises from the relative variation $\Delta D/D$ in the sample thickness (cf. LHS of Table 3). The precision can thus be improved by increasing D and reducing its ΔD variation. An increase in D dictates a larger Bragg angle (Fig.54) and hence a larger λ and bigger IFM. This results in greater neutron beam broadening equal to $2t\sin\theta_B$ at each blade of IFM, t being the thickness of the IFM blade. Keeping in view the practical limit on the available IFM size and neutron flux at large λ, we limit θ_B to 55^o allowing D=26.5 mm for a 31 mm wide sample and 3 mm wide incident neutron beam (Fig.54). The width of neutron IFM becomes rather large, about 12.5 cm, at this θ_B. Attaining ΔD=0.1 μm with a precision grinding and polishing machine would

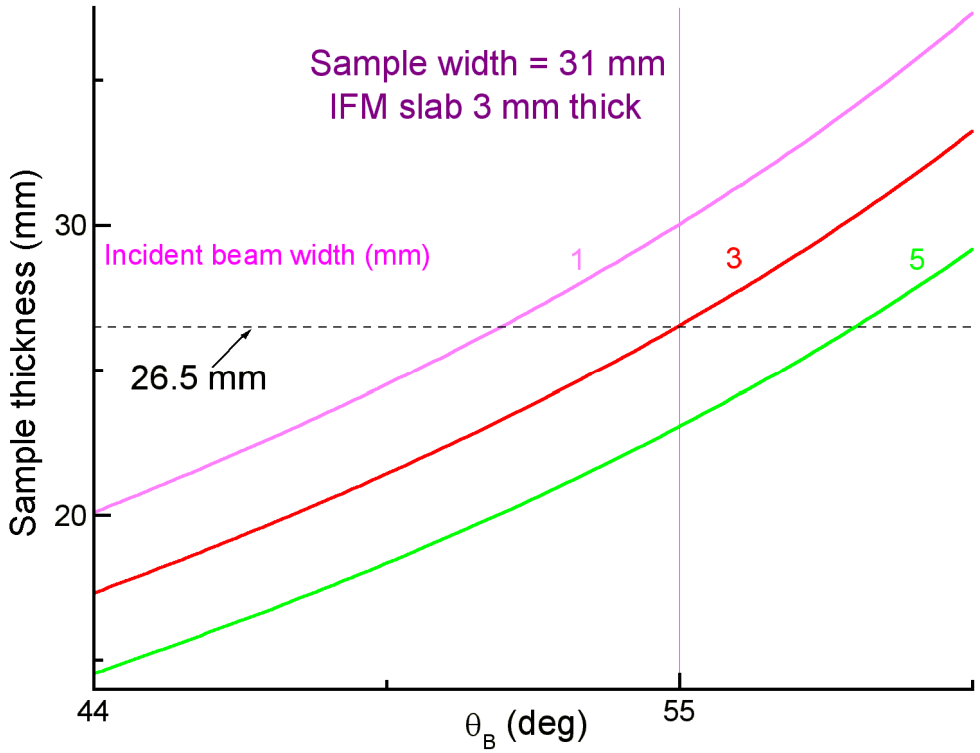

Fig.54 Variation of the allowed sample thickness with Bragg angle of the IFM.

yield about an order of magnitude reduction in the $\Delta D/D$ contribution to $\Delta b_C/b_C$. In addition, the phase also increases by the same factor as D, reducing the $\Delta\Phi/\Phi$ contribution. Further, one can maximise d to 3.14 Å by choosing the {111} Bragg reflection for the Si IFM (hence $\lambda = 5.14$ Å) to enhance Φ by about 63% over that obtainable with the {220} Bragg reflection and reduce $\Delta\Phi/\Phi$. A thermal enclosure around and vibration isolation of the IFM reduces the phase drift to a fraction of a degree over a day [1,127]. The effect of this phase drift over a typical measurement duration of a few hours, is minimised by recording the O and H detector intensities (Fig.50) for the three positions (I, II and Out) of the sample in succession at each angular setting of the phase flag.

A phase error of about 0.3 deg, thus routinely achieved in interferometric experiments, is included in Table 3. Good interference contrast can be achieved even for this high interference order due to the nondispersive configuration [1,126-127]. The contribution from the uncertainty in the refractive index of air, dependent on variations in the temperature, pressure and relative humidity, can be larger than that assumed for $N_a b_a/N = 9.137(9) \times 10^{-3}$ fm in [127]. However, this assumed uncertainty of 2.2 parts per million in b_C precision due to air can be eliminated by performing the experiment in vacuum.

If the sample happens to be a single crystal, extreme care needs to be exercised to ensure neutron incidence far off any Bragg reflection of the sample. The sample then just presents an average refractive index to neutrons. With a crystalline Si sample ($Nd = 1.57 \times 10^{15}$ cm^{-2}), our proposed phase $\Phi_{I\text{-}II} = -394284.8^o$ will yield b_C with ultrahigh precision of a few parts per million (ppm) as shown in the last column of Table 3. The exact and approximate phases for $\delta\gamma=0$ in our proposal are plotted in Fig.53 (bottom curve). The exact phase is greater by about 2.6^o at $\theta=\theta_B$.

The refraction corrections (cf.. Eq.(90)) in b_C of $-6.5*10^{-6}$ for Si{111}, slightly exceeds the proposed precision in magnitude (cf. Table 3), underscoring the importance of refraction effects. Therefore, when such ultrahigh precision is achieved, it becomes mandatory to account for neutron refraction at the ambient-sample interfaces and use the exact formulas for the Φ and b_C respectively (cf. Eqs.(88-89)).

Table 3: Comparison between various $\Delta b_C/b_C$ contributions at Ioffe et al. [127] and our proposal for a Si sample.

Ioffe et al.	**Source**	**Proposed** [111] [220]
$5.0*10^{-5}$	Thickness: $\Delta D \rightarrow 0.1$ μm (Precision grinding)	$3.8*10^{-6}$
$9.0*10^{-6}$	Phase: $\Delta\Phi = 0.3^{o}$, typical	$7.6*10^{-7}$ $1.2*10^{-6}$
$2.2*10^{-6}$	Air: $\Delta(N_a b_a/N)=9*10^{-6}$ fm Eliminate: Vacuum expt	$2.2*10^{-6}$
$1.1*10^{-7}$	Rotation: $\delta\theta \approx 0.01^{o}$, typical	$3.0*10^{-8}$
$1.4*10^{-7}$	Tilt: $\delta\gamma \approx 0.01^{o}$, typical	$1.5*10^{-8}$
$3.7*10^{-9}$	$\Delta\{Nd\}_{Si} = 6*10^{6}$ cm^{-2}	$3.7*10^{-9}$
$5.1*10^{-5}$	Total	$4.4*10^{-6}$ $4.5*10^{-6}$
	Vacuum experiment	$3.9*10^{-6}$ $4.0*10^{-6}$

The refractive index, $n = (1–Nb_C\lambda^2/\pi)^{½}$ of Si for thermal neutrons equals unity to within about 1 part in 10^6. This proposal can thus determine the refractive power, $n–1\approx\pm10^{-6}$, with a relative precision of a few parts in 10^6, and hence the refractive index to a phenomenal precision of a few parts in 10^{12} [156-157].

The refraction corrections of $–2.7*10^{-5}$ and $–1.01x10^{-5}$ fm to b_C for {111} and {220} IFM reflections respectively, due to refraction at air-sample interfaces is of the same order as the Ioffe et al.'s experimentally determined b_C precision of 5 parts in 10^5. Therefore after refraction corrections, b_C values in Ioffe's measurement should be modified to 4.15101(21) and 4.15038 (21) instead of inferred 4.15102(21) and 4.15041(21) values corresponding to IFM reflections {220} with λ= 1.98 Å and {111} with λ= 2.7 Å, respectively.

5.1.2 Dual nondispersive phase shifter

The dual nondispersive phase shifter comprising two identical and parallel phase shifters placed on one path, one before and the other after the mirror blade [Fig.55], in the nondispersive configuration has been recently proposed by Lemmel and Wagh [128]. The effective thickness of the phase shifter gets doubled which results in doubling of the neutron phase Φ ($\propto$D) and halving $\Delta\Phi/\Phi$. The phase shift $\Phi_I(\delta\theta)+\Phi_{II}(-\delta\theta)$, which now can be obtained in a single measurement with this dual phase shifter placed on a single beam path, is exactly nondispersive. Furthermore, the temporal as well as spatial displacements of the wave packet effected by the dual sample in the first gap get cancelled in the second, restoring full interference contrast. A long monolithic sample with a groove cut in the middle (Fig.56) to accommodate the mirror plate attains the exact parallelity and the identical thicknesses for its two segments. Both of these segments are mechanically and thermally coupled. The large nondispersive phase shift can be measured even

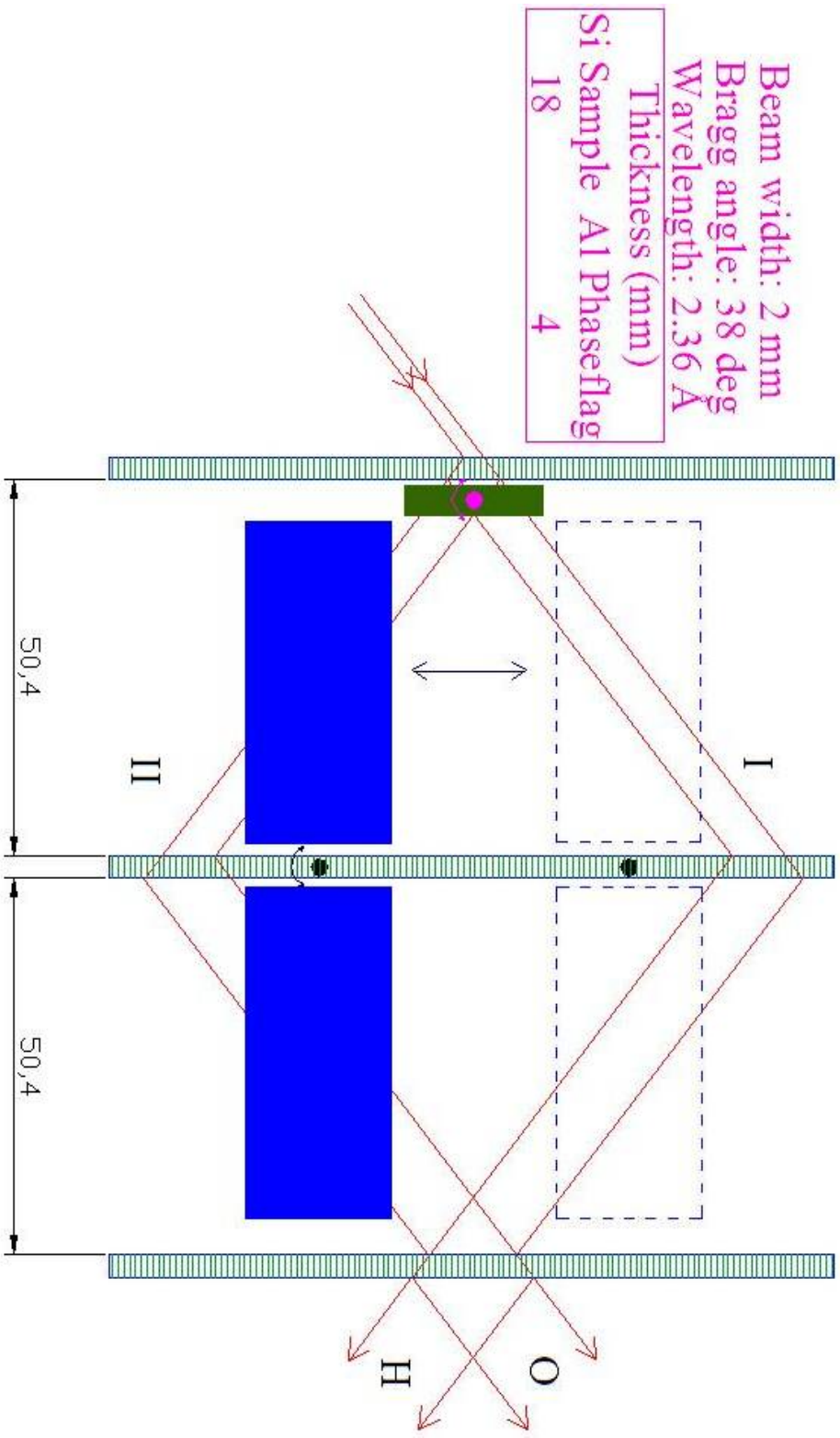

Fig.55 The experimental setup (schematic) employing a large symmetric LLL IFM with dual sample placed in subbeam II.

with a white, and hence high-intensity, incident neutron beam, enabling a fast and precise measurement due to the improved (in fact, FULL) interference contrast.

A dual sample of thickness D each inserted in both gaps of path I (or path II) of the IFM with its surfaces aligned parallel to the IFM Bragg planes yields an exactly non-dispersive phase given by

$$\Phi_{I} = -\Phi_{II} = 4\pi D\left(\sqrt{\frac{1}{4d^2} - \frac{Nb_c - N_a b_a}{\pi}} - \frac{1}{2d}\right), \tag{91}$$

and the phase difference between path I and II equals,

$$\Phi_{I-II} = 8\pi D\left(\sqrt{\frac{1}{4d^2} - \frac{Nb_c - N_a b_a}{\pi}} - \frac{1}{2d}\right). \tag{92}$$

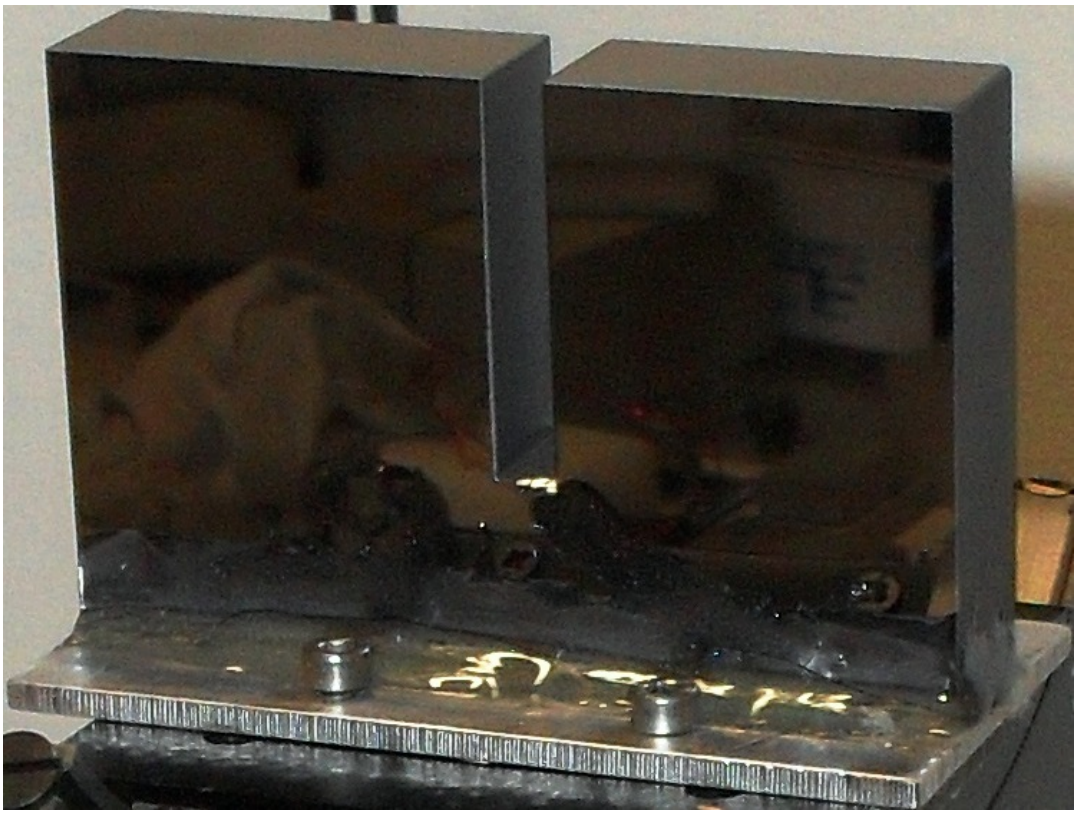

Fig.56 Dual Si-sample mounted on a plate.

A 124 mm wide symmetric {220} LLL IFM [158] fabricated by Prof. Rauch′s group at the Atominstitut in Vienna, with 50.4 mm gaps between successive blades operating at a Bragg angle of 38° for 2.36Å neutrons, constrains the maximum allowed thickness of the dual sample to 18 mm due to beam widening in the mirror blade. The source-wise contributions to $\Delta b_C/b_C$ for the Si sample are listed in LHS of Table 4 for the Ioffe et al. experiment [127] and in RHS for our

Table 4: Comparison between various $\Delta b_C/b_C$ contributions at Ioffe et al. [127] and in the proposed experiments with dual Si-sample.

Ioffe et al	**Source**	**Proposed** [111] [220]
$5.0*10^{-5}$	Thickness: $\Delta D \rightarrow 0.1$ μm (Precision grinding)	$2.78*10^{-6}$
$9.0*10^{-6}$	Phase: $\Delta\Phi = 0.3^{o}$, typical	$5.6*10^{-7}$ $9.1*10^{-7}$
$2.2*10^{-6}$	Air: $\Delta(N_a b_a/N)=9*10^{-6}$ fm Eliminate: Vacuum expt	$2.2*10^{-6}$
$1.1*10^{-7}$	Rotation: $\delta\theta \approx 0.01^{o}$, typical	$6.5*10^{-8}$
$1.4*10^{-7}$	Tilt: $\delta\gamma \approx 0.01^{o}$, typical	$1.5*10^{-8}$
$3.7*10^{-9}$	$\Delta\{Nd\}_{Si} = 6*10^{6}$ cm^{-2}	$3.7*10^{-9}$
$5.1*10^{-5}$	Total	$3.6*10^{-6}$ $3.7*10^{-6}$
	Vacuum experiment	$2.8*10^{-6}$ $2.9*10^{-6}$

proposed dual sample. The dual sample affords greater precision than the single sample due to its greater effective thickness of 36 mm.

5.2 EXPERIMENTAL

The experiment was performed at the S18 beam port of 58 MW Institut Laue Langevin (ILL) reactor in Grenoble, France. The Si perfect-crystal monochromator and IFM are operated in a non-dispersive configuration which provides a narrow rocking curve with 1.8" FWHM at a wavelength of 1.8Å. To attain greater contrast and phase stability, the optical bench is shielded against

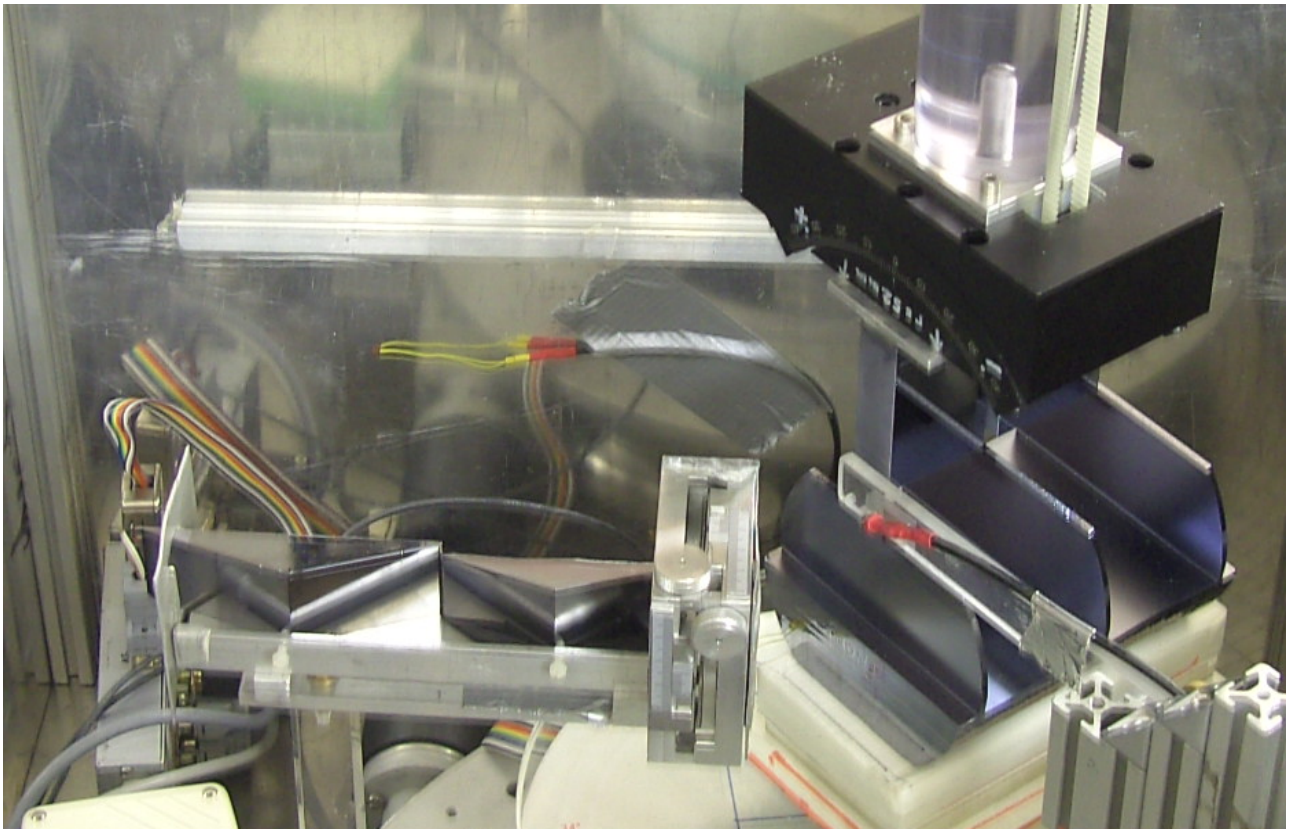

Fig.57 A photograph of the experimental setup at S18 ILL, depicting a pair of amorphous Si prisms each of 120^{o} apex angles placed before the symmetric {220} LLL IFM to remove the $\lambda/2$ from monochromatic neutron beam. Dual sample mounted on a plate, is hanging from the top.

vibrations and thermal drifts. A pair of amorphous Si prisms each of 120^o apex angles is placed before the symmetric {220} LLL IFM to remove the second harmonic ($\lambda/2$) from monochromatic neutron beam (Fig.57). The 93 mm long sample had a 6 mm wide groove in the middle to accommodate the mirror blade of IFM (Fig.56). The sample was cut and ground from a single crystal Si ingot, at an orientation carefully selected so that neutrons incident at 38^o to the sample surface would be at least 10^o away from exciting any major reflection in Bragg or Laue configuration, at a company in Grenoble.

5.2.1 Recording of the interferograms

The relative intensity patterns recorded for the O and H exit beams, depend upon the phase difference of the neutron subbeams traversing path I relative to path II. We record an interferogram with a 4 mm thick Al flat phase flag positioned between the splitter and mirror blades of the IFM such that it intercepts both neutron paths (Fig.55). A rotation ζ of this phase flag from parallelity to IFM blades induces a differential thickness between the two paths given by

$$D_{Al}(\zeta) = D_{II}(\zeta) - D_{I}(\zeta) \;=\; D_0 \frac{2\sin\theta_B \sin\zeta}{\cos^2\theta_B - \sin^2\zeta} \tag{93}$$

and a phase shift

$$\chi(\zeta) = -N_{Al} b_{Al} \lambda D_{Al}(\zeta), \tag{94}$$

proportional to $D_{Al}(\zeta)$. Here D_0, N_{Al} and b_{Al} denote thickness, atom density and coherent scattering length of aluminum phase shifter respectively. O and H intensity patterns recorded by varying χ through ζ, are governed by Eqs.(41a and 41b).

The experiment was performed with λ=2.36 Å corresponding to θ_B = 38^o and an empty IFM rocking curve with 2.52 arcsec FWHM was recorded with respect to monochromator to align IFM. The empty IFM contrast, defined by Eq.(42), dropped from 80% at θ_B =30^o (λ=1.92Å) to about 40% at θ_B = 38^o since now neutrons sampled the less perfect outer regions of the mirror. By translating the IFM horizontally and vertically, the contrast was optimised to about 65%.

Next, the O+H intensity recorded as a function of the sample translation transverse to Bragg planes in the IFM, exhibited a plateau each in paths I and II. The sample position for each path was set at the centre of the respective plateau. With the sample placed in either path I or II, O and H interferograms were recorded. The contrast dropped to ~ 60% on placing the sample at either of these positions. For the Si sample, the attenuation cross-section (σ_{attn}= 0.175 barn) does not significantly influence the real part of the refractive index and hence a large neutron path length of 58.5 mm within the sample in nondispersive configuration still yielded a good interference contrast.

5.2.2 Data analysis

For each interferogram, intensity oscillations O*<O+H>/(O+H) were fitted to sinusoidal variation $I = I_O(1 + A\cos(B\chi + \Phi))$, yielding the average intensity I_O, contrast A, normalized frequency B and phase Φ. The phases extracted from interferograms acquired at several rotations ε and tilts γ of the sample displayed the expected parabolic variations (Fig.58). The sample was then set to the correct orientation (ε_0, γ_0) where the phase magnitude exhibited a minimum. A large number of successive sample-in and sample-out interferometric scan pairs were then made alternately for path I and II (Fig.59), punctuated with realignments of the IFM whenever the contrast dropped below about 50%. Phases inferred as a function of oscillation frequency are plotted in Fig.60. The

measurements exhibited large, erratic phase drifts (Fig.61) due to uncontrollable variations in the ambient temperature, humidity, air pressure and background magnetic field ramps generated by neighbouring experiments.

The frequency of interference oscillations, relative to that expected for the 4 mm thick Al flag, varied significantly between path I and II not only for sample-in scans but for sample-(raised) out scans as well, indicating drastically different rates of the two phase drifts. This led to erroneously large inferred phase shifts between paths I and II (Figs.60 and 61). However, the interference contrast as well as average intensity dropped gradually over these scans (Fig.62) due to temperature drifts causing a misalignment between the monochromator and IFM. Average intensity and interference contrast both decreased as a function of scan number. We note that the interference contrast is greater for path I while the average intensity is always higher for path II. It was only for the last (13 + 13) scan pairs that the oscillation frequencies converged near a single value (Fig.61), yielding a nearly constant phase shift $\Phi_{I\text{-}II}$ = + 256.7 ± 0.30 modulo 720 deg (Fig.63). Variations in the planarity and thickness of the sample surfaces, mapped metrologically

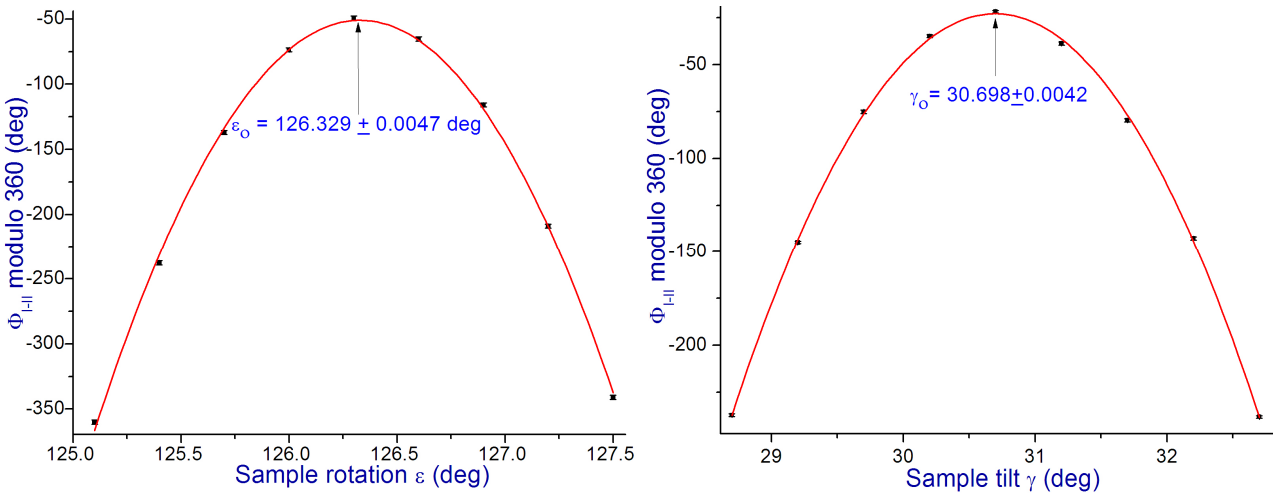

Fig.58 Optimisation of the sample rotation and tilt.

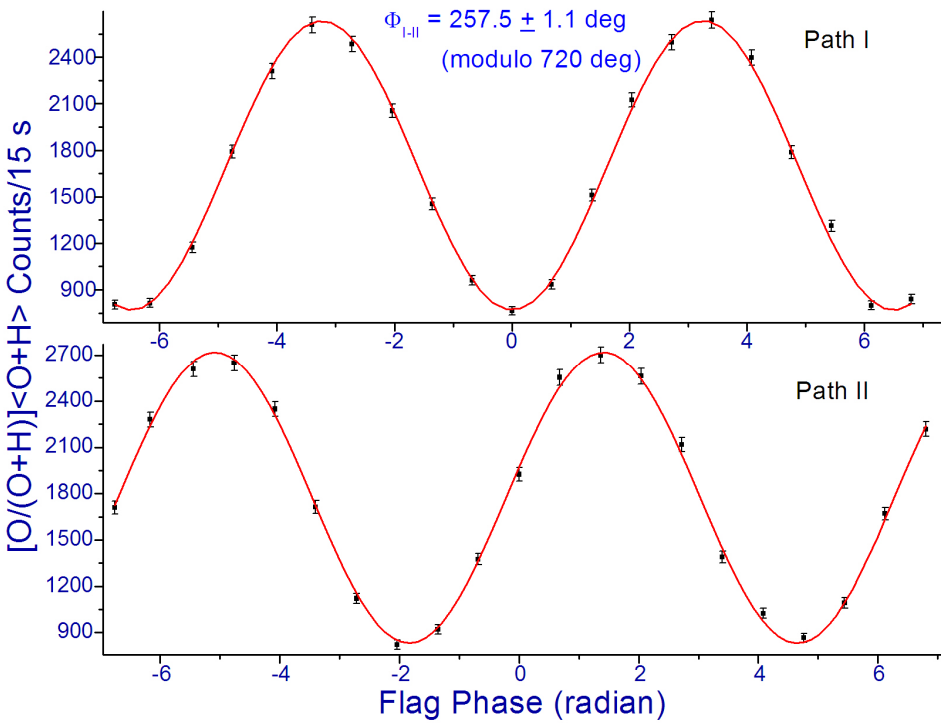

Fig.59 Typical interferograms for path I and II as a function of the flag phase.

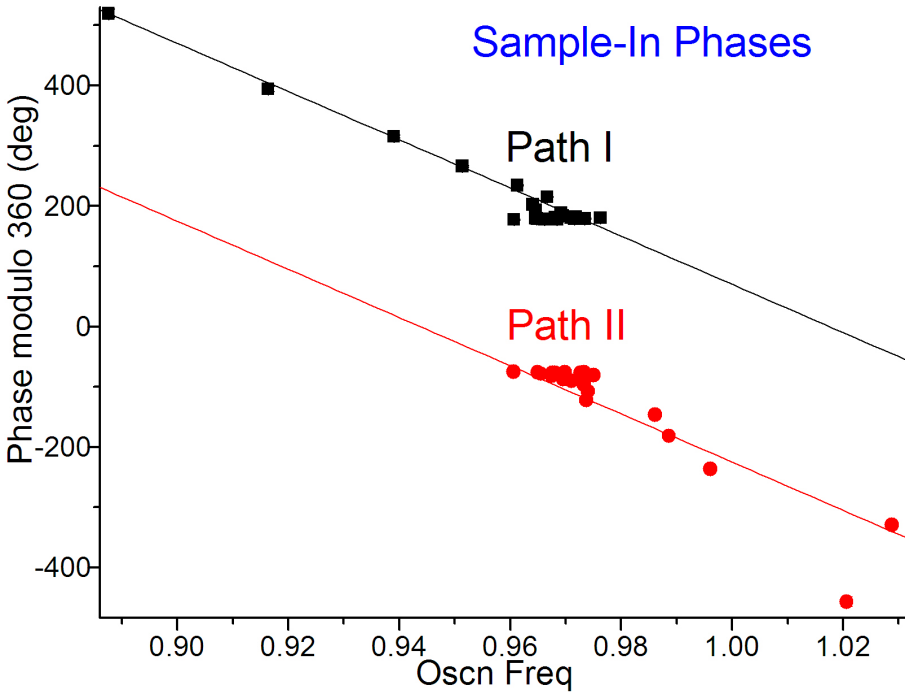

Fig.60 Variation in phase with the interferogram oscillation frequency normalised to that expected theoretically.

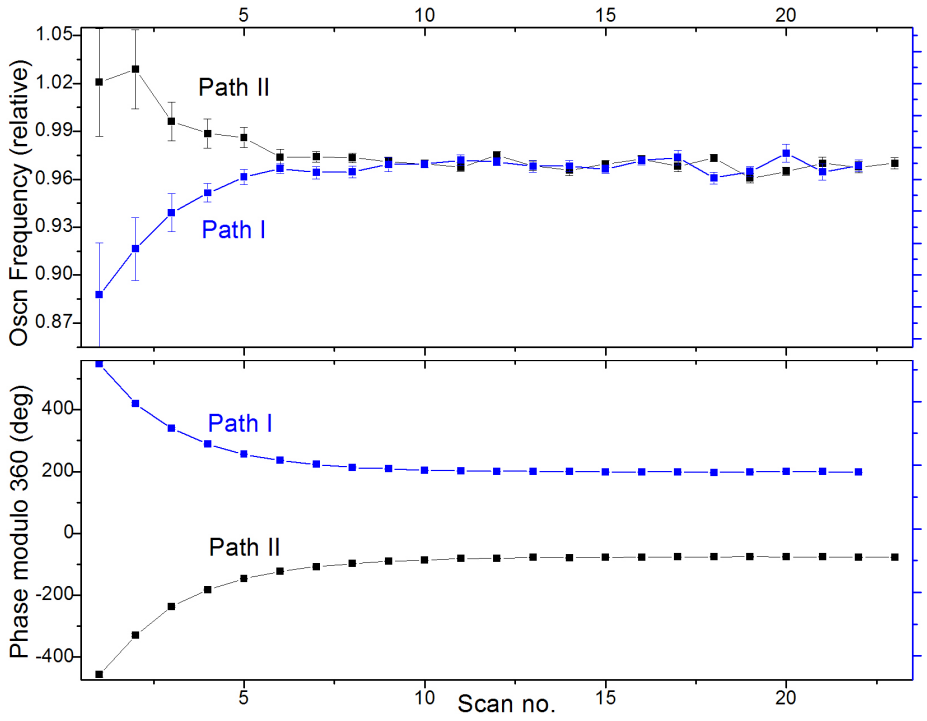

Fig.61 Oscillation frequency and phase with scan number.

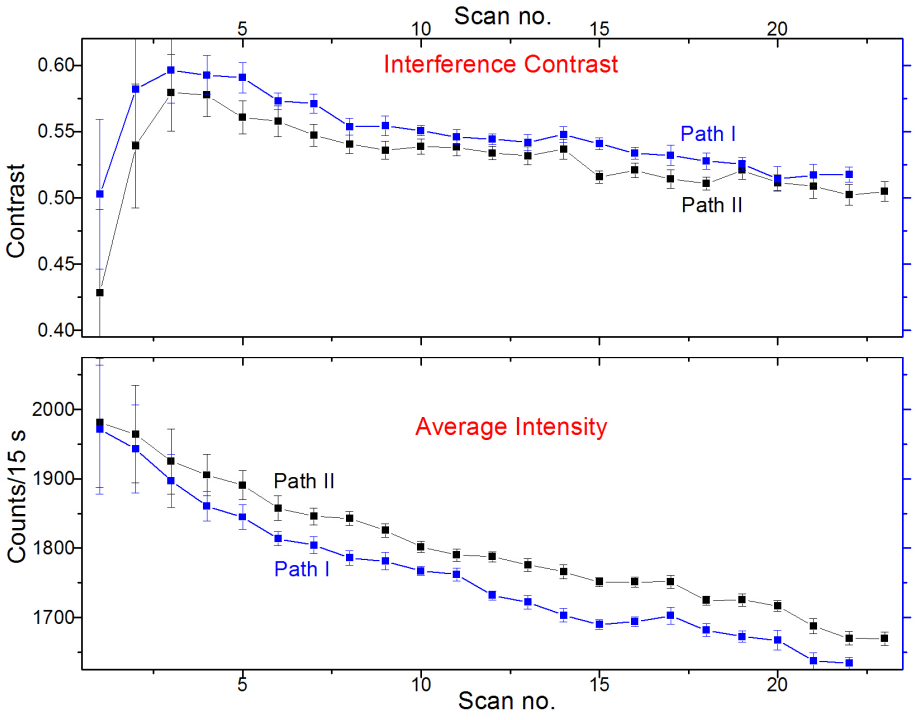

Fig.62 Interference contrast and average intensity.

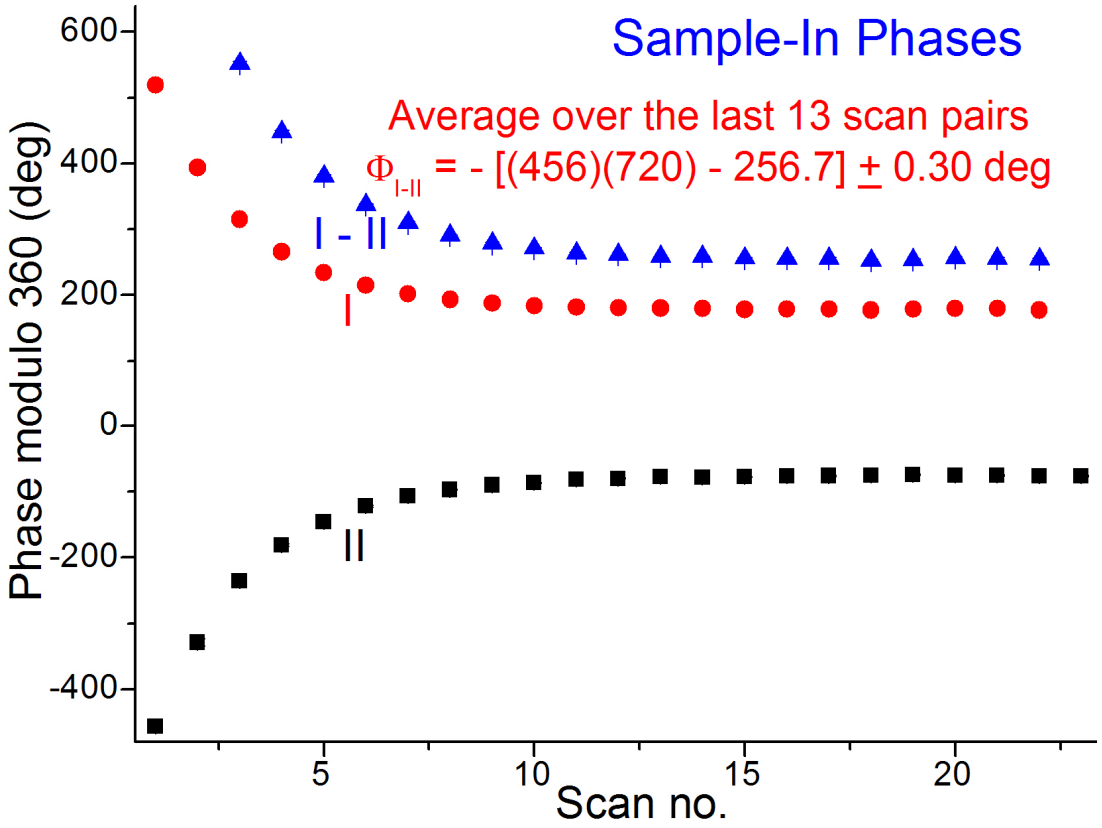

Fig.63 Path I, II and I-II phases during the run.

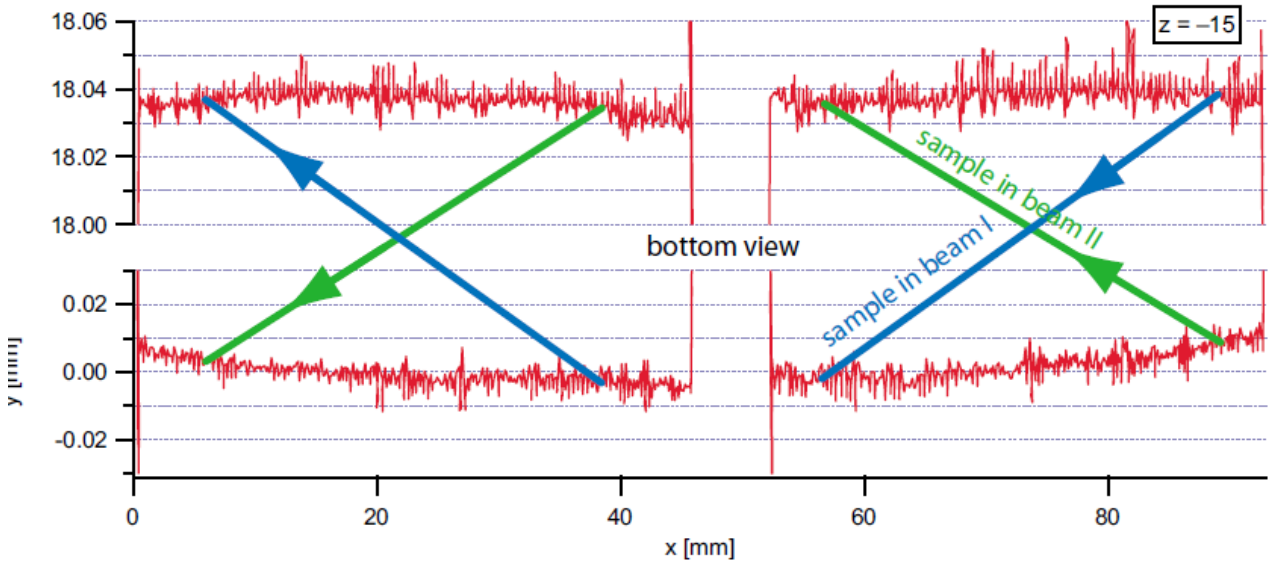

Fig.64 Metrological mapping of the Si sample thickness along with the neutron trajectories in paths I and II.

after the experiment turned out to be unacceptably large (Fig.64). The thicknesses D on paths I and II, averaged over the beam extent, were (1.804+1.804) cm and (1.8027+1.8031) cm respectively. Using the previous measurements of b_C for Si [127], we deduced Sample In – Out phases of – 456 X 360 + 98.4 ± 0.22 and + 456 X 360 – 158.3 ± 0.21 deg for paths I and II respectively so that Φ_{I-II} = – 456 X 720 + 256.7 ± 0.30 deg. The Si b_C value of 4.1479 ± 0.0023 fm was arrived at after adding a correction of 0.009137 fm for air, the major part of the b_C error arising from the 10 μm error in the 18 mm sample thickness. The correction of -1.01×10^{-5} fm to b_C due to refraction at air-sample interfaces is too small in comparison [160-161]. While errors arising due to large thickness variations limited our effort to measure b_C with high precision, the experiment demonstrated the operational superiority of a dual nondispersive sample. Further, this dual sample has facilitated observation of the largest non-dispersive phase (911 interference orders) to date, to within a ppm for the first time.

5.2.3 Repeat Experiment

In 2011, we repeated the experiment to improve b_C precision at the S18 beam port, Institut Laue Langevin (ILL) reactor in Grenoble, France. This time, symmetric {220} LLL IFM operated at slightly different Bragg angle of 37.92° for 2.36Å neutrons. The Si dual sample was ground again and polished to a better accuracy which reduced the average sample thickness to 17.98 mm (Fig.56). The IFM setup was enclosed in an aluminium box equipped with heating coils and Peltier elements to regulate its temperature. Compressed air was passed through a constant-temperature water bath and blown gently into four corners near the box bottom to eliminate thermal gradients near the IFM. The O+H intensity was recorded as a function of the sample translation within the

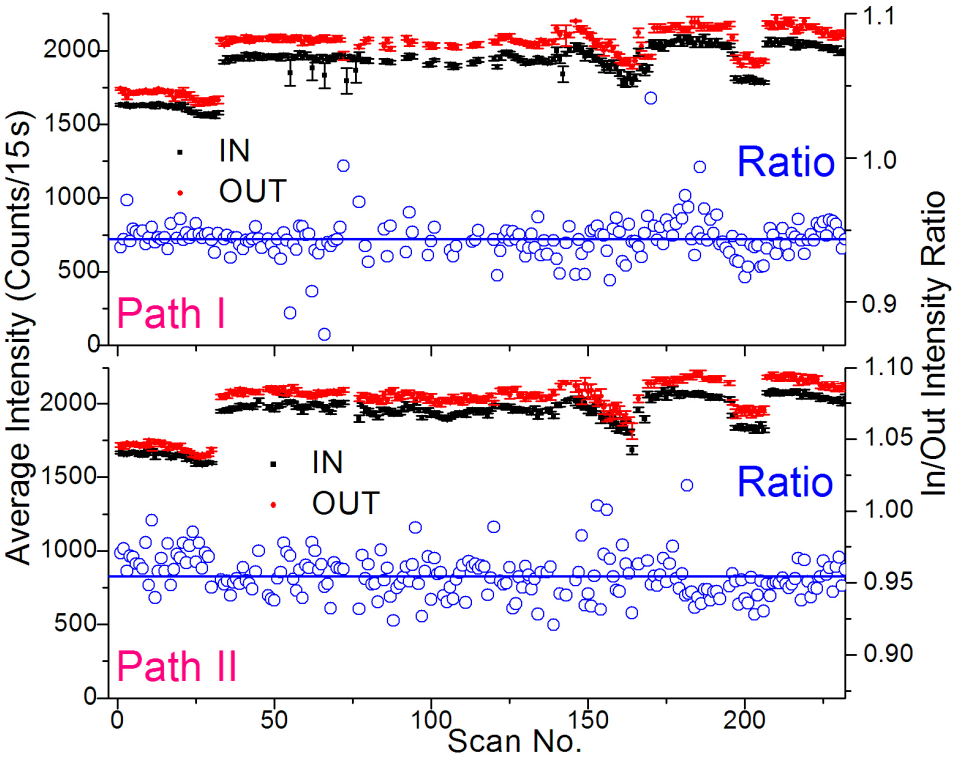

Fig.65 Average intensity with the sample placed IN and OUTSIDE paths I and II.

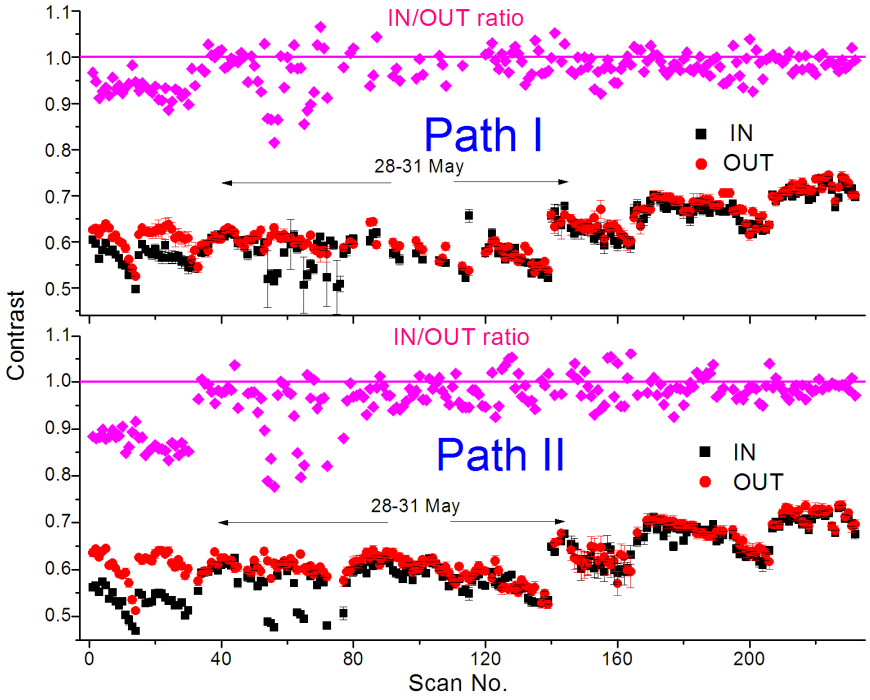

Fig.66 Interference contrasts with the sample placed IN and OUTSIDE paths I and II.

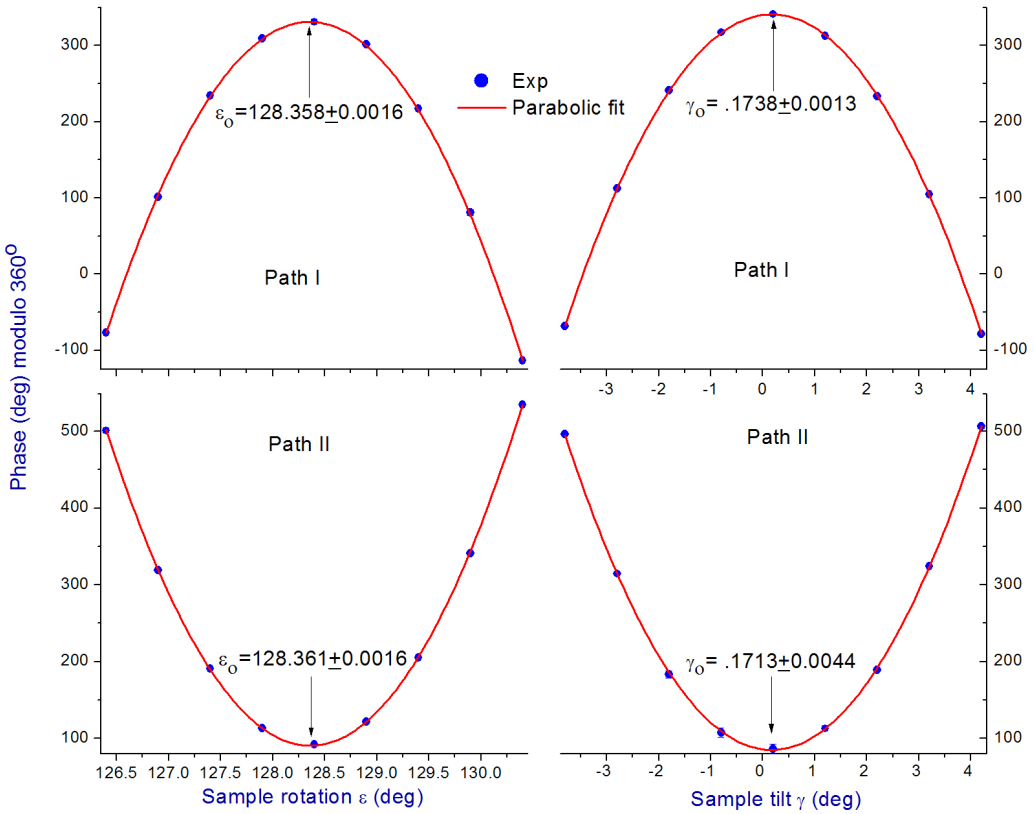

Fig.67 Optimisation of the sample rotation and tilt.

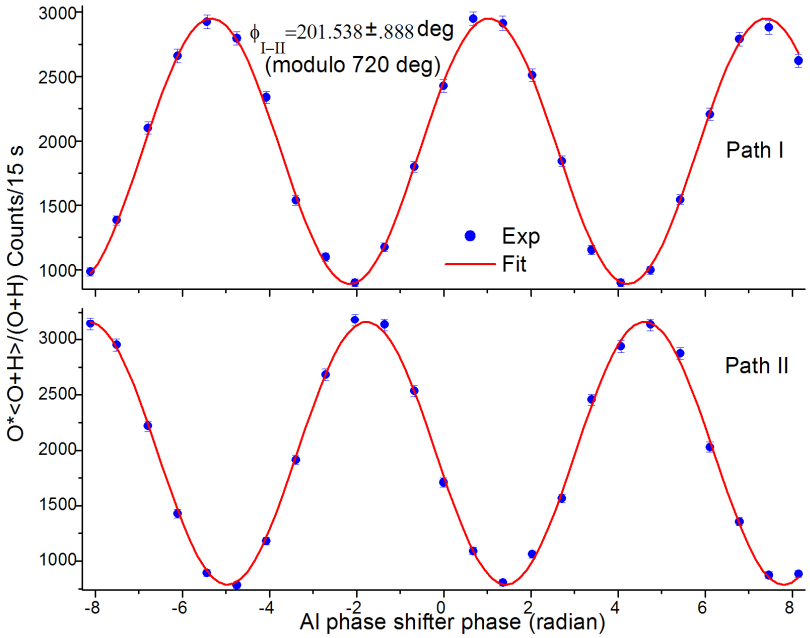

Fig.68 Interferograms with the sample placed in paths I and II.

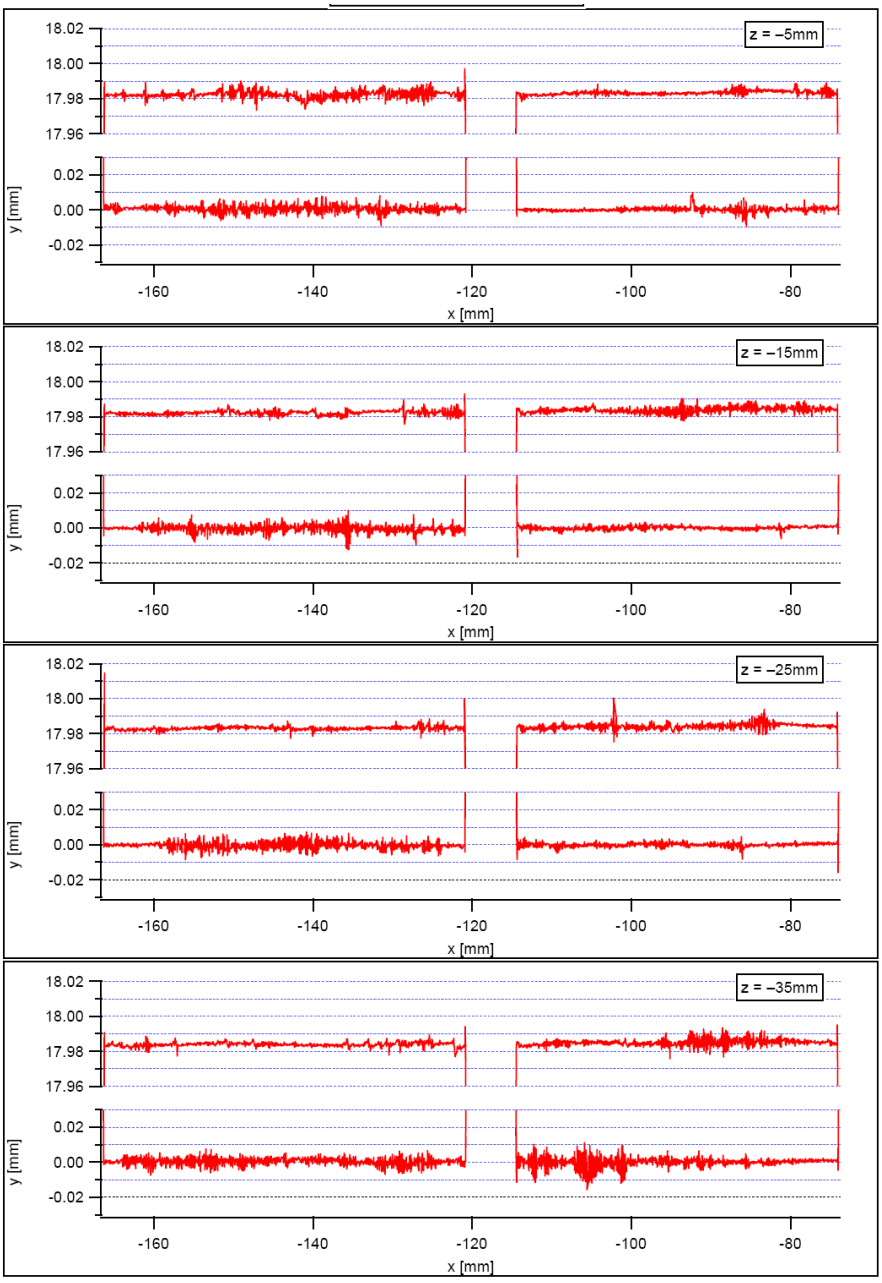

Fig.69 New metrological mapping of the Si dual sample.

IFM and the sample position for path I and II was set at the centre of the intensity plateau obtained for the respective path. During the first week of the experiment, it was difficult to obtain interferograms with good and stable contrasts, due to a vacuum pump inadvertently placed over the IFM cabin roof by the reactor operational staff members. On isolating its vibrations from the cabin,

we were able to achieve empty IFM contrasts up to about 75 %. On placing the sample in path I or II, the intensity dropped only by about 5% (Fig.65) and the interference contrast remained essentially unaltered over a majority of scans (Fig.66). We note that the actual neutron path length of 58.5 mm within the Si dual sample though very large, still yielded a very good contrast underscoring the importance of measurements in nondispersive sample configuration. Further, small intensity decrease in measurements made with the sample IN positions compared to sample OUT scans is due to the incoherent scattering and absorption of neutrons within sample. The phases extracted from interferograms acquired at several rotations ε and tilts γ of the sample in path I and II were fitted to parabolic curves (Fig.67). The sample was then set to the correct orientation (ε_0, γ_0) where the phase magnitude exhibited a minimum. A large number of successive sample-in and -out interferometric scan pairs were then made alternately for path I and II. A typical interferogram for this set of measurements is shown in Fig.68. The regulated air flow within the temperature-controlled aluminium enclosure yielded good interference contrasts, but also reduced the relative air humidity to between 5 and 10% which, in turn, led to a large variation in the measured phases. The frequency of interference oscillations remained fairly constant throughout the measurements.

To arrive at the correct phase, we carefully analysed the temperature and humidity data. We observed that the measured phases on either path remained closely constant when thermal gradients in the IFM vicinity were low and the relative humidity inside the IFM cabin ranged between 35 and 40%. From 95 such interferograms for paths I and II and using the previous measurements of b_C for Si [127], we deduced phases of – 455 X 360 – 54.811 ± 0.154 deg and + 455 X 360 – 256.49 ± 0.117 deg for paths I and II respectively so that $\Phi_{I\text{-}II}$ = – 455 X 720 + 201.679 ± 0.193 deg. After considering a 1μm uncertainty in the sample thickness of 35.96 mm (Fig.69), thermal expansion of

Si at 26.2^{o}C, applying a correction of 0.009137 fm to b_C for ambient air and -1.01×10^{-5} fm due to refraction at air-sample interfaces, a Si b_C value of 4.15195 ± 0.00011 fm was arrived at [162-163]. This observation of a large non-dispersive phase (910 interference orders) to within 1 ppm, led to the interferometric determination of b_C and n of silicon to within 27 parts in 10^6 and 5 parts in 10^{11} respectively.

Our measured Si b_C value of 4.15195 ± 0.00011 fm is in reasonable agreement with the b_C values of 4.1507 ± 0.0002 fm and 4.1534 ± 0.0010 fm, obtained by Ioffe et al. [127] and Shull and Oberteuffer [78] respectively. These b_C values include scattering contributions from both the electronic as well as nuclear charge. However, we have achieved an improved b_C precision by a factor of about 1.9 to that attained by Ioffe et al.

By further improving the uniformity in sample thickness and enhancing the thermomechanical stability of the IFM, it should be possible to achieve the proposed b_C determination to within a few parts in 10^6.

CHAPTER 6

Conclusion and Future directions

The objective of this Chapter is to summarize the main findings of this thesis and to shed some light on the future directions for the research work presented in Chapters 3, 4 and 5.

I. Neutron forward diffraction by Bragg prisms

In Chapter 3, we enunciated the theory of neutron forward diffraction by Bragg prisms and derived analytic expressions for the intensity fraction and deflection of the forward diffracted neutron beam within the framework of dynamical diffraction theory. In the vicinity of a Bragg reflection, the neutron deflection deviates sharply from that for an amorphous prism reaching opposite extrema at either end of the total reflectivity domain and exhibits several orders of magnitude greater sensitivity to the incidence angle variation. Using a 2 arcsec wide 5.24 Å neutron beam from a 7-bounce Bonse-Hart monochromator-analyser setup, we observed the variations of the deflection and transmission of the neutron beam across a Bragg reflection, for several Bragg Si prisms. The observed Bragg prism deflections deviate from amorphous prism deflections by up to 27% and deflection sensitivities up to 0.43 arcsec per arcsec variation in the incidence angle are observed, thus realising 3 orders of magnitude greater deflection sensitivity to the incidence angle variation than that obtainable with amorphous prisms. The results agree well with the predictions of dynamical diffraction theory.

The smooth deflection tuning ability and the several orders of magnitude higher sensitivity are the key advantages of Bragg prisms over conventional prisms. These prisms can also be employed in succession to achieve a larger deflection sensitivity, albeit with a concomitant intensity loss. The theoretical prediction of a sign change of the deflection (Fig.16) on the low θ-side by a suitably

selected asymmetric Bragg prism may be experimentally verified and employed in applications. The use of Bragg prisms can also be explored in neutron interferometric Laue phase measurements [164-165]. Within the channel-cut monochromator as well as analyser silicon crystals, each performing 7 {111} Ewald reflections, an amorphous Si wedge each was inserted after 3 reflections to deflect neutrons of 5.24 Å by about 4 arcsec. Treimer et al. [112] thus attained an analyser rocking curve width ~ 2 arcsec, reduced from Darwin width ~ 6 arcsec. The angular width achievable thus can be trimmed down to a fraction of Darwin width by placing a Si-Bragg prism instead of an amorphous prism albeit with a concomitant loss of intensity. One may envisage further, the tuning of the angular width of such rocking curves by Bragg prism rotation.

The observations presented in Chapter 3 have led to the design and operation of a novel super-collimator Bragg prism which produced a neutron beam with a sub-arcsec angular width.

II. First sub-arcsec collimation of monochromatic neutron beam

Chapter 4 reported attainment of the first sub-arcsec collimation of a monochromatic neutron beam with a Bragg prism, viz. a single crystal prism operating in the vicinity of Bragg incidence. Analytical as well numerical computations based on the dynamical diffraction theory, led to the optimised collimator configuration of a Si {111} Bragg prism for 5.26Å neutrons. This optimal collimator produced a nearly plane wave neutron beam with a 0.58 arcsec angular width. With a similarly optimised Bragg prism analyser of opposite asymmetry, we recorded a 0.62 arcsec wide virgin rocking curve. The availability of such a sharp rocking curve has enabled several experimental firsts. We have recorded the first ever SUSANS spectrum in $Q \sim 10^{-6}$ $Å^{-1}$ range with a hydroxyapatite casein protein sample and demonstrated the instrument capability of characterising agglomerates up to 150 μm in size. The super-collimated monochromatic beam has also enabled us

to record the first neutron diffraction pattern from a macroscopic grating of 200 μm period. The transverse coherence length of 175 μm (FWHM) extracted from the analysis of this pattern is the greatest achieved to date for Å wavelength neutrons.

A magnetic air prism between the monochromator and analyser Bragg prisms can separate the up- and down-spin components of the neutron beam, thus providing a polarised SUSANS facility [166-168].

As indicated in Chapter 4, one can produce even tighter neutron collimation by employing other Bragg reflections, asymmetry and apex angles. The monochromator and analyser Bragg prisms characterised in Chapter 4 can be used to produce a sharper neutron beam by employing higher order reflections. This Bragg prism pair operating near {333} Bragg incidence of 1.75 Å neutrons can achieve a 0.065 arcsec wide rocking curve. The transverse coherence length of 525 μm (FWHM) of this beam will facilitate SUSANS studies down to $3x10^{-7}$ $Å^{-1}$ and characterise agglomerates up to 450 μm in size. A magnetic air prism between the monochromator and sample would then yield a Polarised submicro-$Å^{-1}$ SUSANS facility.

One may envisage tightening the neutron collimation further with Bragg prisms operating at still smaller wavelengths. However, there are practical limits such as the mechanical stability of the apparatus, the minimum rotation step achievable for the goniometer and the inherent weakness of neutron sources in terms of flux. Only when the next generation neutron sources like Inertial Confinement Fusion based or advanced pulsed sources, becomes operational, may Bragg prisms be able to deliver sufficiently strong neutron beam with extremely narrow angular profiles.

However, with X-rays, these novel Bragg prisms can produce sharper angular profiles than neutron beams as photon flux available currently is many orders of magnitude greater compared to neutrons.

III. High precision determination of neutron coherent scattering

In Chapter 5, a proposal for high-precision determination of the neutron coherent scattering length is described. With this proposal, the neutron coherent scattering length and refractive index for Si become determinable to within a few parts per million and a few parts per trillion respectively, for slow neutrons. When such ultra high precision is achieved, the refraction correction at the ambient-sample interface becomes mandatory. We have derived the correct formula for the phase and b_C. In a proof-of-principle measurement, we used a dual non-dispersive sample to measure the largest non-dispersive phase (911 interference orders) to date, to within 1 ppm and the Si b_C value of 4.1479 ±0.0023 fm was arrived at after adding a correction of 0.009137 fm for ambient air. The major part of the b_C error arose from the 10 μm error in the 18 mm sample thickness. The correction of -1.01×10^{-5} fm to b_C due to refraction at air-sample interfaces was too small in comparison.

A repeat experiment with a better polished sample, to within 1 μm, yielded a Si b_C value of 4.15195 ± 0.00011 fm after correcting for all possible sources of errors. Thus, Si b_C could be determined to within 27 parts per million.

By further reducing mechanical vibrations and thermal variations of the IFM set-up and using a sample polished to better flatness, the proposed ppm precision in b_C determination is achievable. Rauch et al.'s [126] nondispersive sample configuration afforded precise interferometric determination of neutron coherent scattering lengths and Ioffe et al. [127] improved the precision further by an order of magnitude by alternating the sample between the two paths of the interferometer. We have presented here a dual nondispersive sample which is more nondispersive than the single "nondispersive" sample by several orders of magnitude. This advantage will be especially interesting for cold neutron interferometry. The dual sample generates double the phase

with a null wave-packet displacement for thermal neutrons and substantially simplifies the angular alignment. One may envisage an interferometer setup dedicated to b_C measurements, operating at a large Bragg angle and with a mirror blade cut to accommodate a nongrooved dual phase shifter or a container cell for liquid and gaseous materials [128].

Further improvement in the b_C precision warrants the use of thicker samples which demands larger neutron IFMs and adequate neutron intensities at greater wavelengths. With the availability of large single crystal of excellent quality, it is indeed possible to fabricate bigger IFMs [159]. Therefore, with the next-generation neutron sources, it would be possible to determine neutron coherent scattering lengths of elements with much higher precision leading to a deeper understanding of inter-nucleon interaction.

REFERENCES

[1] H. Rauch and S. Werner, Neutron Interferometry: Lessons in Experimental Quantum Mechanics, Oxford: Oxford University Press (2000).

[2] V. F. Sears, Neutron Optics, Oxford: Oxford University Press (1989).

[3] J. Bryne, Neutrons, Nuclei and Matter, Bristol: Institute of Physics Publishing (1994); Rep. Prog. Phys., **45** (1982)115.

[4] A. G. Wagh and V. C. Rakhecha, Prog. Part. Nucl. Phys., **37** (1996) 485.

[5] A. G. Klein and S. A. Werner, Rep. Prog. Phys., **46** (1983) 259.

[6] L. de Broglie, Ann. de Phys., **3** (1925) 22.

[7] C. Davisson and L. H. Germer, Phys. Rev., **30**(6) (1927) 705.

[8] G. P. Thomson and A. Reid, Nature, **119** (1927) 890.

[9] W. L. Bragg, Proc. Cambridge Phil. Soc., **17** (1913) 43.

[10] J. Chadwick, Nature, **129** (1932) 312; Proc. Roy. Soc. London, A **136** (1932) 692.

[11] D. P. Mitchell and P. N. Powers, Phys. Rev., **50**(5) (1936) 486.

[12] S. Glasstone and A. Sesonske, Nuclear Reactor Engineering, Van Nostrand (1963).

[13] Development opportunities for small and medium scale accelerator driven neutron sources, Technical Meeting Report (Vienna), pp. 18, IAEA-TECDOC-1439 (May 2004).

[14] K. Clausen, PRAMANA- journal of Physics, **71** (2008) 623.

[15] C. G. Windsor, Pulsed Neutron Scattering, Taylor & Francis, London (1981).

[16] http:///www.helmholtz-berlin.de.; http:///www.frm2.tu-muenchen.de.

[17] “Rapport De Surete Du Reacteur A Haut Flux", Vol. 4, Institut Max von Laue – Paul Langevin, (Grenoble 1971); http:///www.ill.eu.

[18] National Facility for Neutron Beam Research, Eds. D. Sen, V. K. Aswal, R. Mukhopdhayay

and S. L. Chaplot, BARC Technical Brochure (BARC, Mumbai 2008).

[19] J. S. Nico et al., J. Res. Natl. Inst. Stand. Technol, **110** (2005) 137.

[20] P. N. Seo et al., Nucl. Instrum. Meth. A, **517** (2004) 285.

[21] http://www.sns.gov.

[22] http://www.j-parc.jp.

[23] J. M. Pendlebury, Ann. Rev. Nucl. Part. Sci., **43** (1993) 687; H. Abele, Prog. Part. Nucl. Phys., **60** (2008) 1.

[24] G. E. Bacon, Neutron Diffraction, Monographs on the Physics and Chemistry of Materials, Clarendon Press, Oxford (1955).

[25] G. E. Bacon, Neutron Diffraction, Clarendon Press, Oxford (1975) 3rd edn.

[26] S. W. Lovesey, Theory of Neutron Scattering from Condensed Matter, Volume 1: Nuclear Scattering, Clarendon Press, Oxford (1986).

[27] J. S. Higgins, H. C. Benoit, Polymers and Neutron Scattering, Oxford Science Publications, New York (1994).

[28] E. Fermi 1934 Collected papers Vol **1**, ed E Segre, Chicago: University of Chicago Press (1962) 757, Ricerca Sci. **7** (1936) 13.

[29] O. Halpern and M. H. Johnson, Phys. Rev., **55** (1939) 898.

[30] O. Halpern and T. Holstein, Phys. Rev., **59** (1941) 960.

[31] O. Halpern, M. Hamermesh and M. H. Johnson, Phys. Rev., **59** (1941) 981.

[32] M. Hamermesh, Phys. Rev., **61** (1942) 17.

[33] M. Lax, Rev. Mod. Phys., **23** (1951) 287.

[34] M. L. Goldberger and F. Seitz, Phys. Rev., **71**(5) (1947) 294.

[35] E. Fermi and L. Marshall, Phys. Rev., **71**(10) (1947) 666.

[36] J. S. Nico and W. M. Snow, Ann. Rev. Nucl. Part. Sci., **55** (2005) 27.

[37] B. W. Batterman, and H. Cole, Rev. Mod. Phys., **36** (1964) 681.

[38] G. Borrmann, G. Hilderbrandt and H. Wagner, Z. Phys., **142** (1955) 406.

[39] M. R. Eskildsen, P. L. Gammel, E. D. Isaacs, C. Detlefs, K. Mortensen and D. J. Bishop, Nature, **391**(1998) 563.

[40] T. Oku et al., Nucl. Instr. Meth. Phys. Res. A, **462** (2001) 435.

[41] T. Adachi et al., Proc. SPIE, **4509** (2001) 106.

[42] H. M. Shimizu, Appl. Phys. A**, 74** [Suppl.] (2002) S326–S328.

[43] T. Oku and H. M. Shimizu, Physica B, **276**–**278** (2000) 112; Physica B, **283** (2000) 314.

[44] H. Maier-Leibnitz and T. Springer, J. Nucl. Energy Parts A&B, Reactor Science and Technol., **17** (1963) 217; H. Maier-Leibnitz, Nukleonik, **8**(2) (1966) 61.

[45] R. Golub, D. Richardson, and S. K. Lamoreaux, Ultra-Cold Neutrons, Bristol: Adam Hilger (1991).

[46] V. V. Nesvizhevsky et al., Nature, **415** (2002)297; Eur. Phys. J., **C40** (2005) 479.

[47] T. Jenke, P. Geltenbort, H. Lemmel and H. Abele, Nature Physics, **7** (2011) 468.

[48] A. Akhelser and J. Pomeranehuk, Zhur. Eksptl'. i Teort. Fiz., **18** (1948) 475; H. Eksteln, Phys. Rev., **76** (1949) 1328; **78** (1950) 731; O. Halpern, Phys. Rev., **76** (1949) 1130; **88** (1952) 1003.

[49] F. Mezei, Comm. on Phys., **1** (1976) 81.

[50] H. Häse, A. Knöpfler, K. Fiederer, U. Schmidt, D. Dubbers and W. Kaiser, Nucl. Instr. Meth. Phys. Res. A**, 485** (2002) 453; M. Kreuz, V. Nesvizhevsky, A. Petoukhov and T. Soldner, Nucl. Instr. Meth. Phys. Res. A, **547** (2005) 583.

[51] M. Born and E. Wolf Principles of Optics, Oxford: Pergamon Press (1970) 4th edn.

[52] L. I. Schiff, Quantum Mechanics, McGraw-Hill, New York (1955) 2nd ed.

[53] H. Kawamoto and K. Okuwada, Development Trend for High Purity Silicon, Science & Technology Trends, (2007) pp38.

[54] C. G. Darwin, Phil. Mag., **27 (**1914) 315; Phil. Mag., **27 (**1914) 675.

[55] P. P. Ewald,. Ann. Physik (Leipzig), **54** (1917) 519.

[56] J. A. Prins, Z. Physik, **63** (1930) 477.

[57] M. von. Laue, Naturwiss,. **10** (1931) 133.

[58] W. H. Zachariasen, Theory of X-ray Diffraction in Crystals, John Wiley, New York (1945).

[59] R. W. James, The Optical Principles of the Diffraction of X-rays, G. Bell and Sons Ltd., London (1950).

[60] N. Kato, J. Phys. Soc. Japan, **7** (1952) 397; Acta Crystallogr., **13** (1960) 349.

[61] A. Authier, Ewald Waves in Theory and Experiment, Advances in structure research by diffraction methods, eds. R. Brill and R. Mason, Pergamon Press, Oxford (1970) pp. 1.

[62] N. Kato, X-ray Diffraction, in X-ray Diffraction, eds. L. V. Azaroff, , R. Kaplow, N. Kato, R. J. Weiss, A. J. C. Wilson, and R. A. Young, McGraw-Hill, New York (1974) pp. 176.

[63] Z. G. Pinsker, Dynamical Scattering of X-rays in Crystals, Springer Series in Solid State Sciences, Springer Verlag, Berlin (1978).

[64] A. Authier, Dynamical Theory of X-ray Diffraction, International Tables of Crystallography, ed. U. Shmueli, Academic Publishers, Dordrecht, **B** (1992) pp. 464.

[65] A. Authier, Dynamical Theory of X-ray Diffraction – I. Perfect Crystals; II. Deformed Crystals, X-ray and Neutron Dynamical Diffraction: Theory and Applications, eds. A. Authier, S. Lagomarsino and B. K. Tanner, Plenum Press, New York (1996).

[66] C. G. Shull, Phys. Rev. Lett., **21** (1968) 1585.

[67] V. F. Sears, Can. J. Phys., **56** (1982) 1261; Phys. Rev. D, **25 (**1982) 2023.

[68] V. F. Sears, Phys. Rep., **82** (1982) 2.

[69] H. Rauch and D. Petraschek, Neutron Diffraction, ed. H. Dachs, Springer Verlag, Berlin, (1978) pp.303; H. Rauch, Neutron Interferometery eds. U Bonse and H Rauch, Oxford: Oxford University Press (1979) pp.161.

[70] A. G. Wagh, Lecture Notes on Neutron Optics, in RCA-IAEA Summer course on use of reactor neutron beams in study of materials, BARC, Bombay (1986).

[71] C. Stassis and J. A. Oberteuffer, Phys. Rev. B, **10 (**1974) 303.

[72] J. W. Knowles Acta Crystallogr., **9 (**1956) 61.

[73] D. Sippel**,** K .Kleinstuck and G. E. R. Schulze, Phys. Stat. Solidi, **2 (**1962) K104.

[74] S. H. Shilshtein, V. A. Somenkov and V. P. Dokashenko, JETP. Lett., **13 (**1971) 214.

[75] S. Kikuta, I. Ishikawa, K. Kohra and S. Ttoshino, J. Phys. Soc. Jpn., **39** (1975) 471.

[76] A. Zeilinger and C. G. Shull, Phys. Rev. B, **19** (1979) 3957.

[77] C. G. Shull, A. Zeilinger, G. L. Squires, M. A. Horne, D. K. Atwood and J. Arthur, Phys. Rev. Lett., **44 (**1980b) 1715.

[78] C. G. Shull and J. A. Oberteuffer, Phys. Rev. Lett., **29** (1972) 871.

[79] C. G. Shull, J. Appl. Crystallogr., **6** (1973) 257.

[80] H. Rauch, W. Treimer and U.Bonse, Phys. Lett. A, **47** (1974) 369.

[81] U. Bonse and M. Hart, Appl. Phys. Lett., **6 (**1965) 155.

[82] H. Maier-Leibnitz and T. Springer, Z. Phys., **167**(1962) 386.

[83] U. Bonse and W. Graeff, in X-Ray Optics, ed. H.J. Queisser, Springer Verlag, Berlin (1977) pp. 93.

[84] A. Zeilinger, C. G. Shull, J. Arthur and M. A. Horne, Phys. Rev. A, **28** (1983) 487.

[85] H. Rauch, A. Zeilinger, G. Badurek, A. Wilfing, W. Bauspiess and U. Bonse, Phys. Lett.

A, **54** (1975) 425; Z. Phys. B, **29** (1978) 281.

[86] S. A. Werner, R. Colella, A. W. Overhauser and C. F. Eagen, Phys. Rev. Lett., **35** (1975) 1053; A. G. Klein and G. I. Opat, Phys. Rev. Lett., **37** (1976) 238.

[87] G. Badurek, H. Rauch, A. Zeilinger, W. Bauspiess and U. Bonse, Phys. Rev. D, **14** (1976) 1177.

[88] A. W. Overhauser and R. Colella, Phys. Rev. Lett., **33** (1974) 1237; R. Colella, A. W. Overhauser and S. A. Werner, Phys. Rev. Lett., **34** (1975) 1472; J. L. Staudenmann, S. A. Werner, R. Colella and A. W. Overhauser, Phys. Rev A, **21** (1980) 1419.

[89] A. G. Wagh, V. C. Rakhecha, J. Summhammer, G. Badurek, H. Weinfurter, B. E. Allman, H. Kaiser, K. Hamacher, D. L. Jacobson and S. A. Werner, Phys. Rev. Lett., **78** (1997) 755; J. Phys. Soc. Jpn., **65** (Suppl. A) (1996) 73; Phys. Rev. A, **56** (1997) 4420.

[90] A. Cimmino, G. I. Opat, A. G. Klein, H. Kaiser, S. A. Werner, M. Arif and R. Clothier, Phys. Rev. Lett., **63** (1989) 380.

[91] H. Kaiser, S. A. Werner, R. Clothier, M. Arif, A. G. Klein and A. Cimmino, in Proc. Int. Conf. Atomic Physics 12, AIP Conf. Proc. no. 233, Eds. J. C. Zorn and R. R. Lewis, (NY, AIP 1991) pp. 247.

[92]] B. E. Allman, A. Cimmino, A. G. Klein, G. I. Opat, H. Kaiser and S. A.Werner, Phys. Rev. Lett., **68** (1992) 2409; Erratum, **70** (1993) 250; Phys. Rev. A, **48** (1993) 1799.

[93] G. Badurek, H. Weinfurter, R. Gahler, A. Kollmar, S. Wehinger and A. Zeilinger, Phys. Rev. Lett., **71** (1993) 307.

[94] H. Rauch, H. Lemmel, M. Baron and R. Loidl, Nature, **417** (2002) 630.

[95] H. Rauch, H. Wolwitsch, H. Kaiser, R. Clothier, and S. A.Werner, Phys. Rev. A, **53** (1996) 902.

[96] D. A. Pushin, M. Arif, M. G. Huber, and D. G. Cory, Phys. Rev. Lett., **100** (2008) 250404.

[97] A. Cabello, S. Filipp, H. Rauch and Y. Hasegawa, Phys. Rev. Lett., **100** (2008) 130404.

[98] Matter Wave Interferometry, eds. G. Badurek, H. Rauch and A. Zeilinger, Physica B, **151** (1988) 1531.

[99] M. Suda, Quantum Interferometry in Phase Space: Theory and Applications, Springer, New York (2006)

[100] D. M. Greenberger and A. W. Overhauser, Rev. Mod. Phys., **51** (1979) 43; D. M. Greenberger, Rev. Mod. Phys., **55** (1983) 875.

[101] S. A. Werner, Phys. Today 33, **12** (1980) 24; S. A. Werner, Class. Quantum Grav., **11** (1994) A207; Ann. N.Y. Acad. SC., **755** (1995) 241.

[102] H. Rauch, in Proc. Int. Symp. Foundations of Quantum Mechanics, Tokyo, 1983 (Phys. Sot. Japan, Tokyo), pp. 277; Contm. Phys., **27** (1986) 345; Found. Phys., **23** (1993) 7.

[103] S. A. Werner and A. G. Klein, in Methods of Experimental Physics, Vol. 23, Part A, eds. K. Skold and D. L. Price, Academic Press, New York (1986) pp. 259.

[104] A. G. Wagh and V. C. Rakhecha, Physics News (India), **22** (Mar-Jun 1991) 27; *ibid.* **25** (Dee 1994) 163; V. C. Rakhecha, and A. G. Wagh, Ind. J. Pure Appl. Phys., **27** (1989) 582.

[105] S. Abbas and A. G. Wagh, Pramana- J. Phys., **71** (2008) 1115; A. G. Wagh and S. Abbas, Sol. St. Phys. (India), **50** (2005) 99.

[106] D. Dubbers, Prog. Part. Nucl. Phys., **26** (1991) 173.

[107] S. K. Lamoreaux, Int. J. Mod. Phys. A, **7** (1992) 6691.

[108] C. S. Schneider and C.G. Shull, Phys. Rev. B**, 3** (1971) 830.

[109] A. G. Wagh and V. C. Rakhecha, Pramana – J. Phys., **63** (2004) 381.

[110] A. Authier, J. Phys. Radium, **23** (1962) 961.

[111] A. G. Wagh, V. C. Rakhecha and W. Treimer, Phys. Rev. Lett., **87** (2001) 125504.

[112] W. Treimer, M. Strobl and A. Hilger, Appl. Phys. A, **74** (Suppl.) (2002) S191.

[113] Proceedings of XIth International Conference on Small-Angle Scattering (SAS99), Brookhaven, 1999, eds. D. K. Schneider and S.-H. Chen [J. Appl. Cryst., **33** (2000) 421].

[114] T. Brückel, Neutron Scattering - JCNS lab course, eds. T. Brückel, G. Heger, D. Richter and R. Zorn (2008) 6.1.

[115] U. Bonse and M. Hart, Appl. Phys. Lett., **7** (1965) 238.

[116] T. Koga, M. Hart, and T. Hashimoto, J. Appl. Cryst., **29** (1996) 318; D. Schwahn, A. Miksovsky, H. Rauch, E. Seidl, and G. Zugarek, Nucl. Instr. Meth. Phys. Res. A, **239** (1985) 229.

[117] M. Agamalian, D. K. Christen, A. R. Drews, C. J. Glinka, H. Matsuoka, and G. D. Wignall, J. Appl. Cryst., **31** (1998) 235.

[118] G. Kroupa, G. Bruckner, O. Bolik, M. Zawisky, M. Hainbuchner, G. Badurek, R. J. Buchelt, A. Schricker and H. Rauch, Nucl. Instr. Meth. Phys. Res. A, **440** (2000) 604.

[119] L. Koester, H. Rauch and E. Seymann, Atom. Data Nucl. Data Tables, **49** (1991) 65; ILL Neutron Data Booklet, Eds. A.-J. Dianoux and G. Lander (2002)

[120] L. Koester, K. Knopf and W. Waschkowski, Z. Phys. A, **282** (1977) 371.

[121] D. J. Hughes, Neutron Optics, Inter Science, New York (1954).

[122] E. Fermi and L. Marshall, Phys. Rev., **71** (1947) 666; W. C. Dickinson, L. Passell and O. Halpern, Phys. Rev., **126** (1962) 632; R. E. Donaldson, L. Passell, W. Bartolini and D. Groves, Phys. Rev., **138** (1965) B1116; T. A. Kitchens, T. Oversluizen and L. Passell, Phys. Rev. Lett., **32** (1974) 791.

[123] H. Maier-Leibnitz, Z. Angew. Phys., **14** (1962) 738; L. Koester, Z. Phys., **182** (1965) 328.

[124] C. S. Schneider, Rev. Sci. Instrum., **44** (1973) 1594; Acta Cryst. A, **32** (1976) 375.

[125] W. Waschkowski and L. Koester, Z. Naturforsch. Teil A, **31** (1976) 115.

[126] H. Rauch, E. Seidl, D. Tuppinger, D. Petrascheck and R. Scherm, Z. Phys. B, **69** (1987) 313.

[127] A. Ioffe, D. L. Jacobson, M. Arif, M. Vrana, S. A. Werner, P. Fischer, G. L. Greene, and F. Mezei, Phys. Rev. A, **58** (1998) 1475.

[128] H. Lemmel and A. G. Wagh, Phys. Rev. A, **82** (2010) 033626 (pp. 1).

[129] S. Abbas, A. G. Wagh, and W. Treimer, Sol. St. Phys. (India), **54** (2009) 212.

[130] M. G. Huber et al., Phys. Rev. Lett., **102** (2009) 200401; O. Zimmer, G. Ehlers, B. Farago, H. Humblot, W. Ketter and R. Scherm, EPJ direct A, **1** (2002) 1.

[131] M. Peshkin and G. R. Ringo, Am. J. Phys., **39 (**1971) 324.

[132] N. Kato, Acta Cryst., **11** (1958) 885.

[133] W. Soller, Phys. Rev., **24** (1924) 158.

[134] P. D. Hey, B. Mack and C. Carlile, Rutherford Laboratory Report, **RL-75-20** (1975).

[135] H. Meister, and B. Weckermann, Nucl. Instr. Meth. Phys. Res., **108** (1973) 107.

[136] A. Zeilinger and C. G. Shull, Phys. Rev. B, **19** (1979) 3957.

[137] G. F. Knoll, Radiation Detection and Measurement, John Wiley & Sons, Inc., New York (1979); D. H. Wilkinson, Ionization Chambers and Counters, Cambridge University Press, Cambridge, Massachusetts (1950).

[138] A. G. Wagh, Phys. Lett. A**, 121** (1987) 45; Phys. Lett. A, **123** (1987) 499.

[139] S. Abbas and A. G. Wagh, Sol. St. Phys. (India), **50** (2005) 317.

[140] S. Abbas, A. G. Wagh, M. Strobl and W. Treimer, Nucl. Instr. Meth. Phys. Res. A, **634** (2011) S144.

[141] S. Abbas, A. G. Wagh, and W. Treimer, Pramana- J. Phys., **71** (2008) 1109.

[142] S. Abbas, A. G. Wagh, M. Strobl and W. Treimer, Journal of Physics (CS), **251** (2010) 012073.

[143] S. Abbas, A. G. Wagh, M. Strobl and W. Treimer, Sol. St. Phys. (India), **51** (2006) 351.

[144] M. Strobl, W. Treimer, Ch. Ritzoulis, A. G. Wagh, S. Abbas and I. Manke, J. Apl. Cryst.,

40 (supplement) (2007) s463.

[145] A. G. Wagh, S. Abbas , M. Strobl and W. Treimer, BENSC Experimental Reports 2005 (HMI, Germany, 2006) 115.

[146] A. G. Wagh, S. Abbas and W. Treimer, Journal of Physics (CS), **251** (2010) 012074.

[147] A. G. Wagh, S. Abbas and W. Treimer, Nucl. Instr. Meth. Phys. Res. A, **634** (2011) S41.

[148] A. G. Wagh, S. Abbas, and W. Treimer, Pramana- J. Phys. **71** (2008) 1171.

[149] A. G. Wagh and S. Abbas, Sol. St. Phys. (India), **51** (2006) 353.

[150] A. G. Wagh, S. Abbas, M. Strobl and W. Treimer, BENSC Experimental Reports 2006 (HMI, Germany, 2007) 22.

[151] S. Abbas, A. G. Wagh, M. Strobl and W. Treimer, Sol. St. Phys. (India), **52** (2007) 441.

[152] A. G. Wagh, S. Abbas and W. Treimer, BENSC Experimental Reports 2007 (HMI, Germany, 2008) 223.

[153] A. G. Wagh, S. Abbas and W. Treimer, Sol. St. Phys. (India) **53** (2008) 553.

[154] S. Abbas, A. G. Wagh and W. Treimer, Sol. St. Phys. (India), **53** (2008) 555.

[155] S. Abbas, A. G. Wagh and W. Treimer, Abstract book, CNSMS (2009) 112

[156] S. Abbas and A. G. Wagh, Pramana J-Phys., **63** (2004) 375.

[157] H. A. Graf and J. R. Schneider, Acta Cryst. A, **37** (1981) 863.

[158] A. G. Wagh and S. Abbas, J. Res. Natl. Stad. Technol. **110** (2005) 237.

[159] M. Zawisky, M. Baron, R. Loidl and H. Rauch, Nucl. Instr. Meth. Phys. Res. A, **481** (2002) 406

[160] S. Abbas, A. G. Wagh, R. Loidl, H. Lemmel and H. Rauch, AIP Conf. Proc., **1349** (2011) 501.

[161] A. G. Wagh, S. Abbas R. Loidl, H. Lemmel and H. Rauch, ILL Experimental Reports

2009, (Grenoble, France, 2010) **3-15-58**.

[162] A. G. Wagh, S. Abbas T. Potocar, H. Lemmel and H. Rauch, ILL Experimental Reports 2011, (Grenoble, France, submitted) **3-15-61**.

[163] S. Abbas, A. G. Wagh, T. Potocar, H. Lemmel and H. Rauch, AIP Conf. Proc., (2011) in press.

[164] M. Zawisky, J. Springer, and H. Lemmel, Nucl. Instr. Meth. Phys. Res. A, **634** (1-2) (2011) S46–S49.

[165] J. Springer, M. Zawisky, H. Lemmel and M. Suda, Acta. Cryst., **A66 (**2010)17.

[166] A. G. Wagh, V. C. Rakhecha, M. Strobl and W. Treimer, Pramana - J. Phys, **63** (2004) 369.

[167] G. Badurek, R.J. Buchelt, G. Kroupa, M. Baron and M. Villa, Physica B, **283** (2000) 389.

[168] E. Jericha, G. Badurek, M. Trinker, Physica B, **397** (2007) 88.